

ABSTRACT

CAPRACOTTA, MICHAEL DAVID. Mechanisms of Reactivity and Lattice Reconstructions in Ternary Copper (I) Halides. (Under the direction of James D. Martin).

The work in this dissertation consists of a two-part study in which families of ternary copper (I) halides are used to explore mechanisms of phase transitions and reactions in solids. Lewis acid modified copper (I) chloride networks of the formula CuMCl_4 ($M = \text{Al}, \text{Ga}$) bind up to 2 molar equivalents of either ethylene or CO at low gas pressures. These reactions proceed at room temperature to give crystalline adduct phases through a dramatic expansion and restructuring of the CuMCl_4 lattice. The CO adducts of CuMCl_4 are characterized by *in situ* powder X-ray diffraction, UV-vis diffuse reflectance spectroscopy, and FTIR spectroscopy. The structure of the $\beta\text{-(CO)CuAlCl}_4$ adduct is determined by single crystal X-ray diffraction. A sorptive reconstruction mechanism is proposed for the formation of $\beta\text{-(CO)CuAlCl}_4$ in which $\text{S}_\text{n}2$ attack on copper is directed along van der Waals channels in the $\alpha\text{-CuAlCl}_4$ lattice. To demonstrate the effect of Lewis acids on the bonding between Cu(I) and π -coordinating ligands, the reactivity of the series of solids CuCl , CuGaCl_4 and CuAlCl_4 with both ethylene and CO gas is considered. The bonding of copper (I) to CO in the Lewis acid-modified frameworks is shown to be non-classical, consisting predominantly of σ -bonding. The enhancement to the σ -bonding component of the Cu-L bond provided by the Lewis acid results in competitive bonding of CO and ethylene. The reactions of CuAlCl_4 are studied at 35°C by TGA/DSC and optical microscopy provide kinetic data for use in evaluating the proposed sorptive reconstruction mechanism of gas sorption and lattice rearrangement. The reactions to give $(\text{C}_2\text{H}_4)\text{CuAlCl}_4$ and $(\text{C}_2\text{H}_4)_2\text{CuAlCl}_4$ are shown to

follow 1-D phase boundary controlled growth kinetics. A dual reaction mechanism is proposed for the low pressure formation of $(C_2H_4)CuAlCl_4$, which is shown to be a liquid at 35°C. A linear rate dependence on the ethylene partial pressure for the crystallization of $(C_2H_4)_2CuAlCl_4$ is consistent with an associative reaction mechanism. In the second study the phase transition of melting in copper halides is probed by the examination of the molten structure of ternary compounds of composition ACu_2Cl_3 (A = monovalent templating cation) are studied by synchrotron X-ray and neutron diffraction. The structure of these compounds consist of covalently bonded $[Cu_2Cl_3]^-$ chains which run parallel to one another. Neutron diffraction and PDF analysis shows that these chains persist into the molten state and can serve as a structural unit for designing order into the molten state. This order can be further manipulated by choice of the templating cation. This work is relevant to understanding and designing structure in the molten state.

MECHANISMS OF REACTIVITY AND LATTICE RECONSTRUCTIONS
IN TERNARY COPPER (I) HALIDES

by

MICHAEL DAVID CAPRACOTTA

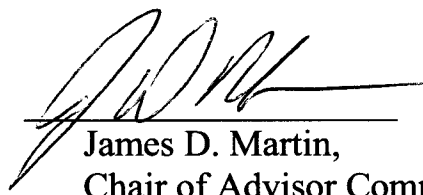
A dissertation submitted to the Graduate Faculty of
North Carolina State University
in partial fulfillment of the
requirements for the Degree of
Doctor of Philosophy

CHEMISTRY

Raleigh

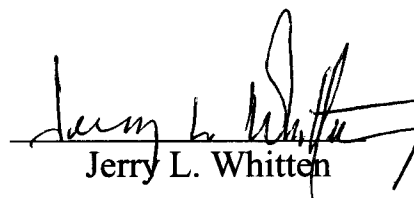
2006

Approved by:


James D. Martin,
Chair of Advisor Committee


T. Brent Gunnoe


Paul A. Maggard


Jerry L. Whitten

DEDICATION

This work is dedicated to the memory of Joan Watson.

BIOGRAPHY

Michael David Capracotta was born on September 24, 1979 in Charleston, South Carolina to parents David and Deborah. His father was an officer in the United States Air Force, and his family lived in several locations from 1979 to 1991 including Rome New York, Sumter South Carolina and Albuquerque New Mexico. During this time Michael's brother Stephen and sister Christina were born. In 1991 the family settled back in Charleston after Michael's father left active duty from the Air Force. Michael attended Fort Dorchester High School in North Charleston, where during his junior and senior years he fostered an interest in chemistry under the instruction of his high school teachers Cathy McClam and Susan Spell. He graduated from Fort Dorchester in 1997 and enrolled at Clemson University majoring in chemistry. After graduating from Clemson in 2001, (Clemson's first graduating class of the 21st century) he moved to Raleigh, North Carolina to begin graduate school at North Carolina State University in part due to the advice and instruction of his undergraduate research advisor at Clemson Professor Shiou-Jyh Hwu. While at N. C. State, Michael met fellow graduate student Sonja Siefert, who he became engaged to in December 2005.

ACKNOWLEDGEMENTS

A number of people have made important direct or indirect contributions without which this work would not have been possible. First and foremost I would like to thank my advisor Dr. James D. Martin for the opportunity to help further his scientific vision. I would also like to thank him for his sage advice on matters both professional and personal, as well as for his friendship during my time at N. C. State. My predecessors in the Martin Group, Dr. Roger M. Sullivan and Steve Smith provided the ground work for much of my research. Also, the scientific support and friendship of my contemporaries in the Martin group (including Dr. Jaap Folmer, Stephen J. Goettler, Amanda A. Josey, Cristin L. Keary, Jeremy W. Knutson, Stan T. Toporek and Robert J. Wilcox) have been invaluable. My path would not have led to N.C. State if not for the inspiration and guidance of the many excellent teachers I've been blessed with over the years, notably Dr. Shiou-Jyh Hwu, Cathy McClam, Susan Spell and E. Penryn Flemyng. Finally, I'd like to thank my family for their constant love and encouragement throughout my academic career, and my fiancée who has provided much needed support over the last two years.

TABLE OF CONTENTS

List of Tables	vii
List of Figures.....	viii
Chapter 1: Introduction	1
1.1 Introduction	2
1.2 Metal Halide Networks	3
1.3 Utility of Cu(I) in Gas Separations	4
1.4 Small Molecule Interactions With Solids	7
1.5 Scope	11
1.6 References	13
Chapter 2: Sorptive Reconstruction of CuMCl_4 (M = Al and Ga) Upon Small Molecule Binding and The Competitive Binding of CO and Ethylene.....	17
2.1 Introduction	19
2.2 Background	20
2.3 Results	25
2.4 Discussion	49
2.5 Conclusions	58
2.6 Experimental	59
2.7 References	65
Chapter 3: The Molten Structure of the Templated Copper Chloride Melts ACu_2Cl_3 (A = monovalent templating cation).....	69
3.1 Introduction	71
3.2 Results & Discussion	73
3.3 Conclusions	112

3.4 Experimental	113
3.5 References	118
Chapter 4: Kinetics of the Lattice Reconstructions in CuAlCl₄ Induced By Small Molecule Binding	121
4.1 Introduction	124
4.2 Background	125
4.3 Results	131
4.4 Discussion	146
4.5 Conclusions	161
4.6 Experimental	162
4.7 References	165

LIST OF TABLES

Table 2.1.	Summary of Cu(I)-monocarbonyl stretching frequencies.....	24
Table 2.2.	Characteristic Low Angle Reflections for identifying Phases in Powder X-ray Diffractograms.....	31
Table 2.3.	Summary of Crystal Data for $(\text{CO})_x\text{CuMCl}_4$ Adducts.....	40
Table 3.1.	Summary of Crystal Data for $(\text{H}_2\text{NMe}_2)\text{Cu}_2\text{Cl}_3$, 1	75
Table 3.2.	Selected Bond Distances and Angles for $(\text{H}_2\text{NMe}_2)\text{Cu}_2\text{Cl}_3$, 1	75
Table 3.3.	Crystal Symmetry and Melting Points of AM_xX_y Chain Structures.....	77
Table 3.4.	Room Temperature Lattice Constants For $(\text{H}_2\text{NMe}_2)\text{Cu}_2\text{Cl}_{3-y}\text{Br}_y$	84
Table 3.5.	Sum of Cation Radius (r_+) and Halide Radius (r_-) Over Diagonal of Prism Face (d) in AM_2X_3	107
Table 3.6.	Calculated M-M Distances in AM_2X_3 Structures	110

LIST OF FIGURES

- Figure 1.1** A comparison of the Dewar-Chatt-Duncanson model for Cu (I) bonding to olefins and to CO. The lower energy of the CO π^* gives the results in the stronger π -backbonding interaction, while the σ -interaction is stronger with the olefin due to greater spacial overlap..... 6
- Figure 2.1.** Representative sorption-desorption isotherms for the systems CuAlCl₄ + CO and CuGaCl₄ + CO..... 26
- Figure 2.2.** Sorption-desorption isotherms for the one equivalent phases from the CuAlCl₄ + CO and CuGaCl₄ + CO systems..... 27
- Figure 2.3.** Variable pressure x-ray diffraction showing the conversion of α -CuAlCl₄ to (CO)₂CuAlCl₄ at (a) 0; (b) 860; (c) 1000; (d) 1500 (e) 2000; (f) 2500; (g) 3000; (h) 3500; (i) 4000; (j&k) 4500 Torr of CO. The powder patterns are color coded blue for α -CuAlCl₄, red for α -(CO)CuAlCl₄ and for (CO)₂CuAlCl₄..... 32
- Figure 2.4.** Synchrotron x-ray diffractograms of CuAlCl₄ prior (blue) to and after (green) exposure to CO gas giving incomplete reaction to give the β -(CO)CuAlCl₄ adduct (calculated pattern shown in red). Diffraction peaks are identified by blue dots- α -CuAlCl₄, red dots- β -(CO)CuAlCl₄, and green dots- (CO)₂CuAlCl₄..... 33
- Figure 2.5.** Variable Pressure X-ray diffraction of showing the conversion of CuGaCl₄ to β -(CO)CuGaCl₄ (red lines) and (CO)₂CuGaCl₄ (green line) at a) 0 Torr; b&c) 20 psi; d) 30 psi; e) 40 psi; f) 50 psi of CO..... 34
- Figure 2.6.** Time/temperature-resolved x-ray diffraction for the desorption of CO from (CO)₂CuAlCl₄: [diffractogram, temperature in °C]: (a) (CO)₂CuAlCl₄, (green line) 25; desorption to form (CO)CuAlCl₄, (b) 26; (c) 27; (d) 29; (e) 30; (f) 31; pure (CO)CuAlCl₄ (red lines) (g) 32; (h) 36; (i) 43; (j) 45; (k) 50; (l) melted (CO)CuAlCl₄ (purple line) 53; desorption to give CuAlCl₄ (blue lines) (m) 57; (n) 61. 36
- Figure 2.7.** Quarter image plates from PRXRD of reaction of CuMCl₄ + CO. (a) Grainy diffraction pattern of **2-CO_{Al}** with amorphous diffraction ring from the eutectic melt. (b) Grainy diffraction pattern with a mixture of **2-CO_{Ga}**, **β -1-CO_{Ga}** and α -CuGaCl₄. (c) microcrystalline α -CuGaCl₄ from desorption of CO from (b), and (d) Nanocrystalline diffraction pattern of (CO)CuCl..... 37
- Figure 2.8.** (a) ORTEP (50% probability ellipsoid) of a chain of **β -1-CO** showing the atom labeling scheme. (b) A crystal packing view of the crystal structure

- looking down the chains (along **b**). (c) A view of the pseudo-close packing of the chlorides and carbonyl ligands in the (201) planes..... 41
- Figure 2.9.** FTIR of CO + CuAlCl₄ reaction at (a) 0 Torr; (b) 200 Torr; (c) 375 Torr; (d) 750 Torr; (e) 850 Torr; (f) 950 Torr. Spectrum g is of the eutectic liquid which forms in this system..... 45
- Figure 2.10.** Diffuse reflectance UV-Vis of CO + CuAlCl₄ reaction at (a) vacuum; (b) 110 Torr; (c) 820 Torr; and (d) 930 Torr..... 46
- Figure 2.11.** Diffuse reflectance UV-vis CO + CuGaCl₄ reaction at a) 0 Torr; b) 200 Torr; and c) 620 Torr of CO..... 47
- Figure 2.12.** Pathway for the sorptive reconstruction of α -CuAlCl₄ to chains of (CO)CuAlCl₄. (a) View of α -CuAlCl₄ looking down the 112 vector with shaded blue regions highlighting the van der Waals channels. (b) A chain excised from α -CuAlCl₄ (outlined in a box in a.) running parallel to the 112 vector. (c) A single chain of β -(CO)CuAlCl₄..... 51
- Figure 3.1.** (a) Crystal structure of **1** viewed down the direction of chain propagation. (b) ORTEP (50% probability ellipsoid) of **1**, emphasizing the hydrogen-bonding between the templating cations and a single [Cu₂Cl₃]⁻ chain..... 76
- Figure 3.2** Representative examples of known AM₂X₃ chain structures. The packing arrangements of the [M₂X₃]⁻ chains varies depending on the size and shape of the templating cation, where small cations (Rb⁺, Cs⁺) form close packed layers with the halide while larger cations disrupt the close packing to give a variety of structures..... 79
- Figure 3.3** (a) Slice taken through the 221 lattice planes of CsCu₂Cl₃ showing a single pseudo-closed packed layer of [Cs]⁺ templating cations and [Cl]⁻ anions. (b) A view of CsCu₂Cl₃ highlighting the coordination geometry around [Cs]⁺ with bonds drawn in red to the chlorides forming the rectangular anti-prism. Each chloride is labeled to indicate which chain it is associated with (numbered 1-3) as well as its coordination to copper. The [Cs]⁺ and [Cl]⁻ ions combine to show three pseudo close-packed layers..... 80
- Figure 3.4** Slice taken through the 221 lattice planes of [H₂NMe₂]Cu₂Cl₃, **1**, showing a single pseudo-closed packed layer of [H₂NMe₂]⁺ templating cations and [Cl]⁻ anions, analogous the the close packed layer of CsCu₂Cl₃..... 81
- Figure 3.5** Room temperature X-ray diffraction of the mixed halide solid solutions (H₂NMe₂)Cu₂Cl_{3-y}Br_y for selected compositions..... 83

Figure 3.6	Unit cell volumes and lattice parameters of the mixed halide solid solution $(\text{H}_2\text{NMe}_2)\text{Cu}_2\text{Cl}_{3-y}\text{Br}_y$ as a function of bromide content y	85
Figure 3.7	Measured melting points of selected compositions of mixed halide solid solution $(\text{H}_2\text{NMe}_2)\text{Cu}_2\text{Cl}_{3-y}\text{Br}_y$ as a function of bromide content y	89
Figure 3.8	Structure factor $S(Q)$ and pair distribution $G(r)$ plots comparing the molten structures CsCu_2Cl_3 , CuCl and CsCl . Data for CuCl and CsCl were scanned from the referenced reports.....	92
Figure 3.9	X-ray (red) and neutron (blue) diffraction patterns of crystalline and molten CsCu_2Cl_3 . The molten diffraction patterns (a and c) were collected at 300°C while the crystalline diffraction patterns were calculated for the two different radiation sources using the room temperature lattice constants for CsCu_2Cl_3 (b and d). The amorphous scattering is closely correlated with the labeled crystalline diffraction peaks.....	94
Figure 3.10	Spacings between the crystalline lattice planes correlated to the amorphous diffraction of molten CsCu_2Cl_3 . The 221 and 111 plane spacings correspond to the distance between $[\text{Cs}]^+ / [\text{Cl}]^-$ close packed planes and planes of $[\text{Cs}]^+$ cations respectively. The 110 and 020 plane spacings are related to the distance between $[\text{Cu}_2\text{Cl}_3]^-$ chains.....	95
Figure 3.11	X-ray (red) and neutron (blue) diffraction patterns of crystalline and molten 1 . The molten diffraction patterns (a and c) were collected at 150°C while the crystalline diffraction patterns were calculated for the two different radiation sources using the room temperature lattice constants for 1 . The neutron data was collected using a fully deuterated sample, while the x-ray data was collected with a sample of natural isotopic abundance. The amorphous scattering is closely correlated with the labeled crystalline diffraction planes.	97
Figure 3.12	The spacings between the crystalline lattice planes correlated to the amorphous diffraction of molten. The spacings between the 111 and 221 of 1 correspond to the separation between close packed layers of $[\text{H}_2\text{NMe}_2]^+ / [\text{Cl}]^-$ and layers of $[\text{H}_2\text{NMe}_2]^+$ cations respectively. The distance between the 110 and 200 planes correspond to the spacing between $[\text{Cu}_2\text{Cl}_3]^-$ chains.....	98
Figure 3.13	Crystalline and melt diffraction patterns of $(\text{NMe}_4)\text{Cu}_2\text{Cl}_3$ collected with X-ray diffraction.....	100
Figure 3.14	The spacings between the crystalline lattice planes correlated to the amorphous diffraction of molten $[\text{NMe}_4]\text{Cu}_2\text{Cl}_3$. The 200 and 101 planes relate to spacings between the $[\text{Cu}_2\text{Cl}_3]^-$ chains.....	101

- Figure 3.15** Overlay of the pair distribution function $G(r)$ plot of molten CsCu_2Cl_3 and the calculated atom-atom contact distances for the room temperature crystal.. 103
- Figure 3.16** The face of the rectangular antiprism, shaded, is defined by the μ_2 -chlorides of two neighboring chains. The diagonal distance across this plane, d , is determined by the distances between the chains and the μ_2 -chlorides of a given chain..... 111
- Figure 4.1** Representative TGA/DSC data for the stepwise reaction of CuAlCl_4 with ethylene. After exposure to an initial ethylene partial pressure of <30 Torr the sample rapidly binds ~0.4-0.5 equivalents of gas followed by additional slower absorption to reach the one equivalent phase **et-1**. Subsequent exposure to an ethylene pressure of 700 Torr, causes the sample to quickly bind an additional 0.8 equivalents of gas to yield **et-2**..... 134
- Figure 4.2** Representative TGA/DSC data for CuAlCl_4 exposed to an initial ethylene partial pressure greater than 50 Torr. (a) Reaction of agate mortar and pestle ground CuAlCl_4 on exposure to 380 Torr of ethylene. (b) Reaction of CuAlCl_4 particles sieved to a diameter of 0.2-0.3mm to an ethylene partial pressure of 80 Torr..... 137
- Figure 4.3** The early stages for the high pressure ethylene reaction with CuAlCl_4 at ethylene partial pressures of a) 760 Torr, b) 570 Torr, c) 380 Torr, d) 280 Torr, and e) 90 Torr. At every pressure studied an inflection in the TGA curve occurs at a weight gain corresponding to 0.4 equivalents of ethylene sorbed..... 137
- Figure 4.4** The particle size dependence of the reaction of CuAlCl_4 at ethylene partial pressures below 30 Torr. The reaction rate decreases somewhat with increasing particle size..... 139
- Figure 4.5** TGA/DSC data of the α - CuAlCl_4 reaction with CO. The DSC indicates the irreversibility of the reaction under these experimental conditions..... 141
- Figure 4.6** Optical microscopy showing finely ground α - CuAlCl_4 a) prior to reaction with ethylene, b) 1 minute after exposure in which the smallest particles have reacted, c) 5 minutes after initial exposure showing significant formation of the liquid **et-1**, d) 10 minutes after exposure with the majority of the sample liquid with a the reaction still penetrating the largest particle, e) 15 minutes after exposure in with further penetration into the largest particle, and f) nearly complete formation of the liquid **et-1** adduct..... 143
- Figure 4.7** Particles of α - CuAlCl_4 sieved to 0.2-0.3mm diameter a) prior to reaction with ethylene, b) after exposure for 1 hour, c) during the initial stages of ethylene desorption from **et-2** yielding some liquid **et-1**, and d) after desorption is complete leaving highly fractured α - CuAlCl_4 145

- Figure 4.8** Sharp-Hancock plot for the low pressure reaction of finely ground CuAlCl_4 particles, which exhibits a change of slope near $\alpha = 0.40$ indicating a change in the reaction mechanism..... 148
- Figure 4.9** The Sharp-Hancock plot for the low pressure reaction of CuAlCl_4 particles sieved to a diameters from 0.2-0.3 mm, which has a single linear region over the approximate range $0.05 < \alpha < 0.75$ 150
- Figure 4.10** Sharp-Hancock plots for the **et-1** \rightarrow **et-2** reaction at a) 700 Torr, b) 620 Torr, c) 320 Torr and d) 70 Torr, with slopes between $0.15 < \alpha < 0.5$ of 3.56, 3.31, 2.70 and 1.05, respectively..... 153
- Figure 4.11** The ethylene partial pressure dependence of the probability of nucleation, β , for the 1-D phase boundary controlled crystallization of **et-2** from the **et-1** melt occuring on sorption of a second equivalent of gas..... 154
- Figure 4.12** The pressure dependence at 35°C of the rate constant k_{obs} extracted from the Sharp-Hancock analysis of the TGA data for the **et-1** to **et-2** ethylene sorption reaction..... 155
- Figure 4.13** a) View of $\alpha\text{-CuAlCl}_4$ down the 112 lattice vector with the entrance to the van der Waals channels shaded. b) Chains running along the 112 vector which are excised from the CuAlCl_4 lattice by the sorptive reconstruction mechanism to give the ladder chain structures c) $\beta\text{-COCuAlCl}_4$ or d) $\beta\text{-etCuAlCl}_4$. f) Alternatively reaction may be directed along the perpendicular sets of tetragonal channels running along the 100 and 010 lattice vector to give the perpendicular sets of $\alpha\text{-etCuAlCl}_4$ chains..... 158

Chapter 1:
Introduction

1.1 Introduction

Research in materials chemistry is critical to continuing advances in fields such as communications, catalysis and energy management.¹ Traditionally, solid-state chemistry's contribution to materials research has focused on the discovery of new crystal structures and the study of their structure-property relationships.² Today powerful computing resources, made possible by advances in materials science, greatly simplify the process of crystal structure solution and allow solid-state scientists to focus on increasingly complex problems, such as the rational design of new materials with specifically targeted properties.³ Understanding both synthesis structure-property relationships requires the recognition that the dynamic processes involved in solid-state phase transitions and reactivity are often the key to understanding a material's properties. For instance, reversible binding of small molecules by the recently discovered class of metal-organic-frameworks occurs via dynamic lattice expansions and rearrangements and, some anticipate this chemistry will lead to the next generation of gas sensing and storage materials.⁴ In order to move from new chemistry to functional materials, reactive properties must occur under conditions appropriate for the desired application, creating a need for ways to control properties such as kinetics and reversibility of gas binding. The fundamental research presented in this thesis studies the control of chemical bonding in solids as a means to manipulate properties in materials as well as to contribute to the knowledge of how dynamic processes occur in the solid state. Specifically this research examines structure and bonding effects which define the dynamic properties, including chemical reactions and phase transitions, of certain solid ternary copper halides. The role of Lewis acids on the chemical bonding involved in the reversible gas sorption reactions of solid CuCl and CuMCl_4 ($M = \text{Al}, \text{Ga}$) sorbent materials with small

molecules is explored. This chemistry is closely related to the pairing of copper(I) with more Lewis acidic metals for the removal of CO from gas streams by aromatic solutions of CuAlCl_4 in the COSORB process⁵ and the synthesis of methanol from CO/ H_2 synthesis gas catalyzed by Cu(I)/ZnO.⁶ The crystalline CuMCl_4 system undergoes dramatic framework reconstruction on gas sorption, providing a useful system for studying dynamic changes in solids. The kinetics of these lattice reconstructions in CuMCl_4 are examined to help to develop a mechanistic model for the gas sorption reactions. The even more fundamental dynamic process of melting is considered through a structural study of copper chloride melts. A strong relationship between structure in the solid and molten states is demonstrated which has implications for designing structure in amorphous materials and relates back to the dynamics of solid-state reactions which result in loss of crystallinity. To rationalize the selection of cuprous halide systems for these studies, the relevant properties of metal halides and chemistry of Cu(I) are considered, followed by a brief review of reactions involving solid and small molecules which will provide a context for later discussion of solid state reactivity.

1.2 Metal Halide Networks

Solid oxides are frequently choice materials as catalysts since they provide robust supports for active centers, particularly for high temperature processes. Open framework network structures such as zeolites, offer the additional benefits of high reactive surface area, and size and shape selectivity in catalysis and separations. While their structural chemistry is considerably underdeveloped in comparison to oxides, some metal halides are known to exhibit some similar structural motifs.⁷ For example, open-framework materials similar to

zeolites, have been designed by templating the networks of ZnCl_2 and CuCl .^{8,9} Metal halides are also effective catalysts, as evidenced by their prevalent use in organic synthesis, however, their crystalline solids are generally highly sensitive to moisture and oxygen and are not stable at high temperatures. Furthermore their relatively small lattice energies make them less attractive candidates for many applications. However, the ‘soft’ crystalline lattices of metal halides make them ideal subjects for investigations of phase transitions in solid networks materials, including melting and recrystallization and as well as solid-solid phase transitions, which occur at temperatures low enough to be easily monitored by common experimental techniques. The Martin group has taken advantage of these properties of metal halides to investigate mechanisms for the solid-state phase transition which converts $\beta\text{-CuAlCl}_4$ to $\alpha\text{-CuAlCl}_4$ at temperatures between 100-150°C,¹⁰ and the room temperature gas sorption induced lattice reconstructions of Lewis acid modified copper halide frameworks,^{11,12} which is further explored in this thesis.

1.3 Utility of Cu(I) in Gas Separations

The utility of Cu(I) in separations chemistry lies in its low cost and ability to selectively and reversibly bind unsaturated molecules like olefins, aromatics and carbon monoxide. Copper containing materials have been put to use for gas purification and separations applications including the COSORB process for removing carbon monoxide from gas streams.⁵ In these reactions Cu(I) serves as both a Lewis acid and a Lewis base towards to sorbed species, according to the Dewar-Chatt-Duncanson model that describes the bonding between transition metals and σ -donor/ π -acceptor ligands.¹³ Figure 1.1 depicts the orbital interactions involved in the bonding between Cu(I) and either an olefin or CO molecule. An

empty Cu 4s or s/p hybrid orbital accepts electrons from the ligand HOMO to form a σ -bond. The ligand HOMO participating in the σ -bond consists of the C-C π -bond in the case of the olefin and the weakly anti-bonding lone pair of the CO σ^* -orbital, which is localized on carbon. Formation of the Cu-L σ -bond stabilizes the ligand based orbital while destabilizing the Cu 4s. The olefin π -orbital is more stabilized than the CO σ^* because it exhibits greater spacial overlap with the Cu. Copper can also donate electrons from its HOMO, an orbital from the fully occupied 3d subshell, into the empty π^* -anti-bonding orbital of the olefin or CO. This π -backbonding interaction stabilizes the copper 3d orbital while destabilizing the π^* -orbital of the ligand. The π^* -orbital of CO is of lower energy than that of an olefin, therefore backbonding to CO affords greater stabilization of the Cu 3d orbital.

Binding of Cu(I) to π -coordinating ligands is reported as early as the middle of the nineteenth century,¹⁴ with continuing reports of gas sorption of CO and olefins by acidic or “ammoniacal solutions” of Cu(I) salts in the early 20th century.¹⁵ The first patents suggesting the practical use of Cu(I) solutions in separating CO from gas streams were filed in the 1910s.¹⁶ Later it was discovered that at sufficiently high gas pressures CuCl and CuBr also react in the solid state to bind molecules like ethylene or CO.¹⁷ The patent literature shows attempts to develop Cu(I)/acidic solutions for olefin/paraffin separation by moving from the CuCl/HCl systems reported in earlier work to the more acidic system CuBF₄/HF,¹⁸ however in later half of the century, aromatic solutions of ternary cuprous halides eventually emerged as the more successful candidate. In the 1970s the COSORB process, still in use today, was developed for the removal of low concentrations of CO from gas mixtures and uses CuAlCl₄ dissolved in toluene as the active component.^{5,19} A closely related process known as ESEP, also using a CuAlCl₄-toluene solution, was developed for olefin/paraffin separation, however

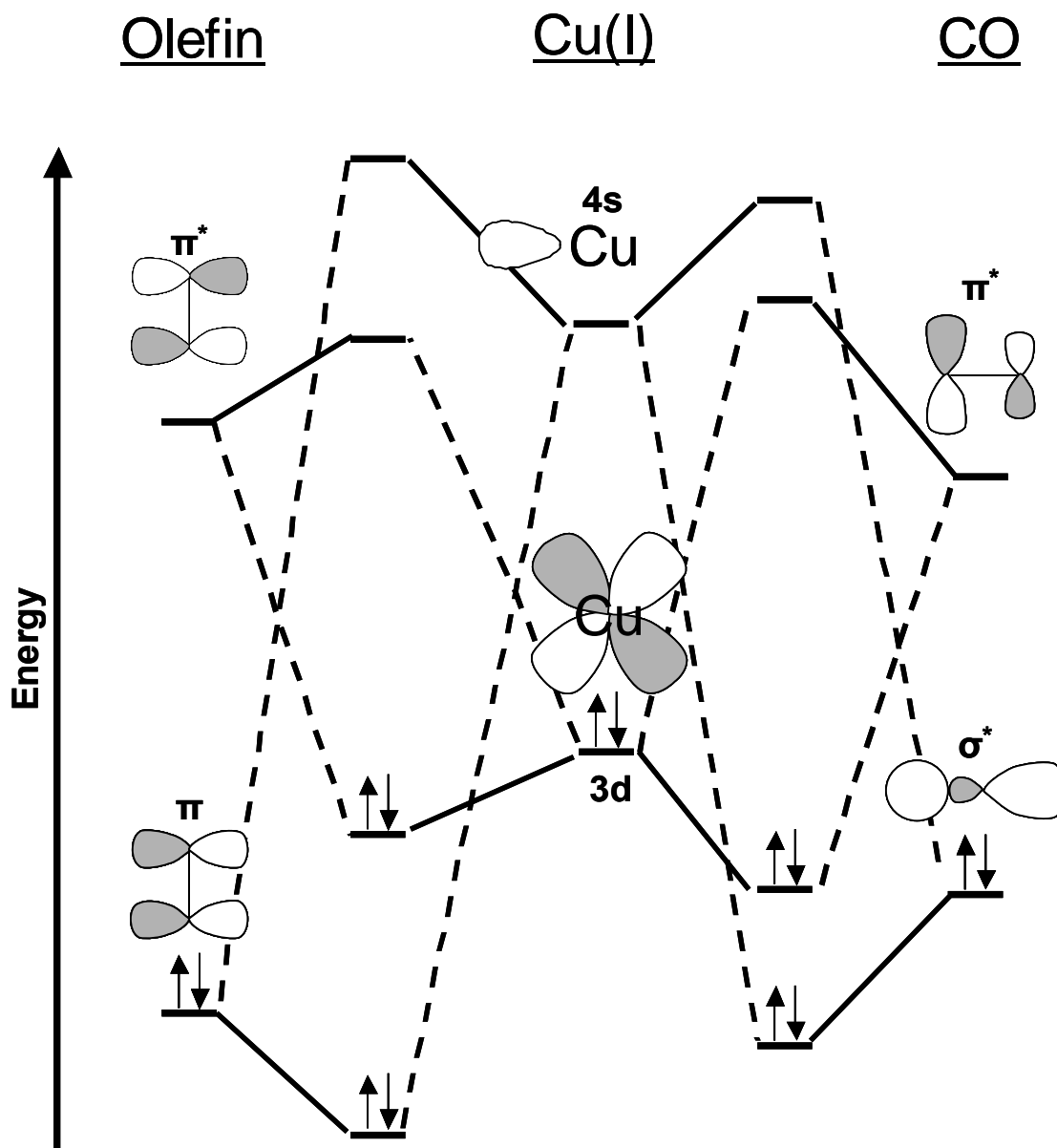


Figure 1.1. A comparison of the Dewar-Chatt-Duncanson model for Cu (I) bonding to olefins and to CO. The lower energy of the CO π^* gives the results in the stronger π -backbonding interaction, while the σ -interaction is stronger with the olefin due to greater spacial overlap.

the process has not been put in to extensive use due in part to the solution's sensitivity to sulfur containing compounds and moisture.²⁰ In some cases the COSORB process has been replaced by pressure swing adsorption in which CO may be selectively removed from gas streams by adsorbents such as carbon supported Cu^+ .^{21,22}

Current technology to replace the expensive cryogenic separation of olefins and paraffins includes the development of facilitated transport membranes. This technology relies on a solubility difference between species in a gas mixture to separate the components. The diffusion of olefins through a membrane is facilitated by the presence of a mobile complexing agent which increases the solubility. Immobilized liquid membranes containing Cu(I) complexing agents have been investigated for this application, however Ag(I) compounds have received more attention in part due to their greater stability with respect to oxidation. Among the most effective liquid membranes studied consist of supported aqueous solutions of CuNO_3 /ethanolamine and AgBF_4 , with the silver complex offering the greater olefin selectivity and sorption capacity. Supported liquid membranes lose their effectiveness over time due to loss of solvent or loss of the mobile complexing agent.²³ In an effort to circumvent these problems olefin transport across immobilized Ag(I) solid polymer supports has also been developed.²⁴ Current challenges to making facilitated transport membranes a more viable technology include developing solid polymer matrices possessing good thermal and mechanical stability.²⁵

1.4 Small Molecule Interactions With Solids

The study of reactions between solids and small molecules is complex, and requires consideration of factors that are typically not a concern in molecular chemistry. This greatly complicates efforts to develop mechanistic models. Understanding the mechanism of solid-state reactions requires knowledge of the bonding interactions between the active sites of the solid and any reactive molecular species as well as any structural changes occurring in the solid itself. Dynamic changes in solids are frequently the origin of their observed properties and have consequences to their utility in practical applications. For example solid-state batteries made with $\text{Li}_x\text{Mn}_2\text{O}_4$ intercalation electrodes, suffer from reduced capacitance after many cycles due to defects in the electrode formed from repeated structural transformations.²⁶ Similarly, composite polymer-ceramic gas separation membranes may fail at elevated temperatures due to cracking caused by thermal expansion.²⁷

To begin to develop atomistic models for the mechanism of gas sorption by solids it is desirable to obtain structural data for both the unreacted material and the gas sorption product. This in itself may be difficult since adducts may only be stable under an excess of the sorbate gas. Furthermore, crystallites often fracture upon gas sorption. Gravimetric analysis offers a convenient technique to study the kinetics of many solid-state sorption or desorption reactions to help validate proposed mechanisms, however it provides no information for structural characterization of any reaction intermediates. *In situ* X-ray diffraction can be used to identify crystalline phases involved in the reaction, however, amorphous liquid or solid intermediates must be characterized by other means. It should also be noted that in many studies of solid-state reactions the possibility of liquid or amorphous intermediates is not addressed nor ruled out as a potential component of the mechanism.²⁸

Among the best studied reactions between solids and small molecules are those involving removal of water from hydrated inorganic salts. While loss of water constitutes a desorption process, the microscopic reverse of such mechanistic processes should provide insight into the mechanism of gas sorption reactions. Dehydration generally occurs on heating, and loss of water ensues beginning at the particle surface, particularly near crystal defects. Crystallization of the dehydrated product phase may be facilitated by the presence of water vapor, resulting in a complex relationship between the kinetics and the partial pressure of water.^{29,30,31} At water partial pressures sufficient to facilitate product crystallization, further water release may be impeded by the layer of dehydrated product phase at the particle surface, resulting in a slower reaction rate. Formation of cracks and channels in the product phase can help provide sites for continued water release to improve the kinetics. By contrast, dehydration under high vacuum is too fast for the lattice to reorganize resulting in amorphous or unstable product phase layers through which further water release is not impeded. Reaction mechanisms can be also complicated by the existence of partially hydrated intermediates, for instance in the case of $\text{MgSO}_4 \cdot 7\text{H}_2\text{O}$,³² or by preferential dehydration from a specific crystallographic face as in $\text{Mn}(\text{CHO}_2)_2 \cdot 2 \text{H}_2\text{O}$ ³³ and $\text{Cu}(\text{HCO}_2)_2 \cdot 4 \text{H}_2\text{O}$.³⁴ Mathematical expressions used to fit the kinetics of dehydration vary depending on the specific inorganic hydrate and include both diffusion controlled and phase-boundary controlled models (as will be discussed further in Chapter 3).²⁸

A reasonably well studied class of gas sorption reactions is the binding of hydrogen by metals or alloys to give metal hydride compounds, which have received recent attention as potential hydrogen storage materials. Similar to the impedance of gas transport induced by the product layer in dehydration reactions, surface oxides and hydroxides on metals inhibit

hydrogen absorption. However, repetition of hydrogen sorption and desorption cycles with a single sample often improve the reaction kinetics for hydride formers; a process known as activation. The origin of the improved sorption kinetics is fragmentation of the metal hydride particles on cycling, yielding smaller particles (thus greater surface area) and fresh metal surface free of oxides and hydroxides. Brittle metal hydrides, such as those formed from LaNi_5 or TiFe , exhibit significant fragmentation and therefore have increased hydrogen sorption rates after repeated cycling, while ductile metal hydrides, do not fragment as well and their hydrogen sorption kinetics do not change significantly with cycling.³⁵ The kinetics also vary with hydrogen pressure and several functions have been used to model the pressure dependence of hydrogen sorption reaction rates.³⁶

Considerable attention has recently been given to gas sorption by the metal-organic framework (MOFs) materials. Typical MOF materials capable of gas sorption are built from molecular metal-organic units that form crystalline networks through weak intermolecular forces such as π -stacking or hydrogen-bonding. While many MOFs are microporous, their weak intermolecular bonding forces affords significant lattice flexibility that is not possible in rigid gas sorption materials like zeolites and activated carbons. Their lattice flexibility allows some MOF structures to readily undergo dynamic expansions and reconstructive reactions to reversibly accommodate guest molecules, making them candidates for gas storage, separation and sensing applications. The flexibility gives rise to properties such as the hysteretic physisorption of hydrogen discovered by Thomas and coworkers for $\text{Ni}_2(\text{bipy})_3(\text{NO}_3)_4$ based structures, in which pores in the solid expand to accommodate hydrogen sorption.³⁷ Other structures form adduct phases by reversible binding of larger molecules through formation of chemical bonds. The structure of the adsorbent need not be

microporous since absorption of these larger molecules is often afforded by either lattice expansions or complete structural transformations.^{38,39,40}

Often structural transformations associated phase transitions and reactions occur completely in the solid state, however, in some cases the reaction may proceed by a liquid intermediate. For example, the solid-vapor reaction of $[\text{Cd}(\mu_2\text{-}N,O\text{-}p\text{-NH}_2\text{C}_6\text{H}_4\text{SO}_3)_2(\text{H}_2\text{O})_2]$ powder with alkylamines may proceed by dissolution of the parent material followed by subsequent crystallization of the adduct phase.⁴¹ The possibility of liquid reaction intermediates may be difficult to observe and complicate mechanistic investigations. Since both liquids and solids are condensed phases of matter, some kinetic models for solid-state reactions can also apply to molten phases, however kinetic effects of processes like particle fracturing do not play a role in reactions of liquids. While commonly thought of as a randomly organized state of matter, liquids are also known to possess structural order on length scales beyond nearest neighbor contacts, albeit without the long-range ordering present in crystalline materials, and the short-range contacts between atoms of a compound in the solid and liquid state are often quite similar.⁴² As such the bonding interactions should not change greatly going from the solid to the liquid state, which would suggest that atomistic models for a gas sorption or desorption reaction might be applicable to either condensed phase.

1.5 Scope

The work presented here focuses on the reactivity of solid copper (I) halides with small molecules and the structure of molten copper chlorides. The gas sorption chemistry of CuMCl_4 ($M = \text{Al, Ga}$) with CO is examined in detail in Chapter 1, with a focus on the effects

of the Lewis acidic species AlCl_3 and GaCl_3 on the competitive bonding between copper (I) and olefin and carbonyl ligands. Also, in this chapter the atomistic description of the sorptive reconstruction mechanism is further developed with respect to the lattice rearrangement in CuMCl_4 that occurs on gas sorption of ethylene or CO. Chapter 2 turns to the examination of structure in molten metal halides by neutron and X-ray diffraction. A series of ACu_2X_3 salts (A = monovalent templating cation) are investigated in order to gain understanding of atom level structure in the liquid state and to develop principles for designing structural features in amorphous materials. It is shown that a significant extent of covalent bonding in molten ACu_2Cl_3 compounds is preserved into the liquid state. This condensed matter understanding of liquid structure in turn has consequences for Chapter 3, in which it is shown that near 35°C gas sorption of ethylene by CuAlCl_4 proceeds through a liquid intermediate. A kinetic study in Chapter 3 is used to assess the validity of the sorptive reconstruction mechanism proposed for the CuAlCl_4 /ethylene and CuAlCl_4 /CO gas sorption reactions.

1.6 References

- (1) (a) "Energy and Transportation: Challenges for the Chemical Sciences in the 21st Century." Organizing Committee for the Workshop on Energy and Transportation, Committee on Challenges for the Chemical Sciences in the 21st Century. National Research Council 2003. (b) "Materials in the New Millennium: Responding to Society's Needs." Proceedings of the 2000 National Materials Advisory Board Forum, National Research Council, 2001.
- (2) Rao, C. N. R.; Gopalakrishnan, J. *New Directions in Solid State Chemistry*, Cambridge University Press: New York, 1997.
- (3) (a) Cheetham, A. K.; Rao, C. N. R. *MRS Bulletin*, **2005**, *30*, 93-98. (b) Biradha, Kumar, *Cryst. Eng. Comm.* **2003**, *5*, 374-384. (c) Bedard, R. L. *AIChE Journal*, **1999**, *45*, 2474-2476.
- (4) Fletcher, A. J.; Thomas, K. M.; Rosseinsky, M. J. *J. Solid St. Chem.* **2005**, *178*, 2491-2510.
- (5) (a) Haase, D. J., Walker, D. G. *Chem. Eng. Prog.* **1974**, *70*, 74-77. (b) Long, R. B.; Caruso, F. A.; Walker, D.G. "Monomere Bimetellsalze sowie Verfahren zu ihrer Herstellung and Verbindung." German Patent DE 1,944,405, **1968**. (c) Turnbo, R. G. Process for the Preparation of Bimetallic Salt Complexes *U.S. Patent* 3,857,869; **1974**. (d) Sudduth, J. R.; Keyworth, D. A. "Process for the Purification of Gas Streams" *U.S. Patent* 3,960,910, **1975**. (e) Walker, D. G. *Chemical Technology*, **1975**, *5*, 308-311.
- (6) (a) Lee, S. *Methanol Synthesis Technology*; CRC Press: Boca Raton, FL, 1990; pp 1-22. (b) Cheng, W. H.; Kung, H. H. *Methanol Production and Use*; Cheng, W. H., Kung, H. H., Eds.; Marcel Dekker: New York, 1994; pp 1-22.

- (7) Martin, J. D.; Dattelbaum, A. M.; Thornton, T. A.; Sullivan, R. M.; Yang, J.; Peachy, M. T. *Chem. Mat.* **1998**, *10*, 2699-2713.
- (8) Martin, J. D.; Greenwood, K. B.; *Angew. Chem., Int. Ed. Engl.* **1997**, *36*, 2072-2075.
- (9) Debord, J. R. D.; Lu, Y.; Warren, C.; Haushalter, R. C.; Zubieta, J. *Chem Comm.* **1997**, 1365-6.
- (10) (a) Martin, J. D.; Leafblad, B. R.; Sullivan, R. M.; Boyle, P. D. *Inorg. Chem.* **1998**, *37*, 1341-1346 (b) Haiming L.; Sullivan, R. M.; Hanson, J. C.; Grey, C. P.; Martin, J. D. *J. Am. Chem. Soc.* **2001**, *123*, 7564-7573.
- (11) Sullivan, R. M.; Liu, H.; Smith, S.; Hanson, J. C.; Osterhout, D.; Ciraolo, M.; Grey, C. P.; Martin, J. D. *J. Am. Chem. Soc.* **2003**, *125*, 11065-11079.
- (12) Dattelbaum, A. M.; Martin, J. D. *Polyhedron*, **2006**, *25*, 349-359.
- (13) (a) Dewar, M. *Bull. Soc. Chim. Fr.* **1951**, *18*, C71-79. (b) Chatt, J.; Duncanson, L. *J. Chem. Soc.* **1953**, 2939-2947.
- (14) (a) Leblanc, F. C., *R. Acad. Sci. Paris*, **1850**, *30*, 483. (b) Berethelot, M., *Ann. Chim. Phys.*, **1856**, *346*, 364.
- (15) (a) Manchot, W. *Oesterreicheische Chemiker-Zeitung* **1911**, *14*, 264-265. (b) Hainsworth, W. R.; Titus, E. Y. *J. Am. Chem. Soc.*, **1921**, *43*, 1-11. (c) Larson, A. T.; Teitsworth, C. S. *J. Am. Chem. Soc.* **1922**, *44*, 2878-2885. (d) Kropf, A. *Angew. Chemie* **1922**, *35*, 451-452. (e) Moser, L.; Hanika, F. *Z. Analyt. Chem.* **1926**, *67*, 448-456. (f) Gump, W.; E. I. *J. Ind. Eng. Chem.*, **1930**, *22*, 382-384.
- (16) (a) Badische. "Removing carbon monoxide from gases." Great Britain patent GB 1409271, **1914**. (b) Badische. "Removing Carbon monoxide from gas mixtures." German patent DE 282505, **1913**. (c) Badische. "Separating carbon monoxide from gas mixtures

with the aid of cuprous oxide compounds.” German patent DE 289649, **1914**. (d) Watts, H. G. “Separating ethylene from its homologs.” U.S. Patent 1977659, **1934**.

(17) (a) Tropsch, H.; Mattox, W. J. *J. Am. Chem. Soc.* **1935**, *57*, 1102-1103 (b) Gilliland, E. R.; Seebold, J. E.; FitzHugh, J. R.; Morgan, P. S. *J. Am. Chem. Soc.*, **1939**, *61*, 1960-1962. (c) Gilliland, E. R.; Bliss, H. L.; Kip, C. E. *J. Am. Chem. Soc.*, **1941**, *63*, 2088-2090. (d) Wagner, O. H. *Anorg. Allg. Chem.* **1931**, *196*, 364-373.

(18) McCaulay, D. A. “Copper Fluoroborate-Aromatic Complexes and Preparation Thereof.” U. S. Patent 2,953,589, **1960**.

(19) Safarik, D. J.; Eldridge, R. B. *Ind. Eng. Chem. Res.* **1998**, *37*, 2571-2581.

(20) Guitierrez, A. P.; Haase, D. J.; Keyworth, D. A.; Walker, D. G.; Klein, D. L. “ESEP, A Process for the Recovery of Ethylene.” Presented at the 175th National Meeting of the American Chemical Society, Anaheim, CA, March 12-17, 1978.

(21) Dutta, N. N.; Patil, G. S. *Gas Sep. Purif.* **1995**, *9*, 277-283.

(22) (a) Zue, L. Q.; Tu, J. L.; Shi, Y. J. *Gas Sep. Purif.* **1991**, *5*, 173-176. (b) Kasuye, F.; Tsuji, T. *Gas Sep. Purif.* **1991**, *5*, 242-246.

(23) Noble, R. D.; Koval, C. A.; Pellegrino, J. J. *Chem. Eng. Prog.* **1989**, *85(3)*, 58-70.

(24) (a) LeBlanc, O. H.; Ward, W. J.; Matson, S. L.; Kimura, S. G. *J. Membrane Sci.*, **1980**, *6*, 339-343. (b) Ho, W. S.; Dalrymple, D. C. *J. Membrane Sci.*, **1994**, *91*, 13-25. (c) Kang, Y-S.; Won, J-O.; Hong, S-U.; “Solid state facilitated transport separation membranes using polymer electrolytes for alkene separation.” U.S. Patent 2001013273, **2001**.

(25) Su, C.; Kuraoka, K.; Yazawa, T. *J. Sol-Gel Sci. and Tech.* **2005**, *33*, 327-332.

(26) Bruce, P. G.; Armstrong, A. R.; Huang, H. *J. Power Sources* **1997**, *68*, 19-23.

(27) Rezac, M. E.; Koros, W. J.; Miller, S. J. *Sep. Sci. Technol.* **1995**, *30*, 2159-2171.

- (28) *Reactions in the Solid State, Comprehensive Chemical Kinetics*; Bamford, C. H.; Tipper, C. F. H. Eds.; Elsevier: Amsterdam, 1980; Vol. 22.
- (29) Topley, B.; Smith, M. L. *J. Chem. Soc.*, **1935**, 321-325.
- (30) Volmer, M.; Seydel, G. *Z. Phys. Chem.* **1937**, A179, 153-171.
- (31) W. E. Garner (Ed.), *Chemistry of the Solid State*, Butterworth, London, 1955, p.232.
- (32) (a) Lallemand, M.; Wattle-Marion, G. *C. R. Acad. Sci.* **1967**, 264, 2030-2033 (b) Lallemand, M.; Wattle-Marion, G. *C. R. Acad. Sci.* **1967**, 265, 627-630.
- (33) (a) Eckhardt, R. C.; Flanagan, T. B. *Trans. Faraday Soc.*, **1964**, 60, 1289-1298. (b) Clarke, T. A.; Thomas, J. M. *J. Chem. Soc. A*, **1969**, 2227-2230.
- (34) Fitchte, P. M.; Flanagan, T. B. *Trans. Faraday Soc.* **1971**, 67, 1467-1479.
- (35) P. S. Rudman *J. Less Common Metals*, **1983**, 89, 93-110.
- (36) Ron, M. *J. Alloys and Compounds* **1999**, 283, 178-191.
- (37) Zhao, X.; Xiao, B.; Fletcher, A. J.; Thomas, K. M.; Bradshaw, D.; Rosseinsky, M. J. *Science* **2004**, 306, 1012-1015.
- (38) (a) Albrecht, M.; Lutz, M.; Spek, A. L.; van Koten, G. *Nature*, **2000**, 970-974. (b) Albrecht, M.; Lutz, M.; Schreurs, A. M. M.; Lutz, E. T. H.; Spek, A. L.; van Koten, G. *J. Chem. Soc., Dalton Trans.* **2000**, 3797-3804.
- (39) Mäkinen, S. K.; Melcer, N. J.; Parvez, M.; Shimzu, G. K. H. *Chem. Eur. J.*, **2001**, 7, 5176-5182.
- (40) van Poppel, L. H.; Bott, S. G.; Barron, A. R. *J. Am. Chem. Soc.*, **2003**, 125, 11006-11017.
- (41) Zhou, J-S.; Cai, J.; Wang, L.; Ng S-W. *J. Chem. Soc., Dalton Trans.*, **2004**, 1493-1497.
- (42) Rovere, M.; Tosi, M. P. *Rep. Prog. Phys.* **1986**, 1001-1081.

Chapter 2:
**Sorptive Reconstruction of CuMCl_4 (M = Al and Ga) Upon Small
Molecule Binding and The Competitive Binding of CO and
Ethylene.**

*Michael D. Capracotta, Roger M. Sullivan and James D. Martin**

Department of Chemistry, North Carolina State University, Raleigh, NC 27695-8204

(submitted to *J. Am. Chem. Soc.* in 2006)

Abstract

Carbonyl adducts to CuMCl_4 ($M = \text{Al}$ and Ga) have been characterized by single crystal and/or powder X-ray diffraction, IR and Diffuse Reflectance UV/Vis spectroscopy. β -(CO) CuAlCl_4 , $\mathbf{a} = 6.8752(3)$, $\mathbf{b} = 7.0092(3)$, $\mathbf{c} = 8.7362(3)$, $\alpha = 81.798(2)$, $\beta = 69.646(2)$, $\gamma = 85.723(2)$, $P\bar{1}$, $Z = 2$; β -(CO) CuGaCl_4 , $\mathbf{a} = 6.877(1)$, $\mathbf{b} = 7.015(1)$, $\mathbf{c} = 8.759(2)$, $\alpha = 81.00(2)$, $\beta = 69.45(1)$, $\gamma = 85.73(2)$, $P\bar{1}$, $Z = 2$. Up to two equivalents of carbon monoxide ($\sim 200 \text{ cm}^3/\text{g}$ relative to stp) are sorbed at room temperature, with equilibrium binding pressures of below 0.5 atm of CO. The carbonyl bonding is shown to be non-classical, implicating the dominance of σ -bonding and absence of π -back bonding. Analysis of the crystalline structures of the parent and adduct phases provide an atomistic picture of the sorptive reconstruction reaction. Comparison of the reactivity of CO and ethylene with these CuMCl_4 materials, as well as other copper(I) halide compounds that exhibit classical and non-classical modes of bonding, demonstrate the ability to tune the reactivity of the crystalline frameworks with selectivity for carbon monoxide or olefins, respectively.

2.1 Introduction

Compounds of copper (I) are well known to be useful in separations and catalysis applications due to their ability to readily bind small molecules such as olefins, aromatics and carbonyls.^{1,2,3,4,5,6,7} Among these, systems that combine Cu(I) with more Lewis acidic metals are the active components in several chemically and economically important processes. For instance Cu(I)/ZnO catalyzes the synthesis of methanol from syngas,⁸ and aromatic solutions of CuCl and AlCl₃ selectively remove carbon monoxide from gas mixtures in the COSORB process.⁹ Despite the significance of these reaction systems, details of the small molecule binding remain poorly characterized both with respect to the identity of the active copper species and the specific role of any additional Lewis acid. We have previously described the solid-state sorptive reconstruction of CuAlCl₄ upon reaction with ethylene from an atomistic perspective, in which up to two molar equivalents can be reversibly bound under mild conditions. We demonstrated that in contrast to CuCl, which exhibits a room temperature ethylene dissociation pressure of 8 atm,¹⁰ addition of AlCl₃ facilitates ethylene binding to Cu(I) resulting in dissociation pressures of below 20 Torr. Unlike ethylene, carbon monoxide is well known to bind to CuCl.^{11,12} Though sorption is facile for solutions of CuCl in aqueous and organic solvents under one atmosphere of CO,¹³ sorption into crystalline CuCl requires higher pressures ranging from 3 to 100 atm, depending on particle size.^{12,14} The common adduct (CO)CuCl, formed from either solution or solid state reactions, exhibits a room temperature dissociation pressure of 0.5 atm. Based on their respective dissociation pressures CO appears to bind more strongly to CuCl than does ethylene, consistent with a classical carbonyl bonding model.¹⁵ However, when in a Lewis acidic environment, CO and olefin binding to Cu(I) has been observed to exhibit non-

classical, i.e. dominated by σ -interactions with little to no π -back bonding, behavior.^{2,5,16,17,18,19} Given that CO is a better π -acceptor than ethylene but a slightly weaker σ -donor, a study of the comparative binding of CO and ethylene to CuCl, and CuMCl₄ (M = Al and Ga) was initiated to probe bonding and mechanistic details of small molecule binding to Cu(I) in a Lewis acidic coordination environment. Specifically in this report we describe the pressure resolved synchrotron diffraction and spectroscopic characterization of one and two equivalent carbonyl adducts to CuMCl₄ (M = Al and Ga), as well as the single crystal structure of the one-equivalent adduct, (CO)CuAlCl₄. These data, along with our previous report on ethylene binding demonstrate the ability to fine tune the specific reactivity of Cu(I) based materials.

2.2 Background

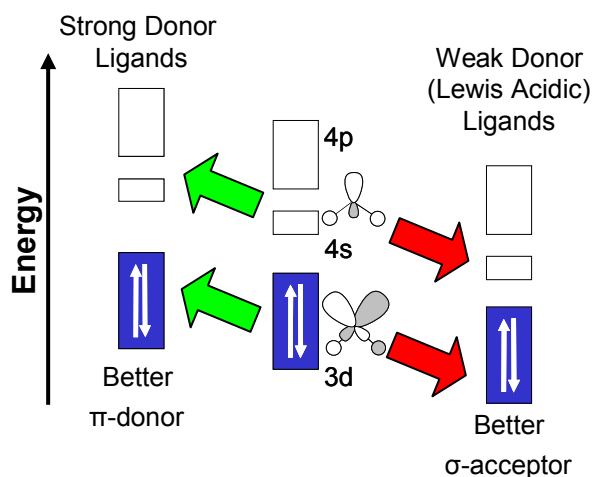
The electronic structure of Cu(I) makes it well suited to be the active site for reversible binding of small molecules like olefins and carbon monoxide. Since copper has an electronegativity similar to silicon, Cu-Cl bonds must have significant covalent character. With a d^{10} -electronic configuration, the relatively high lying HOMO consists of M-L σ^* character. However, the empty s- and p-orbitals of copper (I), also of M-L σ^* character, are quite low in energy resulting in a very small HOMO-LUMO gap. These low-lying empty metal-based orbitals readily mix with the HOMO in a second-order Jahn-Teller fashion, which results in an extensive geometric flexibility of the copper (I) coordination sphere.²⁰ These frontier orbitals also dictate the reactivity of many copper complexes. In both four and three coordinate geometries the M-L σ^* HOMO possess appropriate symmetry to back-bond in a π -fashion, whereas the symmetry of the metal s/p based LUMO is appropriate for σ -

acceptor interactions. Strong ancillary donor ligands destabilize all of these orbitals, which enhance the metal's ability to π -back-bond and make it a less effective σ -acceptor, as shown in the left portion of Scheme I. Nature has exploited this mode of binding enhancement with strong amine-type ligands bound to copper in ethylene binding metalloenzymes.²¹ However, in the presence of weak donor ligands, such as the conjugate base of strong Lewis acids (i.e. AlCl_4^- , AsF_6^-), these frontier orbitals are stabilized providing a better σ -acceptor configuration with little to no back-bonding ability,^{2,5,16-19} represented on the right hand side of Scheme I and described as non-classical.

The carbonyl stretching frequency of carbon monoxide ligand bound to a metal center is a sensitive measure of the relative classical/non-classical nature of ligand binding.¹⁶⁻¹⁹ With its HOMO being a σ -lone pair with weak C-O anti-bonding character and its LUMO being the C-O π^* orbital, classical M-CO binding (i.e. with significant π -back-bonding) results in a decrease of the CO stretching frequency from that of free CO, 2143 cm^{-1} . By contrast non-classical bonding (i.e. predominately σ -bonding) results in a small increase in the CO stretching frequency. (It is important to recognize that π -back-bonding into the CO π^* orbital has a much greater effect on the ν_{CO} than does σ -donation from the weakly anti-bonding CO lone pair). As observed from the tabulation of CO stretching frequencies presented in Table 1, chloride ligands for Cu(I)-CO complexes create an environment that appears to sit very nearly at the classical/non-classical boundary, with $\nu_{\text{CO}} = 2127$ for $(\text{CO})\text{CuCl}$. Interestingly, at 100 K, a thin film of $(\text{CO})\text{CuCl}$ exhibits a slight strengthening of the $\nu_{\text{CO}} = 2135$ (Table 1f),²² and matrix isolating the $(\text{CO})\text{CuCl}$ complex results in non-classical bonding with $\nu_{\text{CO}} = 2157$ cm^{-1} .²³ These data indicate very minimal $d\pi\text{-CO}\pi^*$ interaction for the chloride complex. The addition of donor ligands, such as amines, to a

copper chloride carbonyl complex (Table 1 a-c) pushes the Cu-CO bonding toward the classical mode. Placing the copper (I) center in a more Lewis acidic environment such as in a zeolite (Table 1 m,n) or complexed with a non-coordinating anion (Table 1 o-q) clearly shifts

SCHEME 1



copper-carbonyl bonding to the non-classical motif. The matrix isolated cation $[(\text{CO})\text{Cu}]^+$ (Table 1 r) provides the limiting value for non-classical binding.

The ligand environment thus clearly tunes the binding affinity of copper (I). Many Lewis basic donor ligands exist (i.e. amines and phosphines) that enhance the classical mode of bonding (eq. 1)



By contrast, tuning a complex toward non-classical bonding is more complicated, since Lewis acidic ligands (with the exception of π -acids) essentially do not exist. Here we utilize a

strategy whereby a common-ion Lewis acid tunes the ligand field around the metal center (eq. 2) so as to enhance non-classical bonding.



The reactivity of copper chloride toward CO and ethylene in the presence of the common-ion Lewis acids AlCl_3 and GaCl_3 clearly demonstrate this enhanced non-classical bonding. Mono- and di-carbonyl adduct phases $(\text{CO})\text{CuMCl}_4$, **1-CO_M**, and $(\text{CO})_2\text{CuMCl}_4$, **2-CO_M**, (M = Al and Ga) have been characterized by gravimetric and volumetric sorption, FTIR and UV/Vis spectroscopy, and pressure resolved synchrotron diffraction studies. These data, correlated with previously reported data, demonstrate the ability to fine-tune the copper (I) reactivity so as to favor carbon monoxide vs. olefin binding. The structural data provides further insight into our ongoing mechanistic study of the reconstruction of the CuMCl_4 lattice upon small molecule sorption.

Table 2.1. Summary of Cu(I)-monocarbonyl stretching frequencies.

	Material/Complex	ν_{CO} (cm⁻¹)	Ref
a.	(dipyam)Cu(CO)Cl ⁱ	2069	24
b.	(en)Cu(CO)Cl ⁱⁱ	2080	25
c.	DCEACu(CO)Cl ⁱⁱⁱ	2096	26
d.	(CO)CuCl (MeOH solution)	2070	13c
e.	(CO)CuCl	2127	13b
f.	(CO)CuCl (100K)	2134-2136	22
g.	Cu(CO)Cl (Ar matrix)	2157	23
h.	(CO)CuAlCl ₄	2156	this work
i.	(CO)CuGaCl ₄	2156	This work
j.	Cu(I)/ZnO	2103	27
k.	Cu ₂ O	2127	28
l.	Cu ₂ O/SiO ₂	2132	28
m.	Cu(I)-ZSM-5	2157	29
n.	Cu(I)-Mordenite	2159	30
o.	(CO)Cu(O ₂ CCF ₃)	2155	31
p.	[(CO)Cu][1-Et-CB ₁₁ F ₁₁]	2175	32
q.	[(CO)Cu][AsF ₆]	2178	17
r.	[(CO)Cu] ⁺ Ne/CO matrix	2234	33

i. dipyam = 2,2'-dipyridylamine, ii. en = ethylenediamine, iii. DCEA = bis(2-cyanoethyl)amine.

2.3 Results

Adsorption Isotherm Measurements

Volumetric and gravimetric experiments were performed to probe the sorptive capabilities of CuAlCl_4 and CuGaCl_4 with CO. Exposure of a bulk sample of CuAlCl_4 to 1500 Torr of carbon monoxide at room temperature results in loss of the material's characteristic blue-green luminescence,³⁴ and uptake of approximately 1 equivalent of CO, as measured gravimetrically. Up to about one atmosphere of CO pressure, the material remains solid. However, upon increasing the CO pressure, a eutectic melt-type behavior is observed with the fraction of amber colored liquid increasing with increasing CO pressure. Exposing the solid or liquid products to dynamic vacuum results in a reversion to a solid phase. The return of luminescence upon desorption is indicative of reformation of the parent CuAlCl_4 . However, even after evacuation for several hours at room temperature, gravimetric analysis shows that approximately 0.2-equivalents of CO remain sorbed. Heating the solid to its melting temperature, approximately 45°C, under vacuum removes all the remaining carbon monoxide with quantitative reformation of crystalline $\alpha\text{-CuAlCl}_4$ (m.p. = 235°C). Carbon monoxide can also be removed from the solid adduct by grinding under an N_2 atmosphere in a glove box. Similar results are observed by exposing CuGaCl_4 to CO, however, no liquid phase is observed upon CO sorption and the adduct phases decompose prior to melting.

Representative examples of volumetric sorption/desorption isotherms are given in Figures 2.1 and 2.2, plotted as the number of moles CO sorbed per mole of CuMCl_4 vs. the equilibrated pressure of CO. Sorption isotherms were measured using various sized steps in carbon monoxide pressure from 50 to 600 Torr in an attempt to access multiple reaction pathways as observed previously for ethylene sorption. However, neither the initial exposure

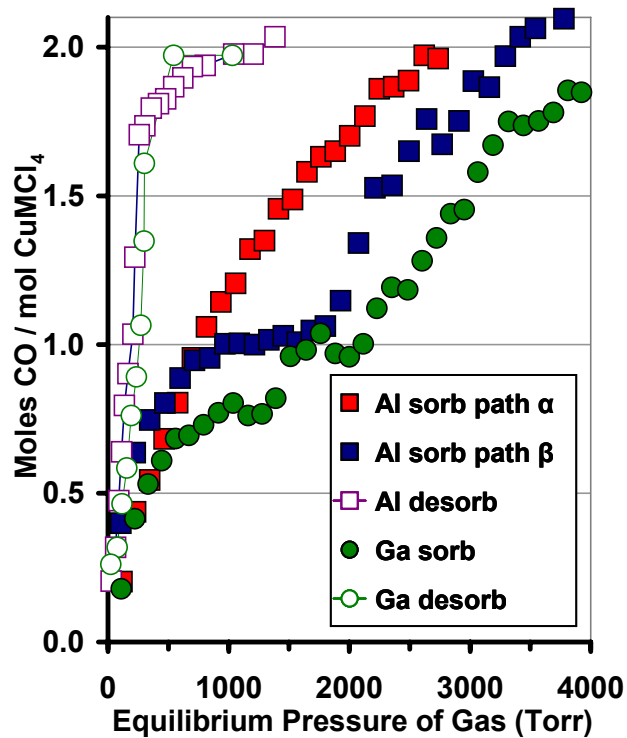


Figure 2.1. Representative sorption-desorption isotherms for the systems $\text{CuAlCl}_4 + \text{CO}$ and $\text{CuGaCl}_4 + \text{CO}$.

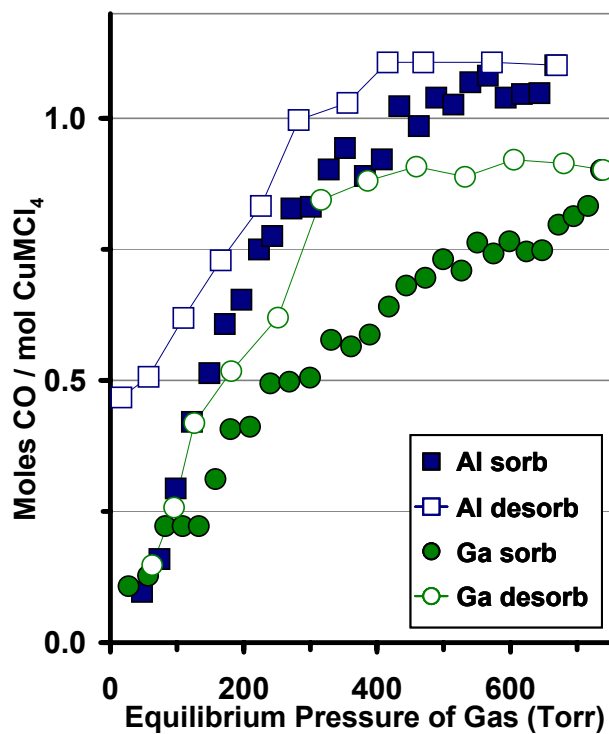


Figure 2.2. Sorption-desorption isotherms for the one equivalent phases from the $\text{CuAlCl}_4 + \text{CO}$ and $\text{CuGaCl}_4 + \text{CO}$ systems.

pressure nor size of the sorption steps appeared to have any significant effect on the sorption reaction. Nevertheless, two characteristic patterns of reactivity, described as path- α and - β , respectively, were observed for the sorption isotherms into CuAlCl_4 , shown in Figure 2.1. The β -path exhibits a plateau at approximately one equivalent and around one atmosphere of CO pressure, consistent with the formation of $(\text{CO})\text{CuAlCl}_4$, **1-CO_{Al}**, followed by gradual sorption to two equivalents of CO, to form $(\text{CO})_2\text{CuAlCl}_4$, **2-CO_{Al}**, at an equilibrium pressure of 4000 Torr. By contrast, the α -path appears to form the higher adduct at lower pressures and does not exhibit a plateau at one-equivalent. Five out of ten isotherm measurements were observed to follow each type reaction path. We have not yet been able to determine what factors determine which reaction path will be followed. Carbon monoxide sorption into CuGaCl_4 has only been observed to follow the stepwise β -type path. For sorption into CuGaCl_4 , the initial plateau occurs with only about 0.75 equivalents of CO sorbed, assigned to the incomplete formation of **1-CO_{Ga}**. With increasing pressure, however, two equivalents of CO are sorbed when the equilibrium pressure of 4000 Torr is achieved, corresponding to the formation of **2-CO_{Ga}**. Similar experiments were performed with CuCl (data not shown), but no sorption of CO was observed up to equilibrated pressures of 4000 Torr, consistent with literature reports.^{12,14}

Significant hysteresis is observed between the sorption and desorption of CO into both CuMCl_4 materials. No carbon monoxide desorption is observed until pressures below one atmosphere are achieved. Desorption from **2-CO_{Al}** commences at an equilibrium pressure of about 700 Torr. Desorption from **2-CO_{Ga}** occurs at a slightly lower pressure, 500 Torr, although a precise comparison is outside the limits of our experiential apparatus. A second series of sorption/desorption experiments in which only the one-equivalent adducts

were allowed to form (Figure 2.2) demonstrates less dramatic hysteresis than was observed for the 2-equivalent adducts. The desorption pressure for **1-CO_{Al}** is about 360 Torr and that for **1-CO_{Ga}** is about 330 Torr. Again while the experimental apparatus does not allow precise measurement of the desorption pressure, repeatedly, **1-CO_{Ga}** samples retain CO to slightly lower pressures than does **1-CO_{Al}**. In these room temperature experiments, complete desorption is never achieved, leaving between 0.15 to 0.45 moles of sorbed gas depending on the individual experiment.

Synchrotron Powder X-ray Diffraction

In situ synchrotron powder X-ray diffraction experiments were conducted to identify the phases present in the reactions of CuAlCl₄, CuGaCl₄ and CuCl with carbon monoxide. As there is a significant pressure gradient along the capillary tubes used in these experiments, it is not possible to draw a precise comparison between the sorption isotherms and the diffraction measurements. The pressure gradient can be inferred by the observation that more carbon monoxide rich products are present at the end of the capillary closest to the gas exposure. This problem is somewhat alleviated by mixing the reactive metal halide with ground fused silica as an inert matrix that helps allow the CO to diffuse through the capillary. Also melting the CuAlCl₄ in the presence of the silica matrix, followed by subsequent cooling to room temperature, gives a thin film of material over the ground silica that increases its surface area and promotes reaction. In experiments without the fused silica, product phases were normally only observed within the first 3 mm of the sample, while little or no reaction occurred deeper into the capillary. A summary of the characteristic low angle reflections that identify each of the phases is given in Table 2.2.

Starting with a $\text{CuAlCl}_4/\text{SiO}_2$ mixture cooled to 15°C and under vacuum, the pressure of CO was gradually increased over a period of approximately 90 minutes. Figure 2.3 shows the time/pressure resolved X-ray diffraction data for this reaction. At a pressure of 860 Torr (Figure 2.3b), diffraction peaks indicative of $\alpha\text{-1-CO}_{\text{Al}}$ are observed along with peaks corresponding to 2-CO_{Al} . The intensity of the peaks corresponding to $\alpha\text{-1-CO}_{\text{Al}}$ grow with increasing pressure until pressures of greater than 2000 Torr are achieved (Figure 2.3e), at which point they begin to decrease in intensity. As the pressure is increased, peaks corresponding to CuAlCl_4 and $\alpha\text{-1-CO}_{\text{Al}}$ continue to diminish, while peaks for 2-CO_{Al} grow only slightly. Further progress of the reaction to the maximum experimental pressure of 4500 Torr shows an increase in the amorphous background consistent with the formation of a eutectic melt. In sorption experiments with only CuAlCl_4 loaded in the capillary (i.e. no ground fused silica), only a partial reaction to form $1\text{-(CO)}_{\text{Al}}$ is observed even at the maximum experimental pressure of gas. Such reactions normally exhibited evidence of the $\beta\text{-1-CO}_{\text{Al}}$ phase (Figure 2.4). Sorption experiments into CuGaCl_4 exhibit similar behavior, except that reactions do not proceed as far toward completion under the accessible CO pressure, and no sample melting is observed (Figure 2.5). Here, $\beta\text{-1-CO}_{\text{Ga}}$ is the only product initially observed, and partial formation of 2-CO_{Ga} is only observed at higher CO pressure. Unfortunately we have not been able to achieve complete formation of $\beta\text{-1-CO}$ prior to formation of 2-CO as would seem to be implied by the β -path sorption isotherm of Figure 2.1.

Table 2.2. Characteristic Low Angle Reflections for identifying Phases in Powder X-ray Diffractograms.

Phase	hkl	Q (\AA^{-1})
α -CuAlCl ₄	100	1.15
	002	1.24
	101	1.31
α -(CO)CuAlCl ₄ α -1-CO _{Al}	100	0.59
	110	1.01
	011	1.06
β -(CO)CuAlCl ₄ β -1-CO _{Al}	001	0.77
	100	0.97
	101	1.02
(CO) ₂ CuAlCl ₄ 2 -CO _{Al}	010	0.53
	100	0.68
	-110	0.94

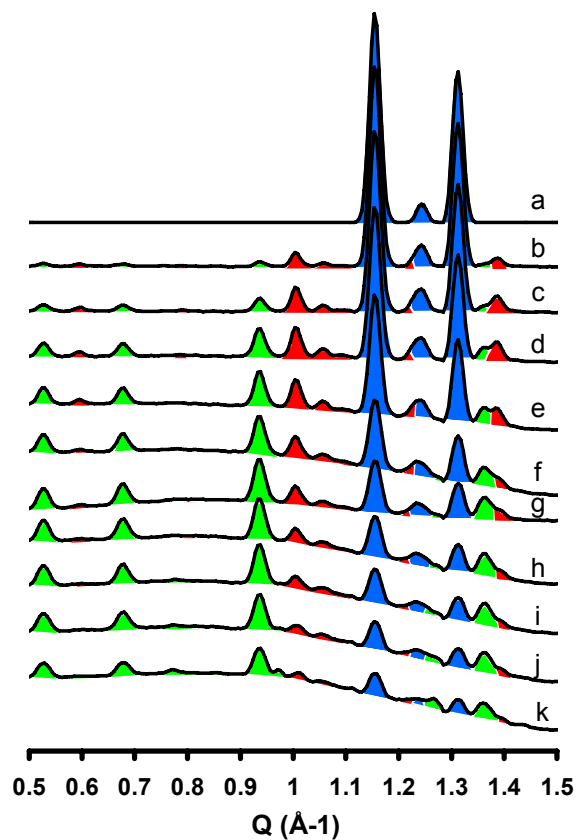


Figure 2.3. Variable pressure x-ray diffraction showing the conversion of α -CuAlCl₄ to (CO)₂CuAlCl₄ at (a) 0; (b) 860; (c) 1000; (d) 1500 (e) 2000; (f) 2500; (g) 3000; (h) 3500; (i) 4000; (j&k) 4500 Torr of CO. The powder patterns are color coded blue for α -CuAlCl₄, red for α -(CO)CuAlCl₄ and for (CO)₂CuAlCl₄.

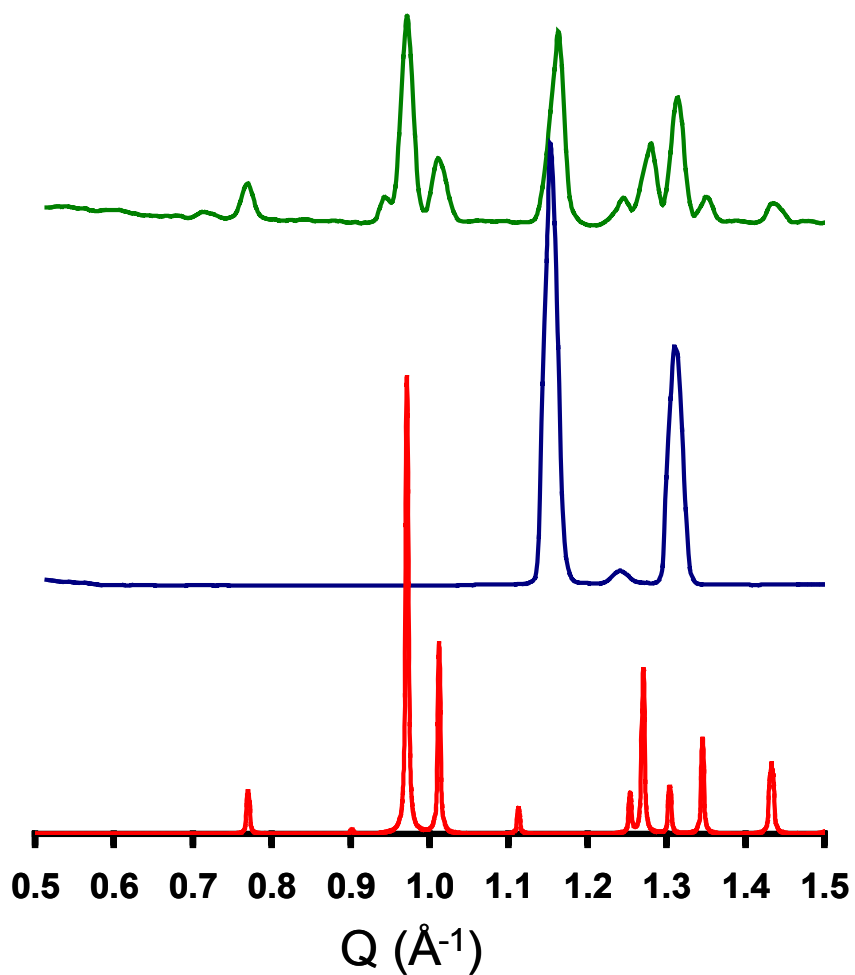


Figure 2.4. Synchrotron x-ray diffractograms of CuAlCl_4 prior (blue) to and after (green) exposure to CO gas giving incomplete reaction to give the $\beta\text{-(CO)CuAlCl}_4$ adduct (calculated pattern shown in red).

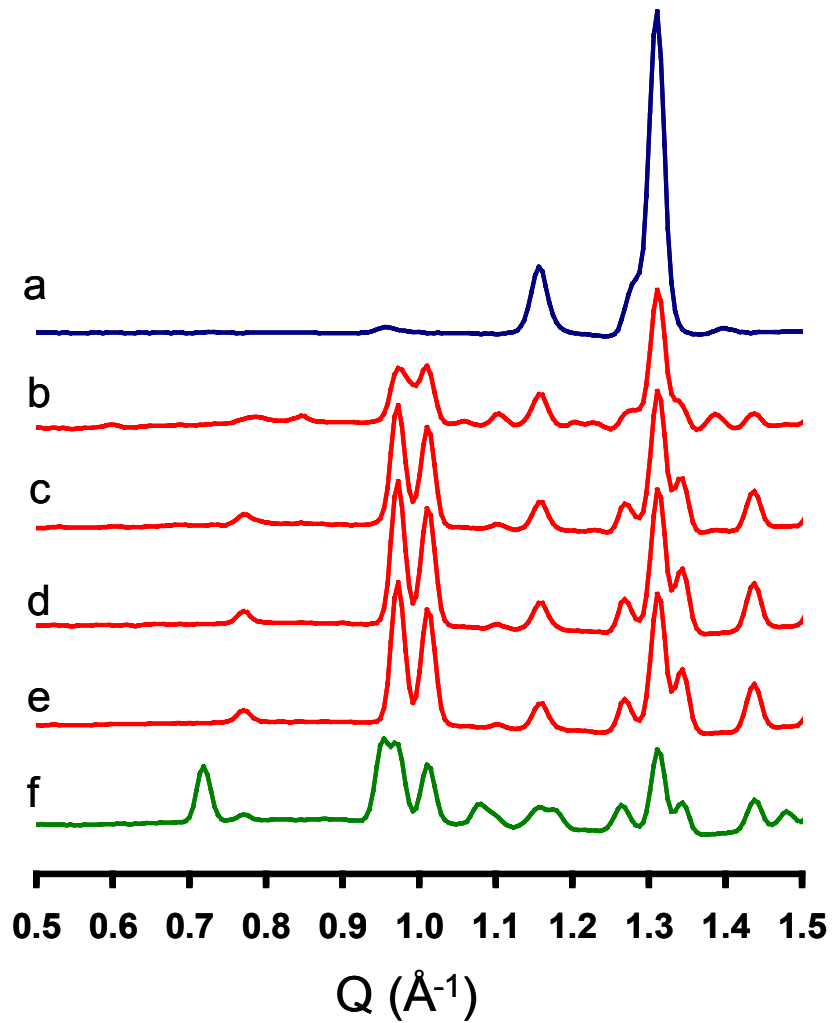


Figure 2.5. Variable Pressure X-ray diffraction of showing the conversion of CuGaCl_4 to β -(CO)CuGaCl₄ (red lines) and (CO)₂CuGaCl₄ (green line) at a) 0 Torr; b&c) 20 psi; d) 30 psi; e) 40 psi; f) 50 psi of CO.

As shown in Figure 2.6, a stepwise desorption of CO from **2-CO_{Al}** is observed as the capillary is heated under vacuum. To date, only the **β-1-CO_{Al}** has been observed upon desorption, whereas both the α - and β -phases have been observed upon sorption. At about 45 °C **β-1-CO_{Al}** begins to melt. At 53 °C the adduct phase is completely melted and begins to release CO resulting in the formation of crystalline CuAlCl₄ starting material. Heating to 100 °C under vacuum resulted in complete desorption of the adduct phase leaving only crystalline α -CuAlCl₄. Desorption of CO from **β-1-CO_{Ga}** also requires heating, though the CO is lost prior to sample melting.

While sorption of CO into CuAlCl₄ results in a unit cell volume expansion of 130% and 190% to form **1-CO** and **2-CO**, respectively, interestingly, these reactions do not cause fragmentation of the reactant crystallites into nano-particulate products, even upon multiple sorption/desorption cycles. Two dimensional diffraction images, Figure 2.7, provide interesting insight as to particle size effects of the sorptive reconstruction reactions. Note: a sample consisting of a fine random powder exhibits smooth diffraction rings, whereas a sample with coarser particle size exhibits spotty rings. Frames a and b of Figure 2.7 demonstrate that coarse grained products are formed upon sorption into CuAlCl₄ and CuGaCl₄ respectively. A significant amorphous ring for the **1-CO_{Al}/2-CO_{Al}** eutectic melt is also clearly observed in Figure 7a. The “grainyness” of these product diffraction patterns is relatively independent of the particle size of the starting reactants (~10 μ m-.1 mm). By contrast, upon desorption and reconstruction of the parent CuMCl₄ phase, a very fine grained powder is formed as shown by the diffraction image of Figure 2.7c, although this pattern give no evidence of Scherrer line-broadening.

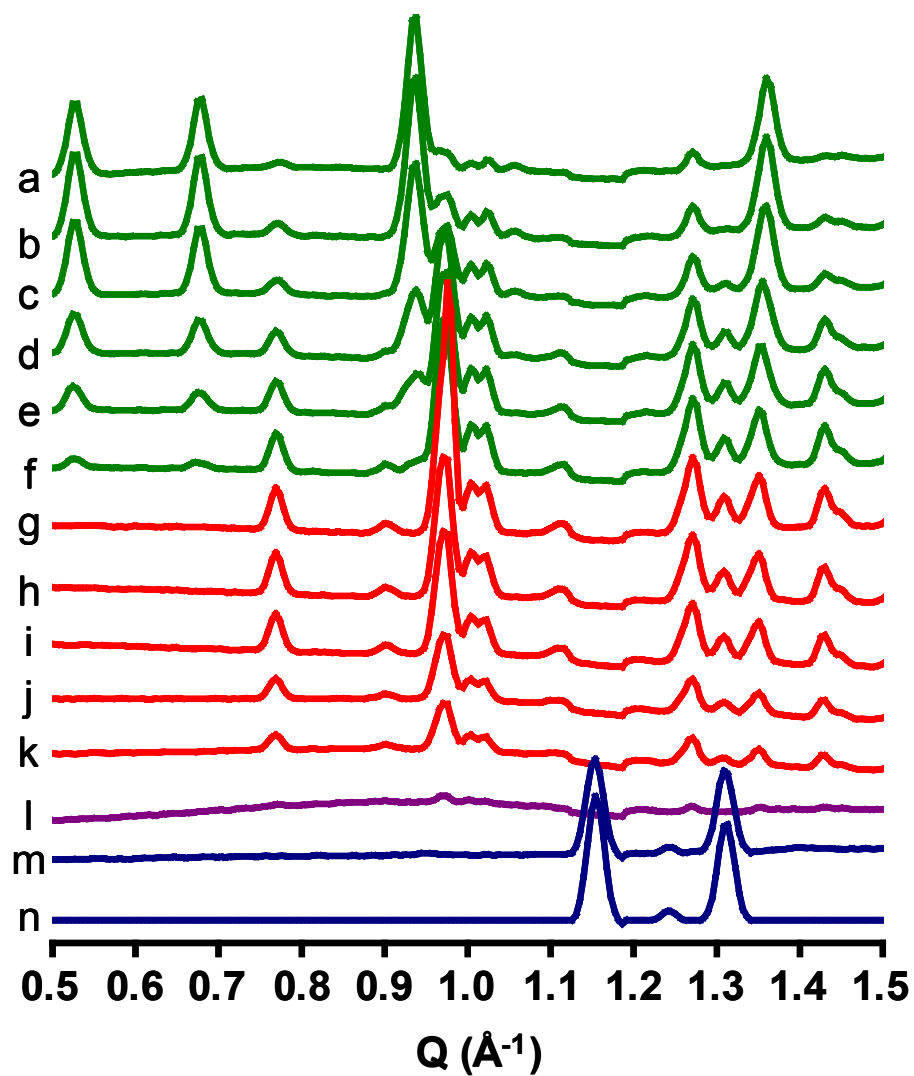


Figure 2.6. Time/temperature-resolved x-ray diffraction for the desorption of CO from $(\text{CO})_2\text{CuAlCl}_4$: [diffractogram, temperature in $^\circ\text{C}$]: (a) $(\text{CO})_2\text{CuAlCl}_4$, (green line) 25; desorption to form $(\text{CO})\text{CuAlCl}_4$, (b) 26; (c) 27; (d) 29; (e) 30; (f) 31; pure $(\text{CO})\text{CuAlCl}_4$ (red lines) (g) 32; (h) 36; (i) 43; (j) 45; (k) 50; (l) melted $(\text{CO})\text{CuAlCl}_4$ (purple line) 53; desorption to give CuAlCl_4 (blue lines) (m) 57; (n) 61.

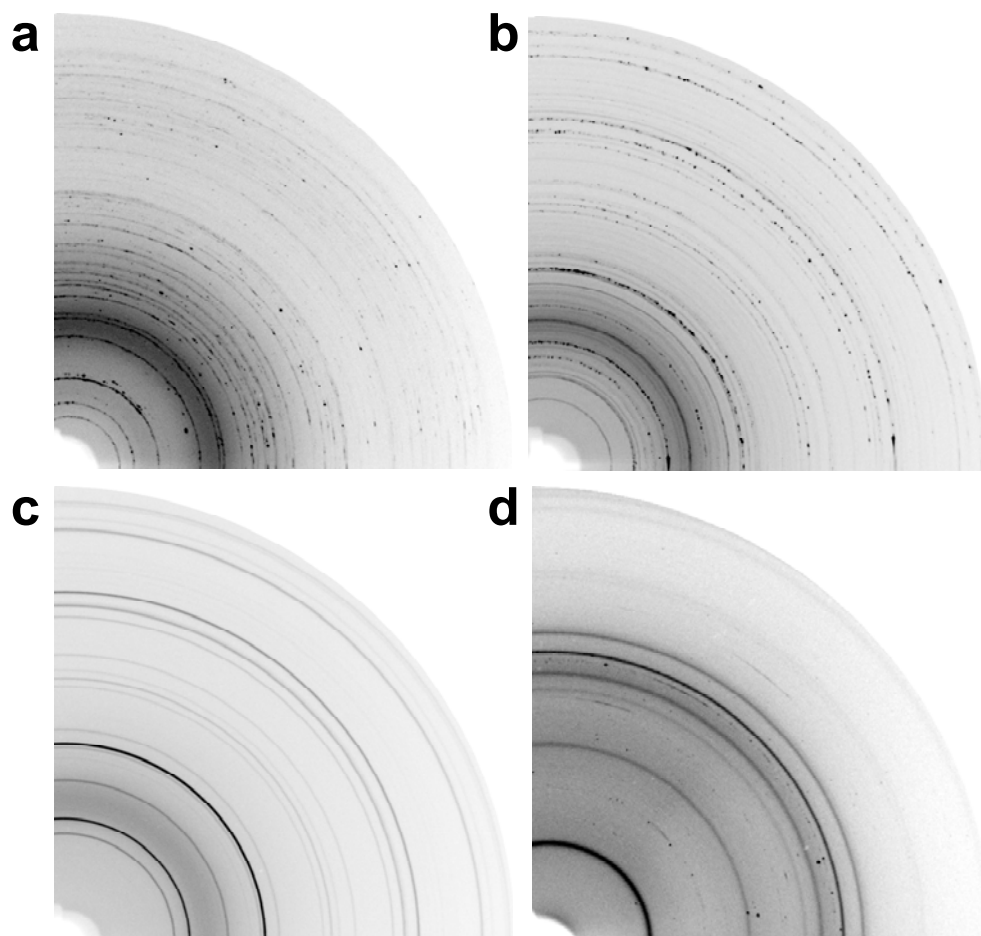


Figure 2.7. Quarter image plates from PRXRD of reaction of $\text{CuMCl}_4 + \text{CO}$. (a) Grainy diffraction pattern of 2-CO_{Al} with amorphous diffraction ring from the eutectic melt. (b) Grainy diffraction pattern with a mixture of 2-CO_{Ga} , $\beta\text{-1-CO}_{\text{Ga}}$ and $\alpha\text{-CuGaCl}_4$. (c) microcrystalline $\alpha\text{-CuGaCl}_4$ from desorption of CO from (b), and (d) Nanocrystalline diffraction pattern of $(\text{CO})\text{CuCl}$.

When capillaries of either CuAlCl_4 or CuGaCl_4 are not sealed well on the gas line a small amount of air/moisture is able to reach the sample. When this occurs the diffraction pattern for the previously characterized $(\text{CO})\text{CuCl}^{13b}$ grows in upon exposure to CO. This capillary reaction proceeds to completion in approximately half an hour at a pressure of 4000 Torr. When $(\text{CO})\text{CuCl}$ is formed no diffraction peaks for either AlCl_3 or GaCl_3 have been observed, however they must be present in some form, possibly as an amorphous decomposition product. Unlike the formation of $\mathbf{1-CO}_{\text{Al}}$ and $\mathbf{1-CO}_{\text{Ga}}$, the 2-D image plates of $(\text{CO})\text{CuCl}$ exhibit fine powder rings (Figure 2.5d), demonstrating that the reaction is extremely destructive to the crystalline lattice. Significant line broadening, about 0.015\AA^{-1} , is observed for the powder pattern(s) of $(\text{CO})\text{CuCl}$ (and CuCl after desorption) consistent with nanocrystalline particle size (~ 40 nm). Running an equivalent pressure resolved diffraction experiment with CuCl ground in an agate mortar and pestle (~ 10 μm particle size) shows no evidence of carbon monoxide sorption. The CuCl-CO adduct loses carbon monoxide when placed under vacuum, and the combination of vacuum and mild heating (approximately 50°C) yields nano-particulate CuCl . Re-exposure of the nano-particulate CuCl to CO results in the reformation of $(\text{CO})\text{CuCl}$, consistent with the previously reported particle size dependence of this reaction.

X-ray Crystal Structures

Single crystals of $\beta\text{-1-CO}_{\text{Al}}$ were grown *in situ* by melt recrystallization in a capillary under a pressure of CO, and its crystal structure was determined by X-ray diffraction. The structure of the isomorphous $\beta\text{-1-CO}_{\text{Ga}}$ was refined by Rietveld analysis of synchrotron X-ray powder diffraction data. It has not yet been possible to determine the structures of the α -

1-CO_{Al} and **2-CO_{Al}** phases, nevertheless, lattice constants for these phases have been determined by powder diffraction methods. A summary of the crystallographic data is given in Table 2.3. Full details of the structure solution are available in the supplementary information.

The structure of **β-1-CO_{Al}** exhibits a ladder-type chain running along **b**, with Cu-Cl-Al rungs that are connected through chloride bridges and related by inversion symmetry, as shown in the ORTEP drawing of Figure 2.8. This results in a strict alternation of corner-shared copper and aluminum tetrahedra. The chains are puckered with the metal cations filling tetrahedral interstices on alternating sides of an anion layer composed of both rung and rail bridging chlorides. Carbonyl ligands are terminally bound to each copper site with a near linear coordination geometry (Cu-C-O = 175.89(3)°) at a distance of Cu-C = 1.857(3)Å. The carbonyl, along with the three chloride bridges (Cu-Cl(1) = 2.4597(7)Å, Cu-Cl(2) = 2.3737(7) Å, and Cu-Cl(4) = 2.3910(7) Å), form a somewhat distorted tetrahedron about the copper, with contracted angles for the chloride face (Cl(1)-Cu-Cl(4) = 95.86(3)°, Cl(1)-Cu-Cl(2) = 103.67(3)° and Cl(2)-Cu-Cl(4) = 101.59(3)°) and expanded angles about the carbonyl ligand (C-Cu-Cl(2) = 124.52(9)°, C-Cu-Cl(1) = 107.33(9)° and C-Cu-Cl(4) = 119.28(10)°). The geometry about the tetrachloroaluminate is a more regular tetrahedron, though the relatively short terminal bond, Al-Cl(3) = 2.090(1)Å with respect to the slightly longer bonds to bridging chlorides (Al-Cl(1) = 2.1443(9)Å, Al-Cl(2) = 2.1673(9)Å and Al-Cl(4) = 2.1508(9)Å) causes a distortion away from the terminal chloride. The average Cl-Al-Cl bond angle to the terminal ligand is 111.7° whereas the average bond angle between the bridging chlorides is 107.2°. Interestingly, the nearly eclipsed CO ligand and terminal chloride exhibit a remarkably short contact, Cl--C = 3.36Å across the ladder rails. This is the shortest

Table 2.3. Summary of Crystal Data for (CO)_xCuMCl₄ Adducts

Formula	β -(CO)CuAlCl ₄	α -(CO)CuAlCl ₄	β -(CO)CuGaCl ₄	(CO) ₂ CuAlCl ₄
	β-1-CO_{Al}	α-1-CO_{Al}	β-1-CO_{Ga}	2-CO_{Al}
	single crystal	powder	powder	Powder
formula weight	260.33	260.33	303.07	288.34
temp, °C	25	15	15	15
space group	<i>P</i> -1 (2)		<i>P</i> -1 (2)	
<i>a</i> (Å)	6.8752(3)	10.67(1)	6.877(1)	9.62(4)
<i>b</i> (Å)	7.0092(3)	7.664(6)	7.015(1)	12.23(6)
<i>c</i> (Å)	8.7362(3)	9.389(5)	8.759(2)	5.152(4)
α (°)	81.798(2)	90	81.00(2)	98.8(2)
β (°)	69.646(2)	93.2(1)	69.45(1)	101.6(5)
γ (°)	85.723(2)	90	85.73(2)	99.1(7)
<i>V</i> (Å ³)	390.53(2)	767(1)	390.75(9)	576(4)
<i>Z</i>	2		2	
R	0.0341		0.0551	
R _w	0.0941		0.0893	

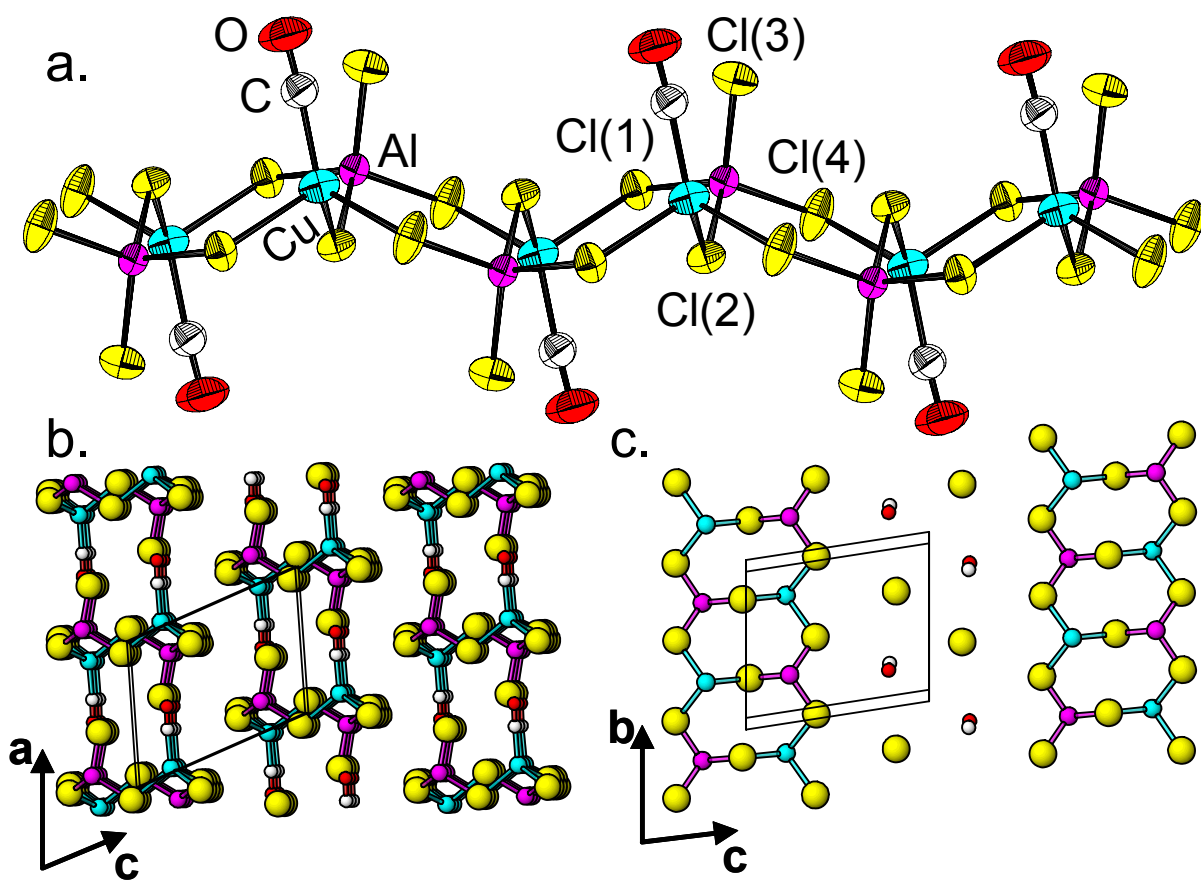


Figure 2.8. (a) ORTEP (50% probability ellipsoid) of a chain of β -1-CO showing the atom labeling scheme. (b) A crystal packing view of the crystal structure looking down the chains (along **b**). (c) A view of the pseudo-close packing of the chlorides and carbonyl ligands in the (201) planes.

inter-ligand contact; the next shortest being Cl(1)-Cl(4) = 3.45Å and Cl(1)-C = 3.50Å. These suggest that there may be some across chain chloride-- π -system interaction, similar to the chloride-- π interaction observed in related structures with ethylene and benzene.^{2,35,36}

These (CO)CuAlCl₄ chains pack extremely efficiently, with the carbonyl and terminal chlorides from chains related by $\pm \mathbf{a}$ interpenetrating a common layer of ligands, seen in Figure 2.6b. In fact the CO and Cl⁻ are so nearly the same size that they form pseudo close packed layers with the CO ligands filling 1/5 of the close-packing sites. Each close packed layer (Figure 2.8c) consists of all the bridging chloride ligands from chains in a crystallographic (201) plane, and the interpenetrating terminal chloride and carbonyl ligands from chains related by $\pm \mathbf{c}$ and $\pm (-\mathbf{a}+\mathbf{c})$. The copper and aluminum cations pair-wise fill 2/10 of the tetrahedral interstices on alternating sides of these close-packed planes. These layers are then stacked in a *hcp* fashion. The interdigitation of the CO and terminal chlorides is reminiscent of the packing of the 2-D sheets of (CO)CuCl.^{13b}

The structure of the α -**1-CO**_{Al} remains elusive, but based on the lattice constants, and relative diffraction intensities, we propose that it exhibits a structure similar to that of the α -**1-et** ethylene adduct, previously reported. The ethylene structure also was not well refined but appears to have orthogonal, as opposed to parallel, ladder chains that run through the crystalline structure. Similarly, the structure of the **2-CO** adduct has not yet been determined, but powder patterns and lattice constants suggest a likely similarity to the structure of the **2-et** ethylene adduct, however with the CO ligands bound end-on as opposed to the edge binding of the ethylene ligands.²

FTIR and UV/Vis Spectroscopy

The reactions of CuMCl_4 ($M = \text{Al}$ and Ga) with CO were monitored by FTIR spectroscopy to determine carbonyl stretching frequency of the adduct phases. Samples were prepared by reaction of CuMCl_4 with carbon monoxide in either fused silica reaction tubes or in a flow cell with KBr windows, with both methods yielding similar spectra in the carbonyl stretching region. The fused silica tubes are most readily interfaced with our gas line, and fortunately have a window in the IR spectrum in the vicinity of the observed CO stretching frequencies; though the window becomes blocked below about 2100 cm^{-1} . Figure 2.9 shows spectra from a representative variable pressure experiment performed in a fused silica tube. At low pressures of CO (200-400 Torr), a single peak is observed in the carbonyl stretching region at 2156 cm^{-1} . As the sample is exposed to increased CO pressure at 750 Torr this peak increases in intensity and new broad features are observed. At this and higher pressures (up to 1500 Torr), some of the sample begins to form a translucent brown liquid phase. An IR spectrum of only the liquid at 950 Torr shows a broad peak around the original peak at 2156 cm^{-1} as well as two new peaks at 2130 cm^{-1} and 2185 cm^{-1} . The two new peaks are consistent with the formation of the dicarbonyl phase $(\text{CO})_2\text{CuAlCl}_4$. Pure $(\text{CO})_2\text{CuAlCl}_4$ could not be obtained with this apparatus. Samples of $(\text{CO})\text{CuGaCl}_4$ also show a peak from 2156 cm^{-1} when exposed to carbon monoxide pressures around one atmosphere, with no additional peaks in the carbonyl stretching region observed on increasing pressure to 1500 Torr.

Following the same CO sorptive reconstruction reaction by diffuse reflectance UV/Vis spectroscopy probes the electronic structure of the adduct phases (Figure 2.10).

Upon initial sorption under about 110 Torr of CO the relatively weak and broad Cu→CO metal-to-ligand charge transfer band becomes visible at about $\lambda_{\max} = 38.4 \times 10^3 \text{ cm}^{-1}$, very near to the Cu3d→Cu 4s transition of the parent CuAlCl₄ phase. By way of reference, a very weak Cu→CO charge transfer band is observed at around $\lambda_{\max} = 37.8 \times 10^3 \text{ cm}^{-1}$ for the sorption of CO into CuCl to form (CO)CuCl. Increasing the CO pressure in this UV/Vis reaction cell results in the observation of increased absorption, particularly of the broad higher energy features at $42.1 \times 10^3 \text{ cm}^{-1}$ and $48.8 \times 10^3 \text{ cm}^{-1}$ which we assign to the **2-CO_{Al}** adduct. On exposure to CO pressures less than one atmosphere, samples of CuGaCl₄ give UV/Vis spectra similar to the aluminate with a Cu→CO metal-to-ligand charge transfer band around $\lambda_{\max} = 38.4 \times 10^3 \text{ cm}^{-1}$ (Figure 2.11).

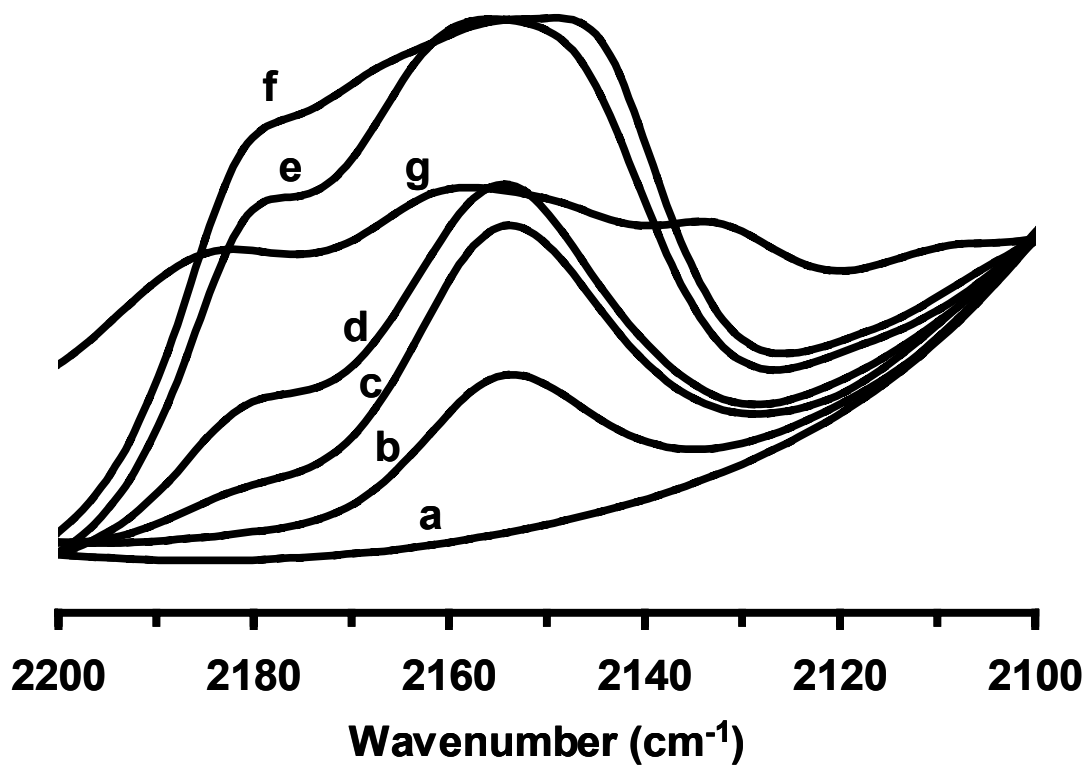


Figure 2.9. FTIR of CO + CuAlCl₄ reaction at (a) 0 Torr; (b) 200 Torr; (c) 375 Torr; (d) 750 Torr; (e) 850 Torr; (f) 950 Torr. Spectrum g is of the eutectic liquid which forms in this system.

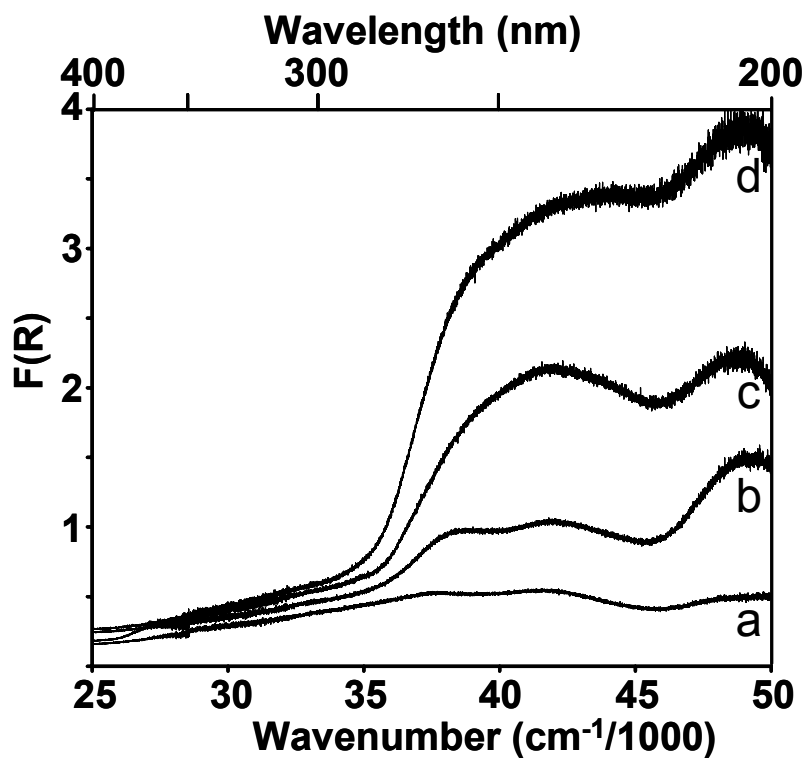


Figure 2.10. Diffuse reflectance UV-Vis of CO + CuAlCl₄ reaction at (a) vacuum; (b) 110 Torr; (c) 820 Torr; and (d) 930 Torr.

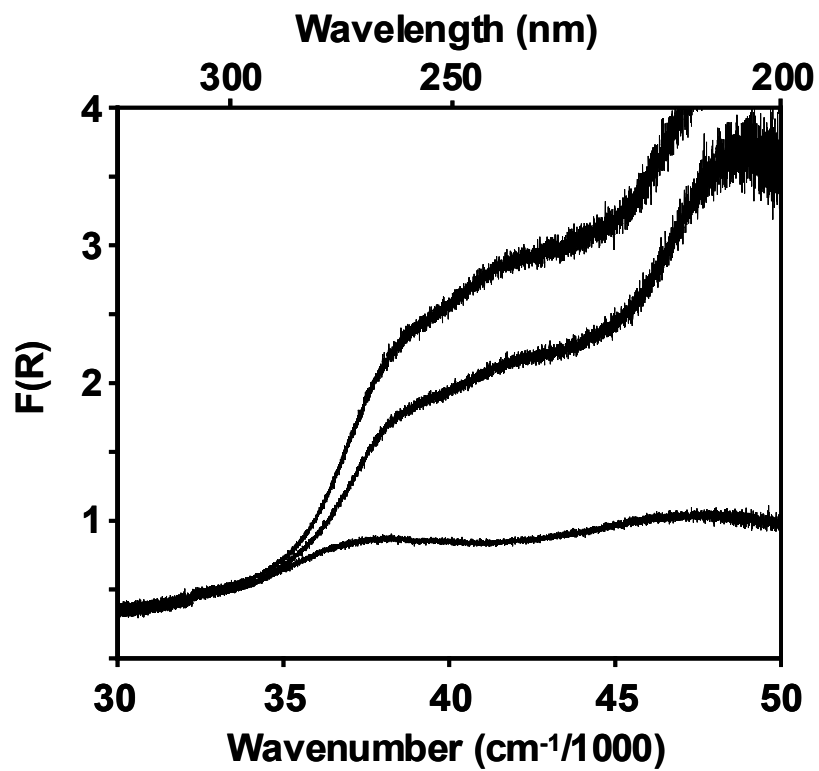
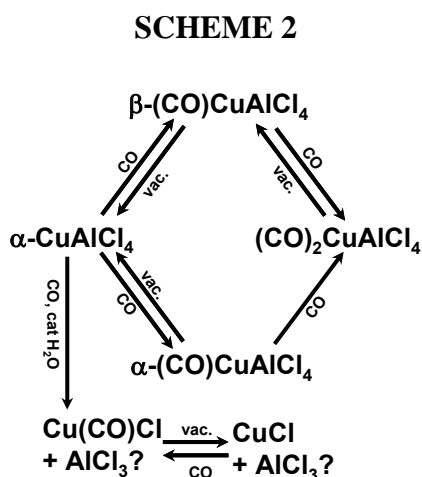


Figure 2.11. Diffuse reflectance UV-vis CO + CuGaCl₄ reaction at a) 0 Torr; b) 200 Torr; and c) 620 Torr of CO.

2.4 Discussion

The sorption isotherms, X-ray structural studies and spectroscopic measurements give indication of a complex pattern of reactivity between CuMCl_4 , $M = \text{Al}$ and Ga , and carbon monoxide, summarized in Scheme 2. Both CuAlCl_4 and CuGaCl_4 reversibly sorb CO gas forming one molar equivalent adduct phases at less than 0.5 atmospheres of CO and a two equivalent phase at higher pressures. A comparative analysis of the crystal structures of the parent $\alpha\text{-CuMCl}_4$ and the products **1-CO** and **2-CO** provide an atomistic picture of the sorptive reconstruction process, with addition of the strong Lewis acids to the copper chloride lattice greatly enhancing the reactivity of copper (I), compared to that of pure CuCl . The pattern of reactivity in these carbon monoxide reactions is quite similar to that previously described for the sorptive reconstruction of CuAlCl_4 upon reaction with ethylene, though notable contrasts in the reactivity are observed as a function of the common ion Lewis acid (AlCl_3 or GaCl_3).



Mechanistic Considerations

Though not a microporous material CuMCl_4 ($M = \text{Al}$ and Ga) exhibits a remarkable sorption capacity of up to 200 cc of CO or ethylene per g of sorbate. This reactivity proceeds via a reaction mechanism that we have described as sorptive reconstruction. Two one-equivalent adduct phases, described as α and β , respectively, are observed by powder X-ray diffraction. The sorption isotherm measurements shown in Figure 1 also give indication of reaction via two distinct pathways, consistent with the formation of these two adducts. It has not yet been possible to unequivocally determine which reaction pathway leads to which of the two **1-CO** products. However, because only the **β -1-CO_{Ga}** adduct has been observed for reaction of CuGaCl_4 with CO, and reactions with the gallate only exhibit the step-wise β -path isotherms, we suggest that the step-wise sorption isotherm for alluminate material also proceeds through the formation of **β -1-CO_{Al}**. Furthermore, the pressure resolved diffraction measurements that show the formation of **α -1-CO_{Al}** (Figure 2.3) also exhibit significant and concomitant formation of **2-CO_{Al}**, whereas those showing the formation of **β -1-CO_{Al}** exhibit only trace formation of **2-CO_{Al}** (see figure 2.4). We therefore suggest that this reaction path, described as the α -path, corresponds to the continuous sorption isotherm, shown as red squares in Figure 2.1.

The single crystal structure of the β -phase has been determined and found to be nearly iso-structural to that of β -(et) CuAlCl_4 , **β -1-et**. However, the slightly smaller size and end-on binding of CO, as compared to the edge binding of ethylene, results in a more efficient packing of the carbonyl ladder chains. Both ethylene and CO adduct structures can be described based on a close packing of the chlorides and ligands. However in **β -1-et**, 1/6 of the close-packing sites are vacant, whereas all sites are filled with either CO or Cl in **β -1-**

CO. This results in only a 130% expansion of the unit cell volume upon formation of **β -1-CO** as opposed to the 150% expansion observed for the formation of **β -1-et**.

Upon careful examination of the crystalline structures of the parent α -CuMCl₄ and the product **β -1-CO** it is apparent that van der Waals channels through the parent crystalline phase³⁷ direct the reactivity toward CO. The van der Waals channels between close packed halide layers, highlighted in blue in Figure 2.12a, though too small for the ligand to pass through, provide the entry point for ligand attack. We have colloquially referred to this type of excision reaction as a “rat snake” mechanism, whereby the jaw of the snake is disengaged in order to accommodate swallowing an egg that is much larger than its mouth. The structure shown in Figure 2.9b is simply a chain running along the 112 vector that has been excised from α -CuAlCl₄. This chain consists of two CuAlCl₄ units that form a four-metal ring analogous to the four-rings in the one equivalent adduct chain, and two units that exhibit chloride bridges along the ladder rails but lack the across-chain halide bridges to form the ladder rungs. Excision of such a chain is possible with nucleophilic attack by CO at the Cu(I) center followed by an inversion of configuration that breaks select network Cu-Cl bonding. Rotation of the tetrachloroaluminate building blocks, as implied by the dotted arrows in Figure 2.12b, allows terminal aluminum bound chlorides, released when CO is coordinated to the coppers of a neighboring chain, to form bridges to the opposite rail of the forming ladder chain. Preliminary kinetic data for ethylene sorption, assumed to be analogous to the CO sorption, suggest that the rate of this reaction increases with increasing reactive gas pressure, consistent with an associative mechanism whereby ligand coordination is the rate limiting step; as opposed to a dissociative mechanism that would require initial Cu-Cl cleavage (defect formation) to be rate limiting, followed by ligand coordination.

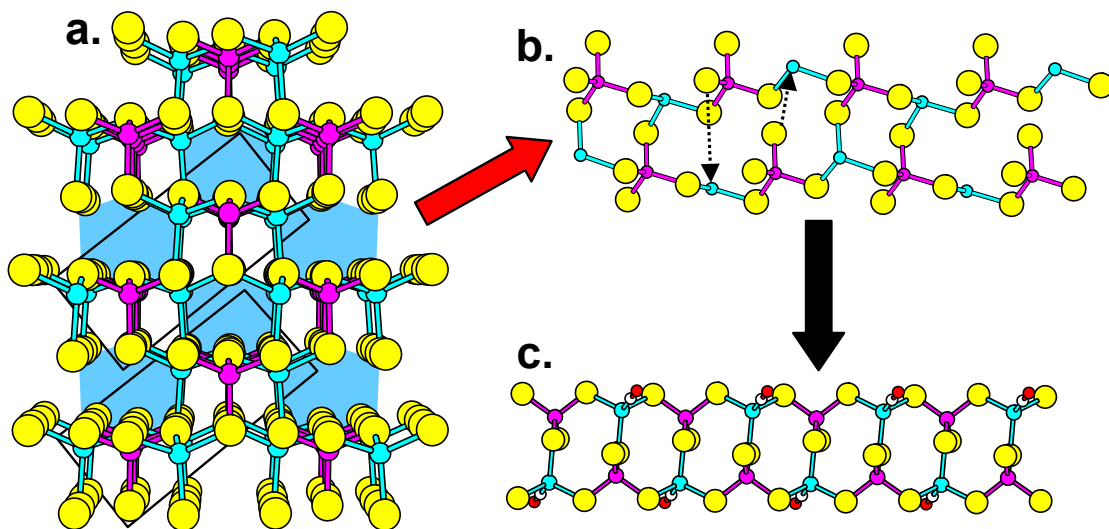


Figure 2.12. Pathway for the sorptive reconstruction of α - CuAlCl_4 to chains of $(\text{CO})\text{CuAlCl}_4$. (a) View of α - CuAlCl_4 looking down the 112 vector with shaded blue regions highlighting the van der Waals channels. (b) A chain excised from α - CuAlCl_4 (outlined in a box in a.) running parallel to the 112 vector. (c) A single chain of β - $(\text{CO})\text{CuAlCl}_4$.

The structure of the α -**1-CO_{Al}** phase is not yet clearly defined, though as noted above, it appears to be similar to the α -**1-et**, phase previously reported for ethylene reactivity.

Whereas the adduct chains run parallel in the β -phase, they run in orthogonal directions in the α -phase. As also proposed for the ethylene reactivity, we suspect that nucleation at the tetragonal-van der Waals channels of α -CuAlCl₄ provide the reaction pathway that leads to the α -**1-CO_{Al}** product.

Exposure of either **1-CO** adduct phase to a higher pressure (higher concentration) of carbon monoxide results in the formation of the two equivalent adduct **2-CO**. As articulated in our prior description of the ethylene induced sorptive reconstruction, this is accomplished by nucleophilic attack of additional CO at the copper centers. Inversion of configuration at the metal center upon ligand attack results in an “unzipping” of chloride bridges of the ladder rungs to yield parallel chains of **2-CO**.

The reactivity of CuMCl₄ toward CO when trace amounts of water are present, which result in the formation of (CO)CuCl, is in notable contrast to the afore described sorptive reconstruction mechanism. Instead of allowing the reaction to propagate down the van der Waals channels of the parent phase, the trace amount of water apparently causes a surface disproportionation of CuMCl₄ to nanoparticulate CuCl and some MCl₃ decomposition product. The near molecular dimension of CuCl provided by the decomposition of this bulk crystalline system affords reactivity with CO closer to that observed for reaction of CuCl dissolved in aqueous acid or polar organic solvents than is observed for bulk crystalline CuCl.^{12,13} Apparently the formation of (CO)CuCl does not provide a sufficient driving force to overcome the lattice energy of bulk CuCl, thus precluding reactivity until CO pressures of

greater than 100 atm are achieved. By contrast, molecular or nanoparticulate CuCl exhibits an equilibrium binding pressure of about 0.5 atm.¹³

Lewis Acid Impact on Ligand Binding

Evaluation of the Cu-CO bonding demonstrates that in addition to the enhanced reactivity, incorporation of a strong Lewis acid into the copper chloride lattice exhibits a significant influence on the bonding of ligands. Whereas previous work clearly demonstrated particle size effects for the CO sorption into CuCl, indicating a significant kinetic barrier to small molecule sorption, the addition of Lewis acids to the copper chloride lattice alters the thermodynamics and kinetics of ligand binding such that the reactivity is relatively particle size independent.¹⁶⁻¹⁸ Crystal structure analysis does not exhibit extensive variation of M-C and C-O distances as a function bonding, however, it is worthwhile to note that the C-O distance observed for β -**1-CO_{Al}**, 1.102(4)Å is slightly shorter than that observed for (CO)CuCl, 1.112(18).^{13b} Their respective Cu-C distances are essentially equivalent (1.856(16) Å in (CO)CuCl and 1.857(3) Å in (CO)CuAlCl₄). This is consistent with the suggestion that the strong Lewis acid, AlCl₃, decreases any ability of the Cu(I) to back-bond with the carbonyl ligand. The non-classical nature of the Cu-CO bonding in these compounds is more clearly demonstrated by the carbonyl stretching frequency $\nu_{\text{CO}} = 2156 \text{ cm}^{-1}$, which is 13 cm^{-1} higher in energy than that of free carbon monoxide ($\nu_{\text{CO}} = 2143 \text{ cm}^{-1}$). By comparison to other materials described in Table 1 above, it is clear that **1-CO_{Al}** and **1-CO_{Ga}** exhibit more non-classical bonding than the weakly classical (CO)CuCl, $\nu_{\text{CO}} = 2120 \text{ cm}^{-1}$,^{13b} but are less non-classical than (CO)Cu[AsF₆], $\nu_{\text{CO}} = 2178 \text{ cm}^{-1}$. The matrix isolated (CO)Cu⁺ cation, with $\nu_{\text{CO}} = 2234 \text{ cm}^{-1}$ represents the non-classical limit for CO

binding to Cu(I). The bands at 2185 cm^{-1} and 2130 cm^{-1} observed at higher CO pressures, which we assign to the dicarbonyl adduct, **2-CO_{Al}**, are consistent with the symmetric and asymmetric stretches of a pseudo trigonal-planar (CO)₂CuCl unit (see structure of (et)₂CuAlCl₄ in ref 2) rather than the linear dicarbonyl cation structure proposed for (CO)₂Cu[AsF₆].¹⁷

As described in eq. 2, a conjugate anion of a strong Lewis acid is a poor ligand to the copper center. By weakening the metal ligand bonds, i.e. from Cu-Cl to Cu-ClAlCl₃, the π -donor and σ -acceptor orbitals of Cu(I) are significantly lowered in energy (Scheme 1), thus favoring a non-classical mode of carbonyl binding. Though not typically reported, direct evidence of this orbital stabilization can be observed by UV/vis diffuse reflectance measurements of the Cu $d^{10} \rightarrow \text{CO } \pi^*$ electronic transitions. A very weak feature is observed in the UV/Vis spectrum of (CO)CuCl with $\lambda_{\text{max}} = 37.8 \times 10^3\text{ cm}^{-1}$, whereas **1-CO_{Al}** and **1-CO_{Ga}** each exhibit a broad feature blue shifted to $\lambda_{\text{max}} = 38.4 \times 10^3\text{ cm}^{-1}$. The energy of the MLCT band does not significantly change with the sorption of more than one equivalent of CO. However the increase in the intensity of higher energy bands at $42.1 \times 10^3\text{ cm}^{-1}$ and $48.8 \times 10^3\text{ cm}^{-1}$ with higher CO pressure suggest that, like the ethylene adducts, there is a significant change in coordination about copper from pseudo tetrahedral in the **1-CO_{Al}** adduct to a pseudo trigonal-planar coordination in **2-CO_{Al}**.

Both IR and UV/Vis spectra paint a similar picture of weakened binding of the lattice chloride ligands to copper when strong Lewis acids are incorporated. Interestingly, the ν_{CO} of both copper-aluminum and -gallium complexes is essentially equivalent to that observed for the matrix isolated linear (CO)CuCl molecules, suggesting that the three Cu-Cl bonds in (CO)CuAlCl₄ (average $d_{\text{Cu-Cl}} = 2.41\text{ \AA}$) provide equivalent bonding to Cu as the single Cl

ligand in the matrix isolated molecule (CO)CuCl (Cu-Cl = 2.10Å). (By way of reference the average Cu-Cl bond distance for the four contacts in CuCl is 2.35Å³⁸ and 2.36Å for the three Cu-Cl bonds in crystalline (CO)CuCl^{13b}).

The variation in the copper-carbonyl bonding, described above, directly impacts the reactivity, as well as the sorption capacity of the systems. While the sorption reactions may exhibit a significant kinetic barrier (largely seen as a particle size effects) due to the deconstruction of the parent crystalline lattice, the desorption isotherms are most useful for determining the strength of the copper carbonyl interactions. Previously it was shown that for the weakly classical carbonyl complex (CO)CuCl, the room temperature equilibrium binding pressure is 440 Torr.^{13a,14} While this value is reasonably sensitive to temperature, it is largely independent of the path by which it was formed (bulk, thin film, nano-particle or solution reaction), and there is no evidence for sorption of greater than one equivalent of CO. By contrast, the non-classical carbonyl complexes discussed here exhibit a significantly lower equilibrium binding pressure of around 350 Torr. Both these Cu/Al and Cu/Ga materials are shown to bind a second equivalent of CO under elevated pressure, with desorption equilibrium binding pressures of between 700 and 500 Torr. Binding of CO to these adducts appears to be slightly more facile for the Cu/Al material than the Cu/Ga material, nevertheless, the latter may have a slightly lower equilibrium binding pressure. That sorption of CO into the Cu/Al system is somewhat more facile than sorption into the Cu/Ga system is attributed to fact that the melting point of the Cu/Al-CO adducts is very close to room temperature (with the eutectic below room temperature), whereas the CuGaCl₄ lattice is more rigid and the Cu/Ga-CO adducts decompose before they melt. The slight, but opposite trend in the equilibrium binding pressures may be a result of differential Cu-CO

bonding as a result of GaCl₃ being a slightly weaker Lewis acid. Furthermore, based on the slope of the isotherms, it is likely that a third equivalent of CO may be bound at pressures higher than are accessible with our gas line. These results are consistent with the sorption of CO into the even more non-classical system CuAsF₆ for which a one-equivalent adduct is observed to form with CO pressure of 3-10 Torr, a low melting two-equivalent adduct forms at pressures between 10-100 Torr, and a solid three-equivalent adduct forms at pressures between 100 and 500 Torr.¹⁷

It is thus clear that the bonding characteristics which are the basis of non-classical Cu-CO bonding also can enhance the reactivity and sorption capacity of these copper(I)-based sorbates. These results further support the suggestion that it is σ -type bonding that dominates the Cu-CO binding. In this regard, it is informative to compare the reactivity of both CO and ethylene with these copper-based materials. Whereas CO is only a moderate σ -donor but an excellent π -acceptor, ethylene is a good σ -donor ligand but only a modest π -acceptor. As a result, CuCl, which allows weak π -back-bonding (it forms a weakly classical carbonyl complex), forms a stable carbonyl complex with a room temperature dissociation pressure of 440 Torr, but the dissociation pressure from (et)CuCl is about 8 atm. By contrast, the non-classical CuAlCl₄, for which predominantly σ -bonding is observed, forms strong ethylene adducts with dissociation pressures of < 10 Torr from **1-et_{Al}** and ~70 Torr from **2-et_{Al}**, and relatively weaker carbonyl adducts with dissociation pressures of ~360 Torr from **1-CO_{Al}** and ~700 Torr from **2-CO_{Al}**. The slightly weaker Lewis acid GaCl₃ (in CuGaCl₄) results in adducts for which the ethylene vs. carbonyl binding is nearly equivalent, but with a slight preference for CO. Continuation of this trend suggests that the even more non-classical CuAsF₆ should exhibit an even greater affinity for ethylene binding.

2.5 Conclusions

The reversible binding of CO by CuAlCl_4 and CuGaCl_4 has been characterized by X-ray single crystal and powder diffraction, IR and UV/Vis spectroscopy, gravimetric and volumetric adsorption studies. One and two equivalent CO-adduct phases that form by topotactic reconstruction of the CuMCl_4 lattice have been identified for each system. Incorporating the Lewis acids AlCl_3 and GaCl_3 into the copper chloride framework facilitates both the kinetics of CO sorption and also improves the Cu(I)-CO bond strength relative to $(\text{CO})\text{CuCl}$. These systems are understood from the perspective of nonclassical metal carbonyl bonding that exhibits primarily σ -bonding interactions. The nonclassical bonding, and corresponding enhanced ligand binding, is the result of the Lewis acids weakening Cu-Cl bonding upon formation of their weakly coordinating conjugate base anions (AlCl_4^- and GaCl_4^-). These weakly coordinating anions lower the energy of the copper's frontier orbitals making it a more effective σ -acceptor and a very weak π -back-bonder. As demonstrated by comparative carbonyl vs. ethylene binding, copper(I)'s propensity to adsorb gases with different σ -donor/ π -acceptor characteristics can be tuned based on which Lewis acids are incorporated into its framework. Stronger Lewis acids, favor adduct formation with ligands that are better σ -donors (ethylene), while a better π -acid ligands (CO) will bond preferentially in a more electron donating ligand environment.

2.6 Experimental

General Methods and Procedures

All manipulations were performed under an inert N₂ atmosphere in a dry box, or using Schlenk or vacuum lines. The chloride materials CuCl³⁹ and α -CuMCl₄ (M = Al, Ga) were prepared according to literature methods. Carbon monoxide gas of natural isotopic abundance, used in all experiments, was purchased from either National Welders or Aldrich.

Sorption Isotherms

Gravimetric measurements were carried out in a tared Pyrex Schlenk tube loaded with α -CuAlCl₄ and pressurized with 1500 Torr N₂. After determining the total mass, the tube was evacuated and pressurized with CO at 1500 Torr and allowed to equilibrate for up to 8-12 h. Because the molecular weights of CO and N₂ are equivalent (28 g/mol) any difference in mass upon substituting CO for N₂ is due to the amount of gas sorbed by the CuAlCl₄. In a typical experiment, 0.5 g of CuAlCl₄ exhibited an increase in mass of about 0.06 g upon exposure to 1500 Torr of CO.

All barometric studies were performed on a calibrated gas/vacuum line described previously. To measure adsorption isotherms, approximately 40 mg of CuAlCl₄ powder was placed in a Pyrex sample cup with a 2-cm² base. The sample was covered with a layer of dry glass wool and sealed in a stainless steel container with a volume of 26 mL. The sample container was then attached to the gas line using Swagelok connectors and nitrogen gas was purged from the container under dynamic vacuum. The dead volume of the sample holder was measured by an N₂ isotherm prior to the experiment with reactive gas. Samples were exposed to carbon monoxide by an automated process as follows. The sample chamber was

isolated from the calibrated line volume and a predetermined gas pressure was introduced into the line. The initial dosing pressure was either 50, 100, 200 or 600 Torr depending on the specific experiment. The valve to the sample chamber was then opened and the gas was allowed to expand into the sample volume. The line pressure was recorded once per minute for 30 min to 1 h. to ensure the system came to equilibrium. The drop in pressure due to volume expansion was determined by the Boyle's law relationship ($P_1V_1/T = P_2V_2/T$). Any further decrease in pressure is attributed to gas sorption. With equilibration intervals of one half or one hour, this process was cycled increasing the pressure of CO in incremental steps with the step size equivalent to the initial dosing pressure, until the limit of the pressure transducer was reached at 5000 Torr. Desorption experiments were carried out manually using the same gas line. The sample chamber was isolated at a given pressure, then the pressure in the calibrated line was decreased to some lower value by exposure to vacuum. The valve to the sample chamber was then opened and the gas was allowed to expand into the calibrated line volume. After equilibration, the pressure in excess of the Boyle's law expansion was attributed to desorption from the sample. This process was repeated until pressures below 10 Torr were achieved.

X-ray structure determination of (CO)CuAlCl₄

Single crystals of (CO)CuAlCl₄ were grown *in situ* in a capillary sealed under CO pressure. Approximately 0.050 mg of α -CuAlCl₄ powder was placed into a fused silica tube affixed with a Teflon stopcock on one end and a hand-drawn capillary (~2 mm in diameter) on the other. Using a gas manifold, this reaction tube was evacuated and subsequently filled with approximately 500 Torr of CO and allowed to equilibrate for 30 minutes. The stopcock

of the tube was then closed and the base end of the tube was suspended vertically inside a tube furnace and heated to 50°C for several hours. At this temperature the adduct melted and flowed into the capillary portion of the tube. Once the melted adduct reached the bottom, the capillary portion of the tube was flame sealed. The capillary was again heated in a furnace at 50°C for 3 hours. The furnace was cooled 0.05°C/min to 34°C and remained at that temperature for 6 hours. Repeating this heat-cool cycle several times produced large crystals suitable for single crystal x-ray studies. One such capillary was mounted on a goniometer such that a large single crystal (2 mm x 2 mm x 10 mm) could be centered in the X-ray beam. Data were collected at room temperature using a Bruker-Nonius X8 Apex2 diffractometer with Mo K α radiation. The cell lattice constants were determined using 5650 reflections with $2.50^\circ < 2\theta < 29.29^\circ$. Reflections were collected from the entire Ewald sphere with 2369 independent reflections measured with a mixture of phi and omega scans from $2.51^\circ < \theta < 30.50^\circ$. All of the atom positions were found using direct methods with the SHELXTL program.⁴⁰ A full matrix least squares calculation on 1878 unique reflections [$I > 2.0\sigma(I)$] were used in the final refinement using the SHELXTL programs. The final R factors obtained were $R = 0.0341$ and $R_w = 0.0941$.

Synchrotron Powder X-ray Diffraction

Powder x-ray diffraction experiments were performed at the National Synchrotron Light Source at Brookhaven National Laboratory on beam line X7B with a wavelength of approximately 1Å in a Debye-Scherrer collection geometry using a MAR345 Image Plate Detector System. The wavelength, sample-to-detector distance, tilting angle of the IP and zero shift position of the IP for the data collected were calibrated to a LaB₆ standard using

the ‘fit2d’ software package to analyze the full Debye-Scherrer rings of the MAR data.⁴¹ Powdered samples of CuCl, CuGaCl₄ or CuAlCl₄ were mixed with dried ground fused silica and placed in a 0.7 mm fused silica capillary affixed to a gas line with Swagelok fittings and aligned on a goniometer head.⁴² The carbon monoxide pressure was metered with an electronically controlled gas manifold. The experimental temperature was maintained at approximately 15 °C with an Oxford cryostream. The background from a CuAlCl₄/SiO₂ sample was subtracted to remove amorphous diffraction intensity due to the capillary and SiO₂.

The structure of **β-1-CO_{Ga}** was characterized using the GSAS suite of programs⁴³ and the PXRD data ($\lambda = 0.92137 \text{ \AA}$, $5^\circ < 2\theta < 35^\circ$) from the pressure resolved experiment, a portion of which is shown in supplemental figure S2. This pattern contains a mixture of α -CuGaCl₄ and **β-1-CO_{Ga}**. The pattern was fit to the known crystal structure of α -CuGaCl₄ and a model structure derived from the single crystal refinement of **β-1-CO_{Al}**. A spherical harmonic (ODF) correction was required to account for the observed preferred orientation for this *in situ* grown sample. It was not possible to achieve successful refinement of atom positions of the CO adduct phase. Full profile refinement of the phase ratio and lattice constant variables (with all atomic parameters fixed to those of the single crystal values for **β-1-CO_{Al}**) yielded a refinement of $R = 0.0551$ and $R_w = 0.0893$.

FTIR Spectroscopy

Samples for FTIR measurements were prepared with approximately 50 mg of CuMCl₄ in either fused silica reaction tubes or sealed between the two KBr salt plates of an IR flow cell. For the variable pressure experiments the fused silica tubes were evacuated to

remove the N₂ after loading with sample. Then the CuMCl₄ was melted in a tube furnace (at 275 °C) and subsequently rapidly cooled to room temperature while rotating the tube, such that material coated the upper part of the fused silica tube. This allowed for gravity separation of the solid and liquid phases formed in the CuAlCl₄ + CO reaction. Carbon monoxide gas was introduced into the tubes using a gas/vacuum manifold. Pressures were measured using an MKS PDR-D-1 pressure transducer. All spectra were collected *in situ* using a Mattson Genesis II spectrophotometer.

Diffuse Reflectance UV/Vis

Diffuse reflectance measurements were carried out on a Cary 3e UV-vis spectrophotometer equipped with an integrating sphere. Spectra were measured with respect to a pressed poly(tetrafluoroethylene) powder standard. Reflectance intensities were collected as the remission function, $F(R_\infty) = (1 - R_\infty)^2/2R_\infty$ (based on Kubelka-Munk theory of diffuse reflectance)⁴⁴ versus wavenumber. For measurement of the reflectance on gas sorption/desorption, samples were prepared by grinding together approximately 0.02 g of CuMCl₄ or CuCl with 1.0 g of ground fused silica particles (300-800 μm) with a mortar and pestle. Powdered samples were then placed in a 1 x 10 mm cuvette that was connected to a gas/vacuum manifold.

Acknowledgements

Dr. Jonathan C. Hanson is acknowledged for his support at NSLS Beamline X7B, and Dr. Paul D. Boyle for his assistance in collecting the single crystal data. This work was supported by the NSF via the contract DMR-0305086. The research carried out at beam line

X7b at BNL-NSLS was supported by contract DE-AC02-98CH10086 with the US DOE office of basic energy sciences division of chemical sciences. The NSLS is supported by the Divisions of Materials and Chemical Sciences of DOE.

Supporting Information

Single crystal X-ray crystallographic data for β -1-CO_{Al}, and powder data for β -1-CO_{Ga} are available in .cif format. This material is available free of charge via the Internet at <http://pubs.acs.org>.

2.7 References

- (1) "Separation Technologies for the Industries of the Future" National Research Council (US), **1998**, National Academy Press: Washington D.C.
- (2) Sullivan, R. M.; Liu, H.; Smith, S.; Hanson, J. C.; Osterhout, D.; Ciraolo, M.; Grey, C. P.; Martin, J. D. *J. Am. Chem. Soc.* **2003**, *125*, 11065-11079.
- (3) (a) Turner, R. W. and Amma, E. L. *J. Am. Chem. Soc.* **1966**, *88*, 1877-82. (b) Dattelbaum, A. M.; Martin, J. D. *Inorg. Chem.* **1999**, *38*, 6200-6205. (c) Dattelbaum, A. M.; Martin, J. D. *Polyhedron*, **2006**, *25*, 349-359.
- (4) Bigorgne, M. *J. Organomet. Chem.* **1978**, *160*, 345-356.
- (5) Hadjiivanov, K.; Kantcheva, M. M.; Klissurski, D. G. *J. Chem. Soc. Faraday Trans.* **1996**, *92*, 4595-4600.
- (6) Szanyi, J.; Paffett, M. T. *J. Catal.* **1996**, *164*, 232-245.
- (7) Bruce, M. I., *J. Organomet. Chem.*, **1972**, *44*, 209-226.
- (8) (a) Lee, S. *Methanol Synthesis Technology*; CRC Press: Boca Raton, FL, 1990; pp 1-22. (b) Cheng, W. H.; Kung, H. H. *Methanol Production and Use*; Cheng, W. H., Kung, H. H., Eds.; Marcel Dekker: New York, 1994; pp 1-22.
- (9) (a) Haase, D. J., Walker, D. G. *Chem. Eng. Prog.* **1974**, *70*, 74-77. (b) Long, R. B.; Caruso, F. A.; Walker, D.G. "Monomere Bimetallsalze sowie Verfahren zu ihrer Herstellung and Verbindung." German Patent DE 1,944,405, **1968**. (c) Turnbo, R. G. Process for the Preparation of Bimetallic Salt Complexes *U.S. Patent* 3,857,869; **1974**. (d) Sudduth, J. R.;

- Keyworth, D. A. "Process for the Purification of Gas Streams" *U.S. Patent* 3,960,910, **1975**.
- (e) Walker, D. G. *Chemical Technology*, **1975**, 5, 308-311.
- (10) Gilliland, E. R.; Seebold, J. E.; FitzHugh, J. R.; Morgan, P. S. *J. Am. Chem. Soc.*, **1939**, 61, 1960-1962.
- (11) (a) Leblanc, F. C., *R. Acad. Sci. Paris*, **1850**, 30, 483. (b) Berethelot, M., *Ann. Chim. Phys.*, **1856**, 346, 364.
- (12) Wagner, O. H. *Anorg. Allg. Chem.* **1931**, 196, 364-373.
- (13) (a) Backen, W.; Vestin, R. *Acta. Chem. Scand.*, **1979**, A33, 85-91. (b) Hakansson, M.; Jagner, S. *Inorg. Chem.* **1990**, 29, 5241-5244. (c) Pasquali, M.; Florinani, C.; Gaetani-Manfredotti, A. A. *Inorg. Chem.* **1981**, 20, 3382-3388.
- (14) Peng, X. D.; Golden, T. C.; Pearlstein, R. M.; Pierantozzi, R. *Langmuir*, **1995**, 11, 534-537.
- (15) Huang, H. Y.; Padin, J.; Yang, R. T. *Ind. Eng. Chem. Res.* **1999**, 38, 2720-2725.
- (16) Strauss, S. H. *J. Chem. Soc., Dalton Trans.* **2000**, 1-6.
- (17) Rack, J. J.; Webb, J. D.; Strauss, S. H. *Inorg. Chem.* **1996**, 35, 277-278.
- (18) Willner, H., and Aubke, F. *Angew. Chem. Int. Ed.* **1997**, 36, 2402-2425.
- (19) Brand, H. V.; Redondo, A., and Hay, P. J. *J. Phys. Chem. B.* **1997**, 101, 7691-7701.
- (20) Burdett, J. K., and Eisenstein, O. *Inorg. Chem.* **1992**, 31, 1758-1762.

- (21) Rodríguez, F. I.; Esch, J. J.; Hall, A. E.; Binder, B. M.; Schaller, G. E.; Bleeker, A. B. *Science*, **1999**, 283, 996-998.
- (22) Scarano, D.; Galletto, P.; Lamberti, C.; De Franceschi, R.; Zecchina, A. *Surf. Sci.* **1997**, 387, 236-242.
- (23) (a) Plitt, H. S.; Bär M. R.; Ahlrichs, R.; Schnöckel H. *Inorg. Chem.* **1992**, 31, 463-465.
(b) Shao, L.; Zhang, L.; Zhou, M.; and Qin, Q. *Organomet.* **2001**, 20, 1137-1143.
- (24) Ugozzoli, F.; Lanfredi, A. M. M.; Marisch, N.; Camus, A. *Inorg. Chim. Acta*, **1997**, 256, 1-7.
- (25) Rucci, G.; Zanzottera, C.; Lachi, M. P.; Camia, M. *Chem. Comm.* **1971**, 12, 652.
- (26) Balkus, Jr. K. J.; Kortz, A.; Drago, R. S. *Inorg. Chem.* **1988**, 27, 2955-2958.
- (27) Bocuzzi, F.; Ghiotti, G. *Journal de Physiqu, Colloque*, **1983**, C10, 455-458.
- (28) Scarano, D.; Bordiga, S.; Lamberti, C.; Spoto, G.; Ricchiardi, G.; Zecchina, A.; Otero Arean, C. *Surface Sci.* **1998**, 41, 272-285.
- (29) Hadjiivanov, K. I.; Kantcheva, M. M.; Klissurski, D. G. *J. Chem. Soc., Faraday Trans.* **1996**, 92, 4595-4600.
- (30) Lamberti, C.; Bordiga, S.; Zecchina, A.; Salvaleggio M.; Geobaldo, F.; Otero Areán, C. *J. Chem. Soc. Faraday Trans.* **1998**, 94, 1519-1525.
- (31) Scott, A. F.; Wilkening, L. L.; Rubin B. *Inorg. Chem.* **1969**, 8, 2533-2534.

- (32) Ivanova, S. M.; Ivanov, S. V.; Miller, S. M.; Anderson, O. P.; Solntsev, K. A.; Strauss, S. H. *Inorg. Chem.*, **1999**, *38*, 3756-3757.
- (33) Zhou, M.; Andrews, L. *J. Chem. Phys.* **1999**, *111*, 4548-4557.
- (34) Sullivan, R. M.; Martin, J. D. *J. Am. Chem. Soc.* **1999**, *121*, 10092-10097.
- (35) Dattelbaum, A. M.; Martin, J. D. *Polyhedron*, **2006**, *25*, 349-359.
- (36) Dattelbaum, A. M.; Martin, J. D., *Inorg. Chem.*, **1999**, *38*, 6200-6205.
- (37) Martin, J. D.; Leafblad, B. R.; Sullivan, R. M.; Boyle, P. D. *Inorg. Chem.*, **1998**, *37*, 1341-1346.
- (38) Wyckoff, R. W. G.; Posnjak, E. *J. Am. Chem. Soc.* **1922**, *44*, 30-36.
- (39) Kauffman, G. B.; Fang, L. In *Inorganic syntheses*; Holt, S. L., Jr., Ed.; McGraw-Hill: New York, 1983; Vol. XXII, p101.
- (40) Sheldrick, G. M. SHELX, a Program for Crystal Structure Refinement, University of Göttingen, Germany.
- (41) (a) Hammersley, A. P. *FIT2D: An Introduction and Overview*; ESRT Internal Report, ESRF97HA02T; European Synchrotron Radiation Facility: Grenoble Cedex, France, 1997.
- (b) Hammersley, A. P. *FIT2D V9.129 Reference Manual V3.I*; ESRT Internal Report, ESRF98HA01T; European Synchrotron Radiation Facility: Grenoble Cedex, France 1998.
- (42) Norby, P. In-situ Time-Resolved Synchrotron Powder Diffraction Studies of Syntheses and Chemical Reactions. In *European Powder Diffraction*; Cernik, R. J., Delhez, R.,

Mittenmeijer, E. J., Eds.; Materials Science Forum Vol. 228 until 231: Trans Tech Publications; Zürich, Switzerland, 1996; pp 147-152.

(43) (a) Toby, B. H. EXPGUI, a graphical user interface for GSAS, *J. Appl. Cryst.* 2001, 34, 210-221. (b) Larson, A. C. and Von Dreele, R. B. "General Structure Analysis System (GSAS)", Los Alamos National Laboratory Report LAUR 86-748 (2004).

(44) Wendlandt, W. W.; Hecht, H. G. *Reflectance Spectroscopy*; Interscience: New York, 1996; Chapter 3.

Chapter 3:

The Molten Structure of the Templated Copper Chloride Melts

ACu_2Cl_3 (A = monovalent templating cation)

Abstract

The molten structure of ACu_2Cl_3 materials ($A = Cs, H_2N(CH_3)_2$ or $N(CH_3)_4$) have been studied by neutron and X-ray diffraction. The crystalline structures of each of these compounds consist of the same $[Cu_2Cl_3]^-$ double chain. While molten copper chloride does not exhibit a low Q ($<2 \text{ \AA}^{-1}$) first sharp diffraction peak (FSDP), a characteristic of intermediate range order, a FSDP is observed in the melts of the lower symmetry ACu_2Cl_3 compounds. These low Q peaks are correlated with diffraction peaks of the crystalline ACu_2Cl_3 materials corresponding to planar spacings between covalently bound the $[Cu_2Cl_3]^-$ chains. The pair distribution function for $CsCu_2Cl_3$ shows strong evidence that the covalent $[Cu_2Cl_3]^-$ chains persist into the molten state, suggesting they give rise to the observed IRO. The spacing between the $[Cu_2Cl_3]^-$ chains, and thus the position of the FSDP of the melt, in the solid and the molten state is determined by the size of the templating cation A , which provides a means of designing the IRO in ACu_2Cl_3 liquids. The crystal structure of $[H_2N(CH_3)_2]Cu_2Cl_3$, **1**, reported here, exhibits close hydrogen bonding contacts between each dimethylammonium cation and a single $[Cu_2Cl_3]^-$ chain. The hydrogen bonding results in an ion-pairing effect which appears to dramatically lower the melting point of **1** to 130°C in contrast to the much higher melting points of $CsCu_2Cl_3$ and $[N(CH_3)_4]Cu_2Cl_3$ (274° and 230°C respectively).

3.1 Introduction

While commonly perceived as consisting of a disordered state of matter, so called amorphous materials are known to possess order on length scales intermediate between periodic crystalline order (>50 nm) and discrete chemical bonds (<5 nm). The low- Q peak ≤ 1 Å in the neutron diffraction of many network liquids and glasses has been ascribed as a signature of this intermediate range order (IRO). The origin of this first sharp diffraction peak (FSDP) has been a point of controversy in the literature,¹ however, it has been frequently attributed to metal-metal correlations.² Less work has been directed towards developing control over the bonding and structural organization in amorphous liquids and glasses, which may provide a foundation for rational design of materials with specific optical, electronic and mechanical properties. Some investigators have shown that adding network modifying AX salts to network glasses can serve as a means of manipulating intermediate range order (IRO).^{3,4} An alternative approach is explored in this work, where the covalently bonded species in an inorganic solid persist into the melt and are used to design structure into the liquid state. Here, we demonstrate that the covalently bound chains in ACu_2X_3 melts (A = monovalent templating cation, X = Cl, Br), remain intact in the molten state and serve as structural units for designing order into an amorphous material.

Among the materials known to exhibit IRO, glasses and melts of $ZnCl_2$ have received significant attention.^{5, 6,7,8,9,10,11,12} The neutron diffraction, expressed as the total structure factor $S(Q)$, of amorphous $ZnCl_2$ at $Q \geq 2$ Å⁻¹ indicate an amorphous structure consisting of a randomly packed chloride ions. The real-space the pair distribution function (PDF), which is the Fourier Transform of the $S(Q)$ data, indicates that each Zn^{2+} cation is tetrahedrally coordinated by the chlorides, and therefore occupies tetrahedral holes of the randomly

packed network.⁶ The stoichiometry of CuCl requires even greater network formation, yet no first sharp diffraction peak is exhibited in the $S(Q)$ of its melt, suggesting no IRO is present, while the higher Q data suggests a random packed chloride network like that of $ZnCl_2$.¹³ When separated into the contribution of the three individual atom pairings (Cu-Cl, Cl-Cl and Cu-Cu) by an isotopic substitution study, the PDF of CuCl exhibits no chemically meaningful Cu-Cu pair correlations. Since molten CuCl is known to have a high Cu^+ conductivity,¹⁴ the lack of Cu-Cu correlations was interpreted to mean that the cations are highly disordered due to their mobility. In the same study, the Cu-Cl contribution to the PDF suggests a near tetrahedral coordination of copper by chloride. However, a distinct copper coordination seems to be somewhat incompatible with a model proposing disordering due to highly mobile Cu^+ cations. Instead, if the cations remain ordered in the melt, the absence of the first sharp-diffraction peak in CuCl may be related to the high symmetry of its liquid state structure, analogous to its cubic crystal structure for which the diffraction peaks $Q < 2 \text{ \AA}^{-1}$ are systematically absent.¹⁵ Therefore, by lowering the symmetry of CuCl melts, such as by the addition of templating agents, should destroy the systematic absences and may result in low Q diffraction peaks corresponding to any network features of the melt.

We have chosen to study the family of ACu_2Cl_3 materials, with structures consisting of covalently bound copper chloride double chains, which can be thought of as being extracted from the CuCl lattice and should possess lower symmetry melts. Further the relatively low melting points of the ACu_2Cl_3 materials, between 130 and 275°C, suggested they might be ideal candidates for an examination of the structure of their liquid state to determine if their anisotropic chain structure may be preserved in the molten state. Comparison of the series of previously known ACu_2Cl_3 compounds where $A = [Cs]^+$ and

$[\text{NMe}_4]^+$ as well as $[\text{H}_2\text{NMe}_2]^+$, whose structure is first reported here, probes the effect of template size and interchain bonding interactions on the melt structures of these materials.

In this work we discuss the structural, melt and bonding characteristics in the family of templated metal halides AM_2X_3 (A = monovalent templating cation; M = Cu, Ag, X = Cl, Br, I). These structures consist of covalent double chains of composition $[\text{M}_2\text{X}_3]^-$ built from edge shared MX_4 tetrahedra. In the all inorganic AM_2X_3 materials of this structure type, (A = Rb^+ or Cs^+) the template participates in the halide close packing, while use of larger organic templates, results in the same basic M_2X_3 double chain motif but disrupts the close packed network.

3.2 Results & Discussion

*Crystal Structure of $(\text{H}_2\text{N}(\text{CH}_3)_2)\text{Cu}_2\text{Cl}_3$, **1***

A summary of the crystallographic data for $(\text{H}_2\text{NMe}_2)\text{Cu}_2\text{Cl}_3$ is given in Table 3.1 with selected bond distances and angles listed in Table 3.2. The structure, shown in Figure 3.1, consists of double chains of stoichiometry $[\text{Cu}_2\text{Cl}_3]^-$ running along **b**. The anionic cuprous halide chain is essentially isostructural with a number of published crystal structures, listed in Table 3.3, with the AM_2X_3 composition (A = monovalent templating cation, M = Cu or Ag, X = Cl, Br or I). The copper atoms of a given single chain of **1** lie are nearly coplanar and each is tetrahedrally coordinated to four chlorides. Each copper centered tetrahedron shares edges with three neighboring tetrahedra to propagate the chain. Neighboring chains are related either by the 2_1 -screw axis or by translation. Two-thirds of the chlorides in each chain are two coordinate and form the outer edge of the chain, while the remaining chlorides

are four-coordinate and are shared among four copper centered tetrahedra. The μ^4 -chlorides alternate faces of the chain and form the apex of a distorted square pyramid with four copper atoms serving as the base. The tetrahedra are very distorted, with relatively short bonds between copper and the μ^2 -chlorides (Cu-Cl(1) 2.28-2.29 Å, Cu-Cl(2) 2.27-2.28 Å) while the bonds to the μ^4 -chlorides are distances are slightly longer (Cu-Cl(3) 2.446, 2.587 Å). The Cl-Cu-Cl bond angles are accordingly distorted away from an ideal tetrahedron as given in Table 3.2, with the Cl_{μ^2} -Cu- Cl_{μ^2} bond angles being most distorted ($\sim 128.5^\circ$). Each copper has two different Cu-Cu nearest-neighbor contacts, with two equivalent contacts of 2.91 Å along the direction of chain propagation and a longer contact of 3.05 Å perpendicular to direction of the chain propagation. A similar distortion is observed in a majority of the AM_2X_3 structures, which calculations suggest is the result of maximizing the Cu-Cu orbital overlap that occurs along the chain.¹⁶

The $[\text{Cu}_2\text{Cl}_3]^-$ chains are surrounded by the dimethylammonium cations which are organized in a pseudo-hexagonal arrangement. Each dimethylammonium cations are located within a rectangular anti-prism defined by a pair of μ^2 -chlorides from each of the three neighboring chains as well as two μ^4 -chlorides from one of the chains. Neighboring chains in **1** are slightly staggered to accommodate the non-spherical dimethylammonium cation, which gives rise to the monoclinic unit cell. Pairs of dimethylammonium cations, related by inversion symmetry, are hydrogen bonded to the μ^2 -chlorides on either side of a single chain, as shown in the ORTEP plot in Figure 1b, with distances of H(1)-Cl(1) 2.48 Å and H(2)-Cl(2) 2.64 Å.

Table 3.1. Summary of Crystal Data for (H₂NMe₂)Cu₂Cl₃, **1**.

Formula weight	279.54
Temperature (°C)	-128
Space Group	<i>P</i> 2 ₁ / <i>c</i>
<i>a</i> (Å)	10.80097(0)
<i>b</i> (Å)	12.53075(0)
<i>c</i> (Å)	5.81046(0)
β (°)	99.49300(0)
<i>V</i> (Å ³)	775.64
<i>Z</i>	4
<i>R</i>	0.040
<i>R_w</i>	0.049

Table 3.2. Selected Bond Distances and Angles for (H₂NMe₂)Cu₂Cl₃, **1**.

Atoms	Distance (Å)	Atoms	Angle (degrees)
Cu(1)-Cl(1)	2.2804(8)	Cl(1)-Cu(1)-Cl(1)a	128.50(3)
Cu(1)-Cl(1)a	2.2887(8)	Cl(1)-Cu(1)-Cl(3)	102.30(3)
Cu(2)-Cl(2)	2.2743(8)	Cl(1)-Cu(1)a-Cl(3)	110.03(3)
Cu(2)-Cl(2)a	2.2820(8)	Cl(1)a-Cu(1)-Cl(3)	103.41(3)
Cu(1)-Cl(3)	2.4492(8)	Cl(1)a-Cu(1)a-Cl(3)	105.16(3)
Cu(1)-Cl(3)a	2.5480(8)	Cl(3)-Cu(1)-Cl(3)a	105.12(3)
Cu(2)-Cl(3)	2.5729(8)	Cl(2)-Cu(2)-Cl(2)a	128.44(3)
Cu(2)-Cl(3)a	2.4430(8)	Cl(2)-Cu(2)-Cl(3)	101.76(3)
Cu(1)-Cu(1)	2.9090(6)	Cl(2)-Cu(2)a-Cl(3)	110.15(3)
Cu(2)-Cu(2)	2.9100(6)	Cl(2)a-Cu(2)-Cl(3)	103.35(3)
Cu(1)-Cu(2)	3.0548(6)	Cl(2)a-Cu(2)a-Cl(3)	105.61(3)
Cl(1)-H(1)	2.642(42)	Cl(3)-Cu(2)-Cl(3)a	104.55(3)
Cl(2)-H(2)	2.477(46)		

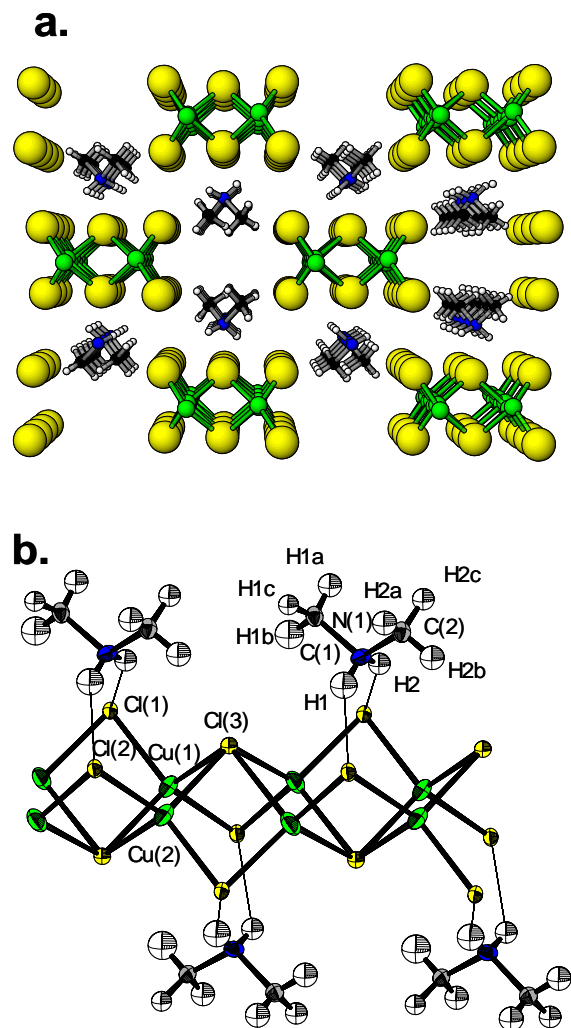


Figure 3.1: (a) Crystal structure of **1** viewed down the direction of chain propagation.

(b) ORTEP (50% probability ellipsoid) of **1**, emphasizing the hydrogen-bonding between the templating cations and a single $[\text{Cu}_2\text{Cl}_3]^-$ chain.

Table 3.3. Crystal Symmetry and Melting Points of AM_xX_y Chain Structures

AM ₂ X ₃ Structures	Melt Temperature (°C)	Crystal Symmetry	Reference
(H ₂ NMe ₂)Cu ₂ Cl ₃	128	<i>P2₁/c</i>	This work
(NMe ₄)Cu ₂ Cl ₃	230	<i>Pnma</i>	17
CsCu ₂ Cl ₃	274	<i>Cmcm</i>	18, 19, 20
CsCu ₂ Br ₃	363	<i>Cmcm</i>	21,22
RbCu ₂ Br ₃	264	<i>Cmcm</i>	21, 23
(Me ₂ N ₂ CHN ₂ Me ₂)Cu ₂ Br ₃	Unknown	<i>P-1</i>	24
(H ₂ NMe ₂)Cu ₂ Br ₃	160	<i>P2₁/c</i>	This work
RbCu ₂ I ₃	Melts incongruently @~300	<i>Pbnm</i>	19, 21
CsCu ₂ I ₃	383	<i>Cmcm</i>	21, 25
(SMe ₃)Cu ₂ I ₃		<i>Pnma</i>	26
(C ₅ H ₅ NCH ₃)Cu ₂ I ₃	164	<i>Pnma</i>	27
CsCu ₂ Cl ₂ I	Unknown, 273<383	<i>P2₁/m</i>	28
CsCu ₂ ClI ₂	Unknown, 273<383	<i>Cmcm</i>	28
(NEt ₄)Ag ₂ Cl ₃	206-7	<i>Pnma</i>	29
(NEt ₄)Ag ₂ Br ₃	225	<i>Pnma</i>	29
(NMe ₄)Ag ₂ Br ₃	Unknown	<i>Pnma</i>	30
CsAg ₂ I ₃	210	<i>Pbnm</i>	21, 31
(NMe ₄)Ag ₂ I ₃	Unknown	<i>Pnam</i>	32
ACu₃X₄ Structures			
dmf ₂ Cu ₃ ClI ₃ ⁱ	125	<i>Pccn</i>	27
dmf ₂ Cu ₃ Br ₂ I ₂ ⁱ	148	<i>Pccn</i>	27
dmf ₂ Cu ₃ I ₄ ⁱ	146	<i>Pccn</i>	27

i. dmf = dimethylforamidinium

While the $[\text{Cu}_2\text{Cl}_3]^-$ chain in **1** is essentially isostructural with the compounds listed Table 3.3, the AM_2X_3 composition exhibit different variations in crystal symmetry depending primarily on the identity of the template. The crystal symmetries of each composition are listed in Table 3.3 and representatives of the symmetry variants are depicted in Figure 3.2. As in **1**, the cations in each compound arrange in a pseudo hexagonal fashion around the $[\text{M}_2\text{X}_3]^-$ anion chains. The templating cations of this structure type are located within a rectangular anti-prism defined by a pair of μ^2 -halides from each of the three neighboring chains as well as two μ^4 -halides from one of the chains. In addition to **1**, only two other AM_2Cl_3 compounds are known: CsCu_2Cl_3 and $(\text{NMe}_4)\text{Cu}_2\text{Cl}_3$. The cesium structure, shown in Figure 3.3a represents the highest crystal symmetry with the $[\text{M}_2\text{X}_3]^-$ cation, *Cmcm*. In CsCu_2Cl_3 , as well as the other structures where A is an alkali cation, both the $[\text{Cs}]^+$ and $[\text{Cl}]^-$ serve as close packing ions due to their similar size. Each close packed layer consists of the slice through the 221 plane of CsCu_2Cl_3 , shown in Figure 3.3a, and contain six chlorides and two cesium cations per chain. Figure 3.3b depicts one of the $[\text{Cs}]^+$ cations within the rectangular anti-prism defined by chlorides from three neighboring chains, analogous to the cation position in **1**, and highlights three layers of the *hcp* close packing of the lattice built in part from the chlorides which define the rectangular anti-prism. Despite its lower symmetry, **1** also consists of $[\text{H}_2\text{NMe}_2]^+/\text{Cl}^-$ close packed planes, shown in Figure 3.4, while the larger tetramethylammonium cation disrupts the halide close packing $(\text{NMe}_4)\text{Cu}_2\text{Cl}_3$.

The size of the templating cation of ACu_2Cl_3 influences the unit cell size of each crystal structure, with room temperature cell volumes of 632, 796, and 984 \AA^3 for $[\text{Cs}]^+$, $[\text{H}_2\text{NMe}_2]^+$ and $[\text{NMe}_4]^+$ respectively. The cations in the $[\text{Cs}]^+$ and $[\text{NMe}_4]^+$ compounds are reasonably symmetrically located within the chlorides defining the prism, with modest

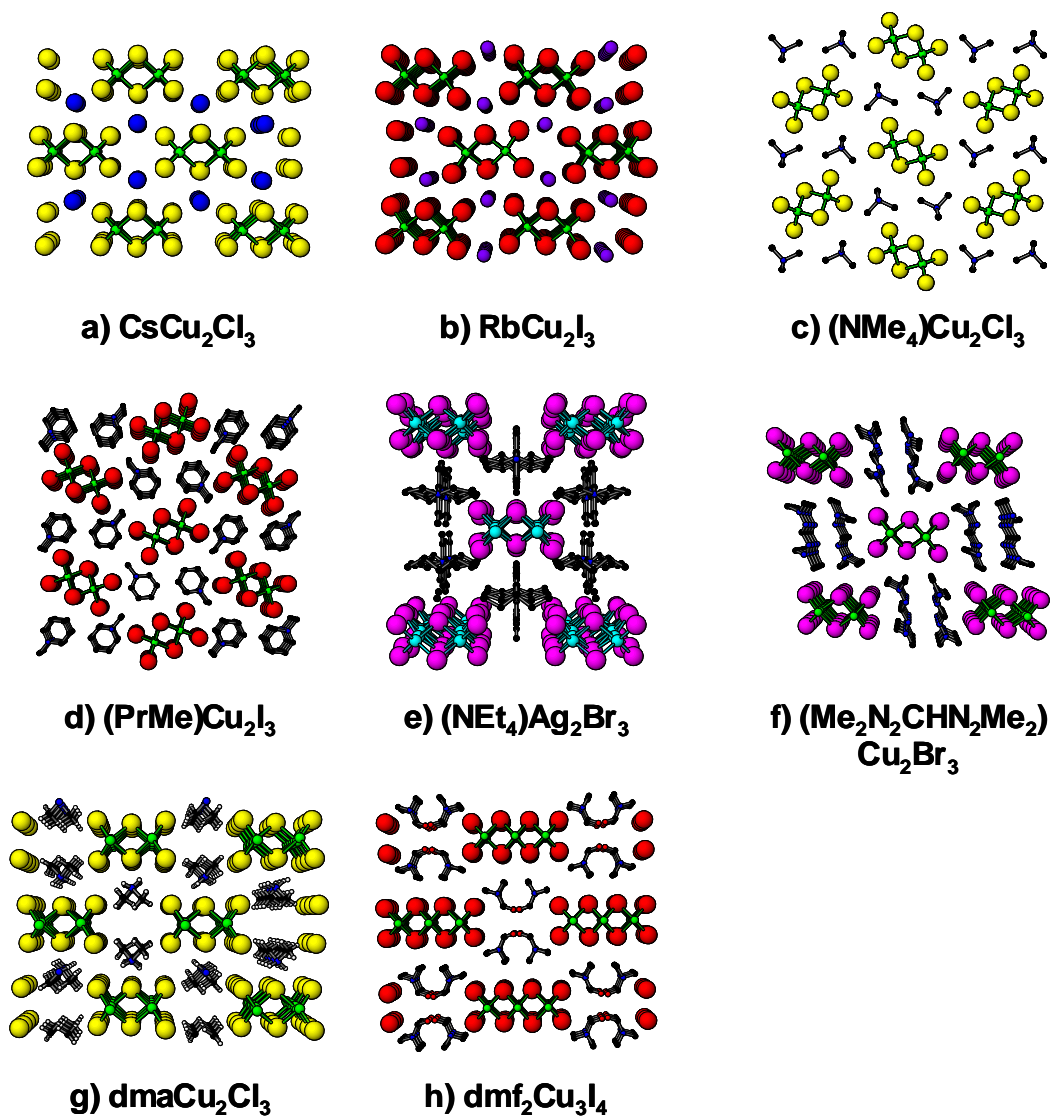


Figure 3.2: Representative examples of known AM_2X_3 chain structures. The packing arrangements of the $[\text{M}_2\text{X}_3]^-$ chains varies depending on the size and shape of the templating cation, where small cations (Rb^+ , Cs^+) form close packed layers with the halide while larger cations disrupt the close packing to give a variety of structures.

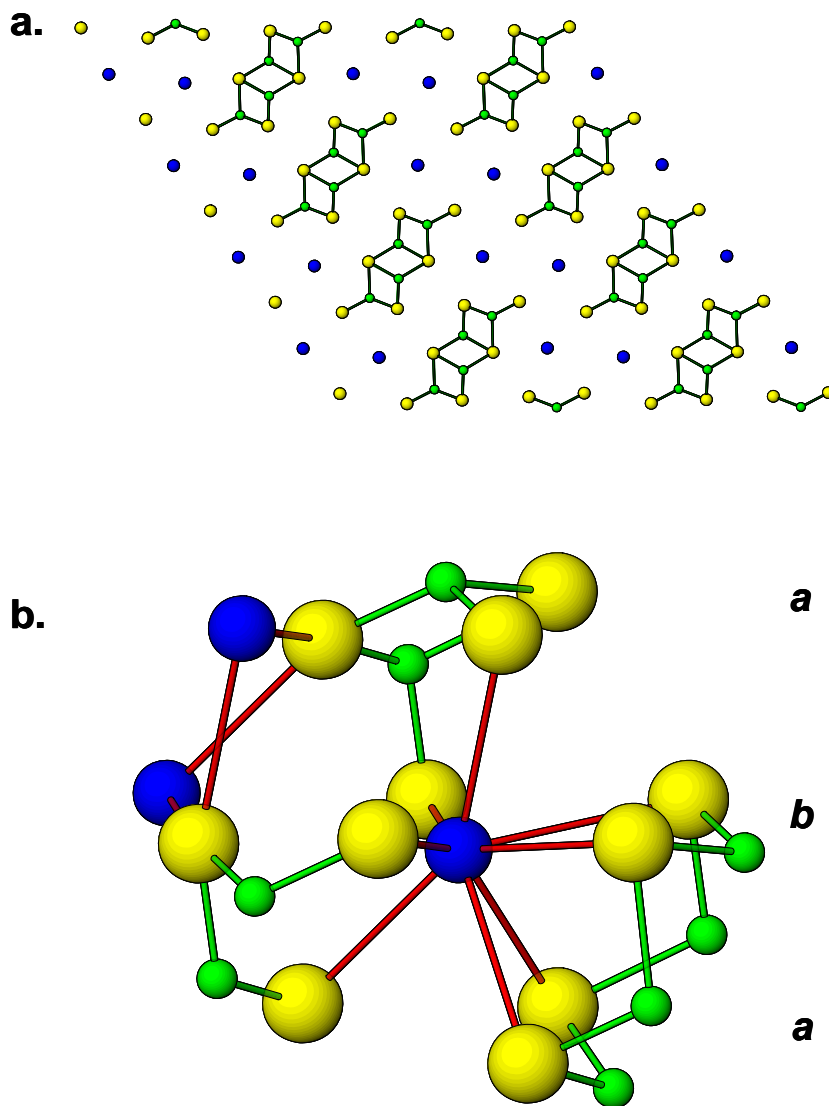


Figure 3.3: (a) Slice taken through the 221 lattice planes of CsCu_2Cl_3 showing a single pseudo-closed packed layer of $[\text{Cs}]^+$ templating cations and $[\text{Cl}]^-$ anions. (b) A view of CsCu_2Cl_3 highlighting the coordination geometry around $[\text{Cs}]^+$ with bonds drawn in red to the chlorides forming the rectangular anti-prism. Each chloride is labeled to indicate which chain it is associated with (numbered 1-3) as well as its coordination to copper. The $[\text{Cs}]^+$ and $[\text{Cl}]^-$ ions combine to show three pseudo close-packed layers.

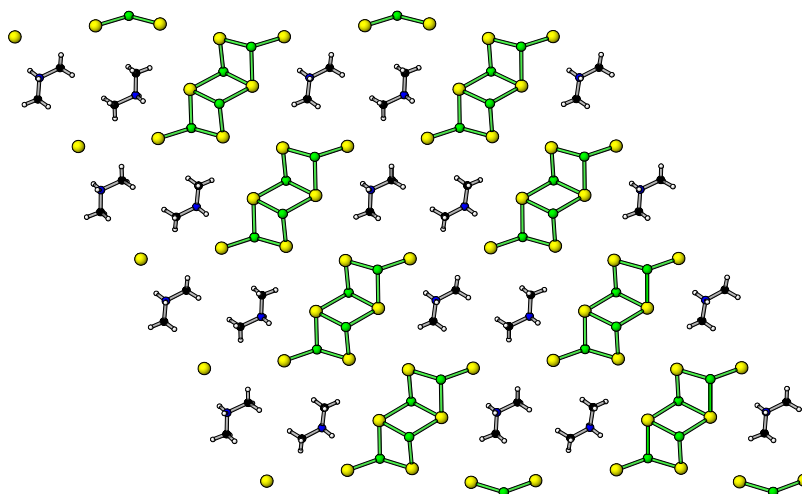


Figure 3.4: Slice taken through the 221 lattice planes of $[\text{H}_2\text{NMe}_2]\text{Cu}_2\text{Cl}_3$, **1**, showing a single pseudo-closed packed layer of $[\text{H}_2\text{NMe}_2]^+$ templating cations and $[\text{Cl}]^-$ anions, analogous to the close packed layer of CsCu_2Cl_3 .

contacts to each neighboring chain of Cs-Cl ~ 3.6 Å and ~ 4.3 - 4.8 Å respectively. In compound **1**, however, NH-Cl hydrogen bonding results in a strong association between each cation and a single cuprous chloride chain with N-Cl contacts to one chain and much weaker contacts of 3.5 - 5.0 Å to the other two neighboring chains.

[H₂NMe₂]Cu₂Cl_{3-y}Br_y Solid Solutions.

The bromide material (H₂NMe₂)Cu₂Br₃, **2**, was prepared by a melt reaction of H₂NMe₂Br and CuBr. Powder X-ray diffraction of **2** confirmed that it is isostructural to **1**. The powder diffraction of mixed halide compositions in Figure 3.5, show single phase products rather than a mixture of **1** and **2**, suggesting there exists a range of solid solutions (H₂NMe₂)Cu₂Cl_{3-y}Br_y. Lattice parameters refined for specific compositions are given in Table 3.4. The unit cell volume increases linearly with increasing bromide content (Figure 3.5a), following Vegard's Law for solid solutions. However, the changes in the a , c and β lattice constants are not linear over the entire range $0 < y < 3$, as shown in Figure 3b-e. In the range $0 \leq y \leq 1$ a decreases while β and c increase with increasing bromide content, while for $y > 1$ all three parameters increase. This discontinuity in the lattice constants is consistent with a special composition at $y = 1$, (H₂NMe₂)Cu₂Cl₂Br. The special composition coincides with the tendency of the larger halide to preferentially occupy the μ^4 -halide positions. The bromide favors the μ^4 position since it can more readily accommodate bonds to four copper atoms and because it avoids disrupting the stronger Cu- μ^2 -Cl covalent bonds. Therefore in the range $0 < y < 1$, bromide disorders over the crystallographic X(3) halide site and completely occupies this site at the composition $y = 1$. At compositions where $y > 1$, the bromides fully occupy the X(3) site and begins occupying the remaining μ^2 sites. That the

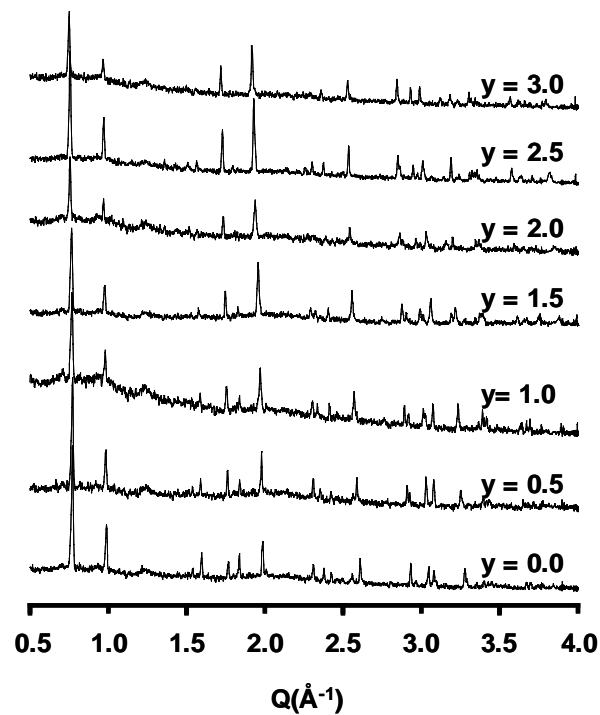


Figure 3.5: Room temperature X-ray diffraction of the mixed halide solid solutions $(\text{H}_2\text{NMe}_2)\text{Cu}_2\text{Cl}_{3-y}\text{Br}_y$ for selected compositions.

Table 3.4. Room Temperature Lattice Constants For $(\text{H}_2\text{NMe}_2)\text{Cu}_2\text{Cl}_{3-y}\text{Br}_y$

Composition (y)	a (Å)	b (Å)	c (Å)	β (°)	Volume (Å ³)
0.00	10.789(7)	12.70(1)	5.893(5)	99.30(6)	796(1)
0.25	10.78(1)	12.74(1)	5.915(3)	99.39(7)	802(1)
0.50	10.761(5)	12.762(9)	5.950(3)	99.18(6)	806.7(6)
0.75	10.755(5)	12.780(8)	5.977(3)	99.13(4)	811.2(6)
1.00	10.76(1)	12.80(2)	5.996(8)	99.1(1)	816(3)
1.25	10.777(6)	12.782(7)	6.046(5)	99.08(5)	822.6(9)
1.50	10.809(9)	12.87(1)	6.036(5)	98.96(8)	830(1)
1.75	10.846(7)	12.884(7)	6.052(3)	99.04(7)	835.3(7)
2.00	10.91(1)	12.958(7)	6.056(4)	99.40(7)	845(1)
2.25	10.903(7)	12.867(6)	6.106(3)	99.05(3)	846.0(6)
2.50	11.05(2)	12.96(2)	6.09(1)	98.73(8)	861(3)
2.75	11.063(8)	12.988(8)	6.080(3)	98.70(6)	863.7(9)
3.00	11.16(1)	13.00(1)	6.09(1)	98.9(1)	872(2)

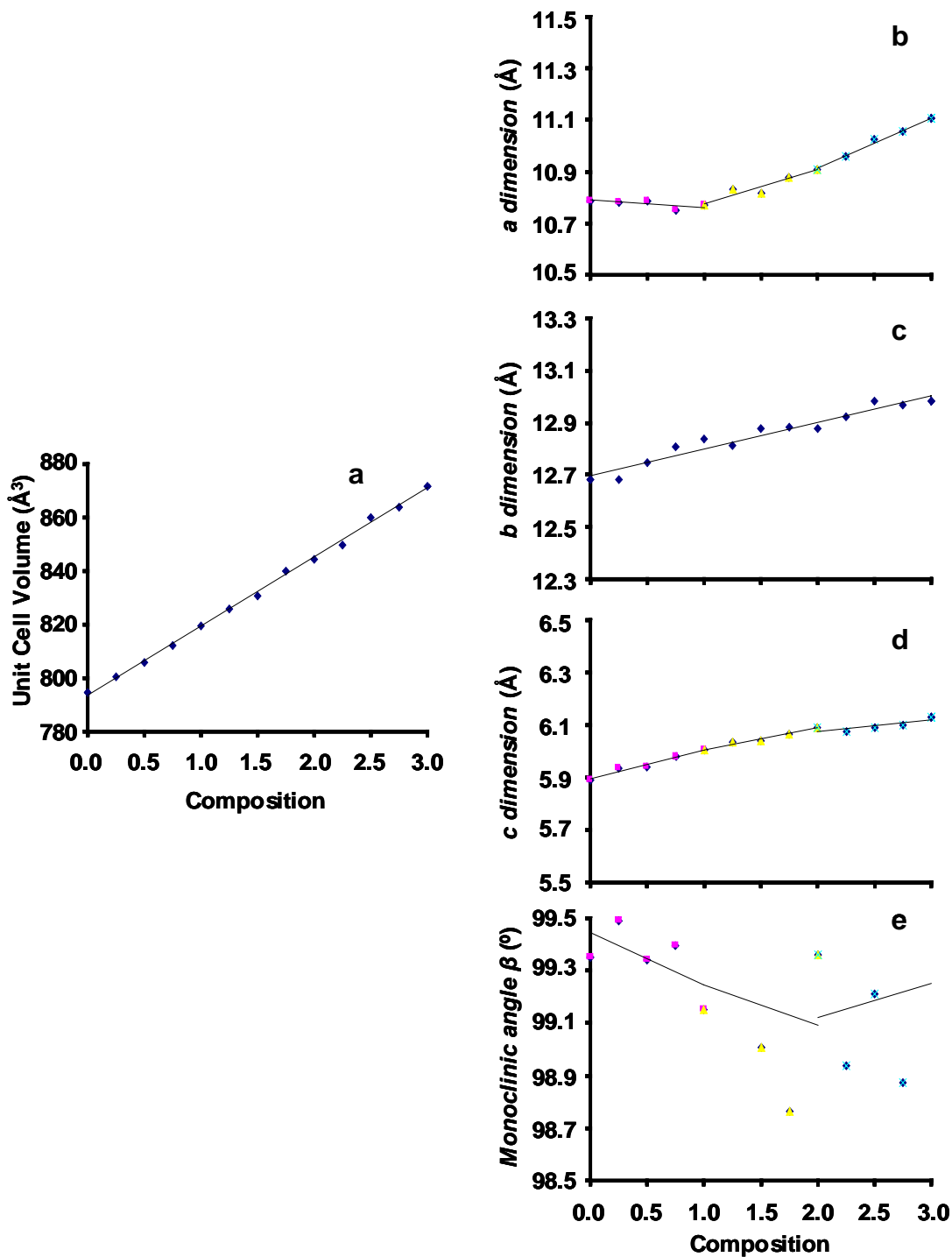


Figure 3.6: Unit cell volumes and lattice parameters of the mixed halide solid solution $(\text{H}_2\text{NMe}_2)\text{Cu}_2\text{Cl}_{3-y}\text{Br}_y$ as a function of bromide content y .

larger halide favors the μ^4 position is consistent with crystal structures solved by Geller and coworkers for $\text{CsCu}_2\text{Cl}_2\text{I}$ and $\text{CsCu}_2\text{ClI}_2$ in the $\text{CsCu}_2\text{Cl}_{3-y}\text{I}_y$ solid solution system,^{28,33} and with mixed halide structures of the formula $\text{A}_2\text{M}_3\text{X}_4$ (A = dimethylformamidinium, M = Ag, Cu, X = Cl, Br, I) composed of a metal halide triple chain of similar structure to the Cu_2X_3 double chains.³⁴ A second change in slope in a and β at $y = 2$ suggests another special composition, $(\text{H}_2\text{NMe}_2)\text{Cu}_2\text{ClBr}_2$. This suggests that one of the two crystallographically independent $\text{X}_{\mu 2}$ sites is occupied by bromide, most likely the site associated with the weaker hydrogen bonding contact, Cl(2). By contrast, in the reported crystal structure of $\text{CsCu}_2\text{ClI}_2$ all of the μ^4 halide positions are occupied by iodide, while the remaining iodide is disordered over the two crystallographically distinct μ^2 positions. A special composition at $y = 2$ is likely only observed for mixed halide AM_2X_3 solid solutions if three crystallographically distinct halide positions are present in the monohalide.

Melt Properties of AM_2X_3 Compounds.

The melting points of the known AM_2X_3 compounds, which in part prompted this research due to their relatively low temperatures, are listed in Table 3.3. Here we consider the effects of different bonding interactions on some trends observed in the melting points, as well as some abnormalities in these trends. Understanding the origin of each trend is relevant to designing structure in the liquid state since low temperature melts may be more likely to preserve the covalently bonded $[\text{M}_2\text{X}_3]^-$ chain. For instance, the melting points in the of the three ACu_2Cl_3 compounds are expected vary in accordance to Coulomb's Law, which states that the electrostatic force between charged particles is inversely proportional to the square of the distance between them. As the size of the templating cation increases, the ions are

separated farther apart, which should result in a weakening of the electrostatic attraction between them. Therefore, the predicted melting points should decrease with increasing unit cell volume in the order $[\text{Cs}]^+ > [\text{NH}_2\text{Me}_2]^+ > [\text{NMe}_4]^+$. Using differential scanning calorimetry (DSC), we have found the melting points to be 274°C for CsCu_2Cl_3 , 230°C for $(\text{NMe}_4)\text{Cu}_2\text{Cl}_3$, but only 128°C for **1**. Surprisingly, while the decrease in melting point for the $[\text{Cs}]^+$ and $[\text{NMe}_4]^+$ materials is in keeping with the expected trend, the $[\text{H}_2\text{NMe}_2]^+$ material exhibits a much lower melting point than the other two compounds, and in fact possesses the lowest reported melting point of the AM_2X_3 materials (Table 3.3).

Generally melting points are linked to the weakest attractive forces in a solid. For example, the hydrogen bonding in ice is disrupted on melting while the covalent O-H bonds remain intact. In CsCu_2Cl_3 and $(\text{NMe}_4)\text{Cu}_2\text{Cl}_3$ the weakest forces are simply the electrostatic attraction between the cations and anions. As described above and as pictured in Figures 3.2a and 3.2b, since each $[\text{A}]^+$ cation is associated with three $[\text{Cu}_2\text{Cl}_3]^-$ chains the overall ionic bonding is distributed among groups of neighboring chains. In the case of **1**, the strong hydrogen bonds between $[\text{H}_2\text{NMe}_2]^+$ and a single $[\text{Cu}_2\text{Cl}_3]^-$ chain form a tight cation-polymer ion pair, whereas the cation has much weaker interactions with other neighboring chains. While hydrogen bonding in water leads to network formation and therefore a higher melting point, in **1** it results in molecular-like units of consisting of the ion pairs. Therefore the weakest attractive forces are those between ion pairs, which are not as strong as the ionic interactions in CsCu_2Cl_3 and $(\text{NMe}_4)\text{Cu}_2\text{Cl}_3$, and **1** exhibits a correspondingly low melting point.

In contrast to the trend in unit cell size and melt temperatures predicted for ACu_2Cl_3 , substitution of larger halides results higher melting points with increasing unit cell volume.

For instance, as listed in Table 3.4 where A = Cs the melting points increase with increasing halide size (m.p = 274, 363 and 383°C while unit cell volume = 632, 709 and 847 Å³ for X = Cl, Br and I respectively). The origin of this trend on halide substitution is likely the increasing ionic character of the Cu-X bond, which corresponds to decreasing electronegativity with halide size. As the Cu-X bond becomes more ionic, the halide will possess greater negative charge character, resulting in stronger ionic interactions between the chain and the templating cation. The stronger ionic bonding apparently plays a larger role in determining the melting point than the unit cell volume.

The melting point of the bromide **2** was found to be 160°C by DSC (Table 3.4), approximately 30°C higher than that of **1**, and is in agreement with the trend in melting points on halide substitution. The melting points measured for the solid-solutions (H₂NMe₂)Cu₂Cl_{3-y}Br_y are shown as a function of composition y in Figure 3.7. Instead of increasing linearly over the entire composition range or exhibiting eutectic behavior as might be expected for a typical solid solution, the melting points increase gradually over the range 0 < x < 1.5 and the more sharply for x > 1.5. This unusual behavior is likely attributable to the differing impacts on the melting point of the μ² and μ⁴ halide sites due to effects of hydrogen bonding. The μ⁴-chlorides which are replaced across the compositional range 0 < y < 1 are only weakly involved in the hydrogen bonding and are effectively isolated in the middle of the [H₂NMe₂]⁺/[Cu₂X₃]⁻ ion pair with no direct contacts to neighboring pairs. By contrast, replacing the μ² sites with bromide weakens the strong hydrogen bonding contacts that give rise to the ion pairing and the low melting point of **1**. The melting points should increase slowly over the composition range 0 < y < 1 where the hydrogen bonding is least affected, and then more significantly for y > 1. The actual melting points in Figure 3.7 closely follow

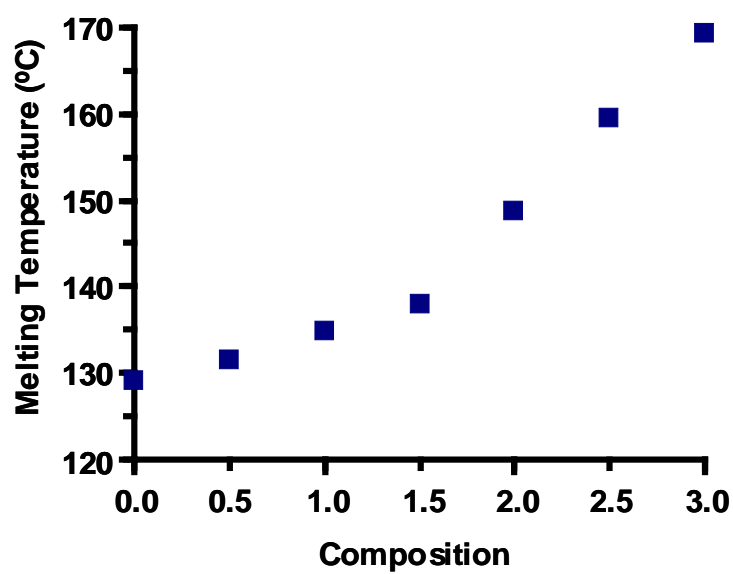


Figure 3.7: Measured melting points of selected compositions of mixed halide solid solution $(\text{H}_2\text{NMe}_2)\text{Cu}_2\text{Cl}_{3-y}\text{Br}_y$ as a function of bromide content y .

this trend, with a gradual increase of melting points over the range $0 \leq y \leq 1.5$ and a more substantial rate of increase with $y \geq 1.5$. The lower than expected melting point at $y = 1.5$ may be due to a maximum in the entropy of mixing at this composition.

We point out that still lower melting points may be possible in these systems. For instance this might be achieved by designing a structure that incorporates both hydrogen bond directed ion pairing and lower charge density ions. Alternatively, simple halide substitutions, such as replacing an iodide with chloride may result in structures with very low melting points, which, as described above, results in more than a 100°C drop for CsCu_2X_3 (m.p. are 273, and 383°C for $\text{X} = \text{Cl}$ and I respectively). Similarly, the $\text{A}_2\text{M}_3\text{X}_4$ discovered by Hartl and coworkers have only been found where at least 2 halides per unit cell are iodide.³⁴ The metal halide triple chain motif results in a lower charge density anion as such these materials melt as low as 125°C. Interestingly, their attempt at synthesizing an all chloride analogue failed to yield a crystalline material, but rather produced a yellow liquid product at room temperature that has not yet been characterized. Prior to the discovery of **1**, the reported melting points in Table 3.3 reveal that the lowest known melting AM_2X_3 compound was $(\text{C}_5\text{H}_5\text{NMe})\text{Cu}_2\text{I}_3$. The low charge density N-methylpyridinium cation gives a melting point of 164°C, over 200°C lower than its cesium analogue CsCu_2I_3 , a substantially larger decrease than is observed for the dimethylammonium cation. A chloride or bromide analogue of this structure should exhibit a melting point below 164°C. Given the placement the N-methylpyridinium in $(\text{C}_5\text{H}_5\text{NMe})\text{Cu}_2\text{I}_3$, shown in Figure 3.2d, replacement with pyridinium may yield a new structure with hydrogen bonding which closely associates with two chains with each cation which could reduce the melting point further still.

Intermediate Range Order in ACu_2Cl_3 Melts

To probe the structure of molten AM_2X_3 materials, we performed the neutron and synchrotron X-ray diffraction experiments on ACu_2Cl_3 melts. Of the three known ACu_2Cl_3 compounds, $CsCu_2Cl_3$ is most readily compared to other work on molten metal halides since its crystalline structure is based on a pseudo-close packing arrangement. Figure 3.8 gives the neutron diffraction for molten $CsCu_2Cl_3$, $CuCl$ ¹³ and $CsCl$ ³⁵ plotted as the total neutron structure factor $S(Q)$, as well as the pair distribution functions for each melt, obtained from the inverse Fourier transform of the neutron structure factor data. As mentioned previously, molten $CuCl$ exhibits no low Q diffraction peak, which has been attributed to highly mobile and therefore disordered $[Cu]^+$ cations.¹³ Molten $CsCl$ also has no low Q diffraction peak and its structure consists of random packing of $[Cs]^+$ and $[Cl]^-$ each with a coordination number of ~ 6 .³⁵ If the melt structure of $CsCu_2Cl_3$ is simply based on random packing of spheres with little contribution from a covalent chain structure, its diffraction might be expected to possess structure similar to its constituent binary metal halides. Instead, the neutron diffraction of molten $CsCu_2Cl_3$ at $300^\circ C$ shows a low Q peak around 0.91 \AA^{-1} indicative of some IRO.

The broad amorphous scattering peaks in the diffraction from $CsCu_2Cl_3$ are highly correlated with Bragg diffraction peaks observed for its crystal structure. Knowledge of the specific lattice planes which give rise to the crystalline diffraction for $CsCu_2Cl_3$ provide indication of what features gives rise to the structure in the molten state. The structure factors for this material are significantly different for the scattering of neutrons by the elemental nuclei and the scattering of X-rays by the electron density. Thus the observed structure factors are distinct for each radiation source. The X-ray diffraction of molten

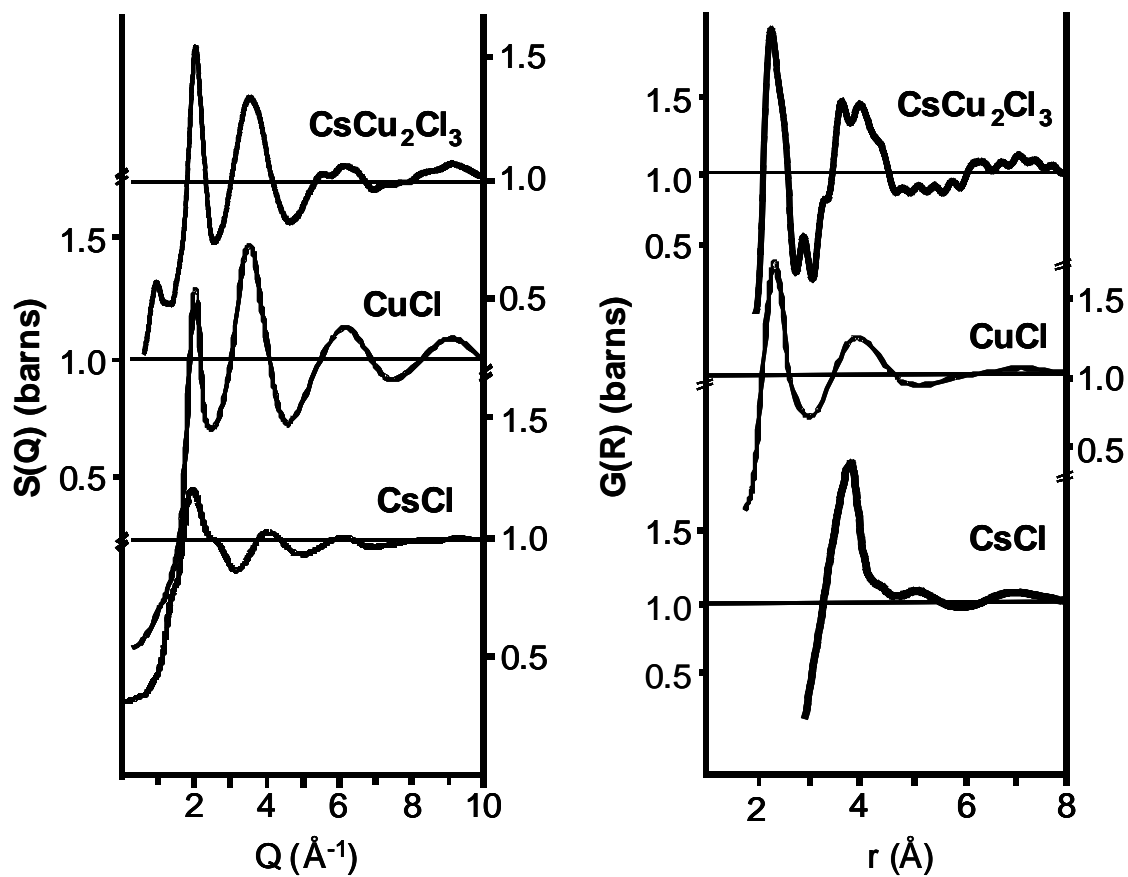


Figure 3.8: Structure factor $S(Q)$ and pair distribution $G(r)$ plots comparing the molten structures CsCu_2Cl_3 , CuCl and CsCl . Data for CuCl^{13} and CsCl^{35} were scanned from the referenced reports.

CsCu₂Cl₃ shows a pair of amorphous diffraction peaks at $Q \approx 1.6 \text{ \AA}^{-1}$, which correlates to a combination of the 111, 220 and 130 peaks, and at $Q \approx 2.0 \text{ \AA}^{-1}$ that correlates with the 221 peak, all of which are also prominent in the calculated X-ray pattern for CsCu₂Cl₃ as shown in Figure 3.9a. By contrast, the calculated neutron diffraction pattern suggest that the 110, 020 and 221 peaks should exhibit the strongest diffraction, as is also observed in the amorphous scattering, Figure 3.9b. The amorphous scattering at $Q \sim 2 \text{ \AA}^{-1}$ correlated with the 221 crystalline diffraction peak associated with the closed packed layers of [Cs]⁺ and [Cl]⁻ ions pictured Figure 3.10a. In agreement with the observation of amorphous structure related to the close-packed [Cs]⁺/[Cl]⁻ layers, the scattering associated with the 111 crystalline peak is consistent with structural order due to layering of cesium ions (Figure 3.10b). The shoulder in the amorphous neutron pattern near $Q = 1.6 \text{ \AA}^{-1}$ may correlate to the crystalline 220 peak. The broad diffraction features between $Q = 3-4 \text{ \AA}^{-1}$ seem to correlate with several crystalline diffraction peaks, including the 350, 332, 440, 402 and 170. The low Q diffraction peak at $\sim 0.9 \text{ \AA}^{-1}$ which signifies the presence of IRO in molten CsCu₂Cl₃ correlates most strongly to the 110 crystalline peak, with some possible contribution from the 020. The 110 and 020, as well as the higher order 220 and 440 observed at higher Q, are associated with the separation between the [Cu₂Cl₃]⁻ chains in the crystal, as pictured in Figures 3.10c and 3.10d. Observation of these low Q peaks in the amorphous scattering implies that some element of the chain persists in the melt and serves as the structural unit which gives rise to the observed IRO.

The effect of changing the templating cation on the molten structure of ACu₂Cl₃ was probed by studying the amorphous diffraction of the [H₂NMe₂]⁺ and [NMe₄]⁺ symmetry variants. As observed with CsCu₂Cl₃, the scattering of neutrons and X-rays scattering by **1**

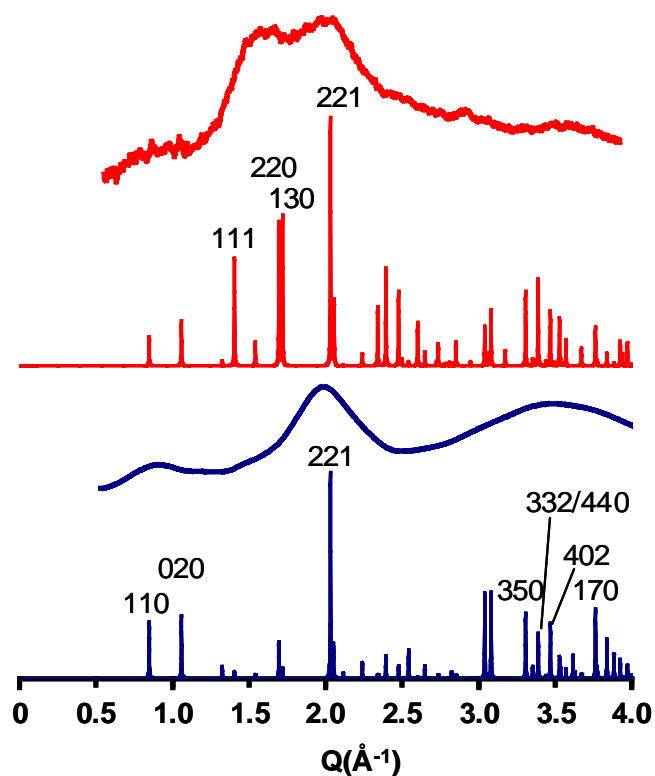


Figure 3.9: X-ray (red) and neutron (blue) diffraction patterns of crystalline and molten CsCu_2Cl_3 . The molten diffraction patterns (a and c) were collected at 300°C while the crystalline diffraction patterns were calculated for the two different radiation sources using the room temperature lattice constants for CsCu_2Cl_3 (b and d). The amorphous scattering is closely correlated with the labeled crystalline diffraction peaks.

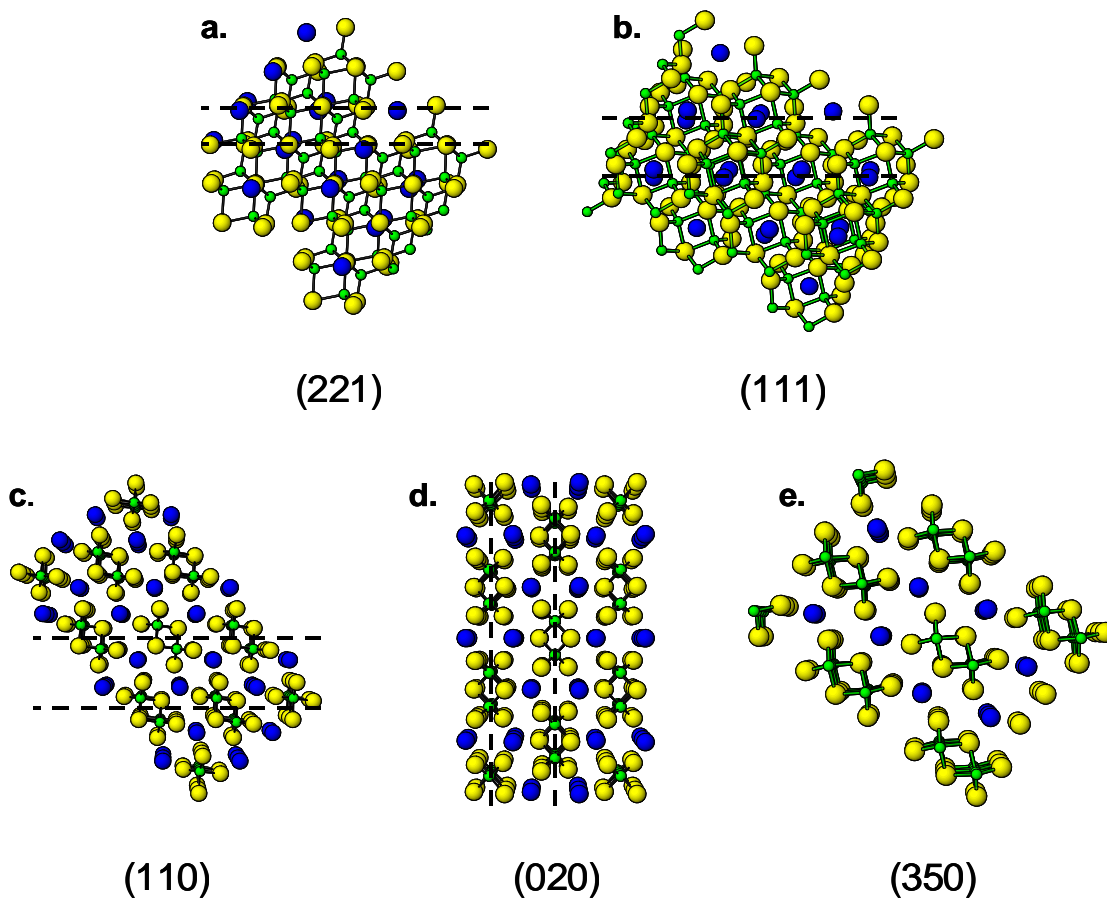


Figure 3.10: Spacings between the crystalline lattice planes correlated to the amorphous diffraction of molten CsCu_2Cl_3 . The 221 and 111 plane spacings correspond to the distance between $[\text{Cs}]^+ / [\text{Cl}]^-$ close packed planes and planes of $[\text{Cs}]^+$ cations respectively. The 110 and 020 plane spacings are related to the distance between $[\text{Cu}_2\text{Cl}_3]^-$ chains.

give two distinct structure factors as shown in Figure 3.11. A fully deuterated sample of **1** was used for the neutron experiments to avoid complications due to the negative neutron scattering cross-section of ^1H . The sample used for the X-ray experiments was of natural isotopic abundance. The amorphous peaks observed by X-ray radiation are correlated with the 110, 220 and 130 crystalline diffraction planes (Figures 3.11a and 3.11b), while the neutron pattern shows amorphous diffraction related to the 200, 111 and 221. Similar to CsCu_2Cl_3 , the amorphous diffraction in molten **1** correlated to the 221 and 111 crystalline diffraction peaks correspond to the $[\text{H}_2\text{NMe}_2]^+ / [\text{Cl}]^-$ pseudo-close-packed layers (Figure 3.12a) and the ordering of the dimethylammonium cations (Figure 3.12b) respectively. The low Q diffraction peak at $\sim 0.78 \text{ \AA}^{-1}$ in the amorphous X-ray pattern is correlated with the 110 crystalline peak of **1** and corresponds to the spacing between the $[\text{Cu}_2\text{Cl}_3]^-$ chains as shown in Figure 3.12c. The amorphous features correlated with the 200 represents a different spacing between the anionic chains (Figure 3.12d) while the 220 is simply a higher order reflection of the 110. As was the case with CsCu_2Cl_3 , this suggests that the copper halide chain must be somewhat preserved in the melt of **1**. Since the FSDP in both structures is correlated to the chain-chain spacing, the structural unit responsible for the IRO must consist of the $[\text{A}]^+ / [\text{Cu}_2\text{Cl}_3]^-$ ion pair. The peak at $\sim 0.78 \text{ \AA}^{-1}$ is lower in Q than the FSDP of CsCu_2Cl_3 ($Q = 0.97 \text{ \AA}^{-1}$) implying the structural unit responsible for the IRO is larger in the melt of **1** than in molten CsCu_2Cl_3 , which is consistent with the larger cation size and unit cell volume in **1**.

The X-ray diffraction of molten $(\text{NMe}_4)\text{Cu}_2\text{Cl}_3$ shown in Figure 3.13, exhibits strong amorphous diffraction, including a low Q peak at 0.94 \AA^{-1} . While the amorphous peaks are less closely correlated with specific crystalline diffraction peaks, however the low Q diffraction peak centered at $\sim 0.94 \text{ \AA}^{-1}$ appears to be correlated to some combination of the

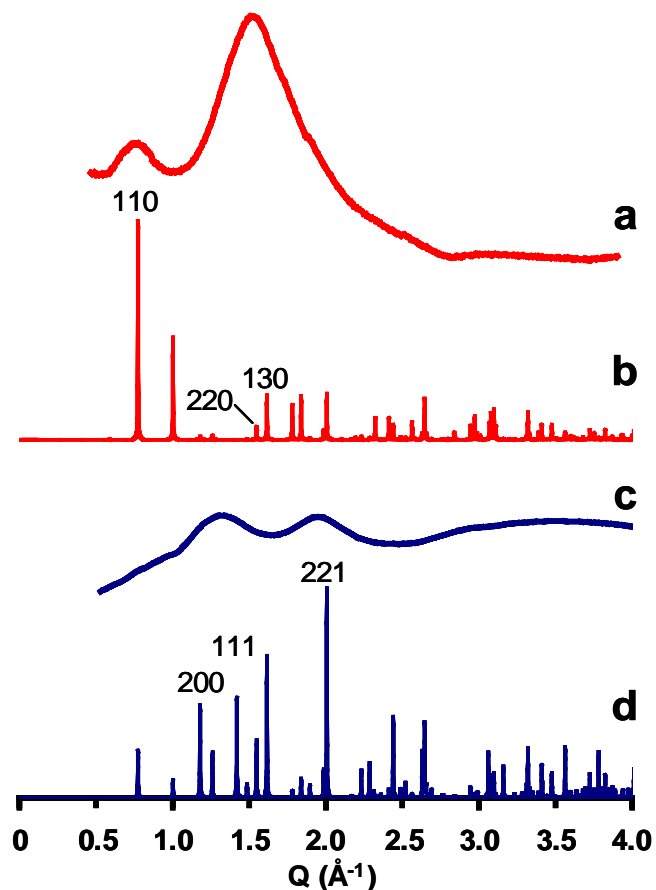


Figure 3.11: X-ray (red) and neutron (blue) diffraction patterns of crystalline and molten **1**. The molten diffraction patterns (a and c) were collected at 150°C while the crystalline diffraction patterns were calculated for the two different radiation sources using the room temperature lattice constants for **1**. The neutron data was collected using a fully deuterated sample, while the X-ray data was collected with a sample of natural isotopic abundance. The amorphous scattering is closely correlated with the labeled crystalline diffraction planes.

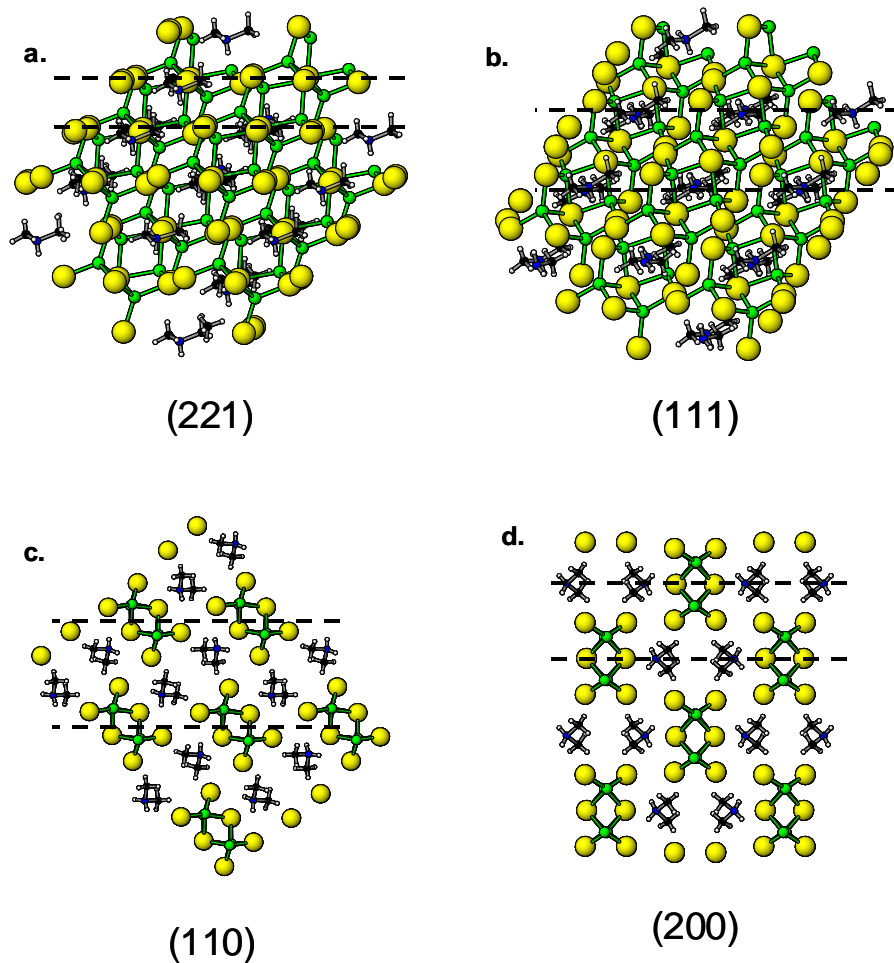


Figure 3.12: The spacings between the crystalline lattice planes correlated to the amorphous diffraction of molten. The spacings between the 111 and 221 of **1** correspond to the separation between close packed layers of $[\text{H}_2\text{NMe}_2]^+ / [\text{Cl}]^-$ and layers of $[\text{H}_2\text{NMe}_2]^+$ cations respectively. The distance between the 110 and 200 planes correspond to the spacing between $[\text{Cu}_2\text{Cl}_3]^-$ chains.

200, 101 and 201. Of these, the 101 is by far the most intense peak in the calculated pattern and might be expected to be the strongest contributor to the amorphous peak at 0.94 \AA^{-1} . The 101 is analogous to the 110 plane in both CsCu_2Cl_3 and **1**, and as shown in Figure 3.14a corresponds to the spacing between chains in $(\text{NMe}_4)\text{Cu}_2\text{Cl}_3$. The 200 diffraction peak in crystalline $(\text{NMe}_4)\text{Cu}_2\text{Cl}_3$ corresponds both to the distance along a which separates the chain centers as well as the distance between layers of the tetramethylammonium template, as pictured in Figure 3.14b.

The diffraction evidence of chain-chain separations in all three molten ACu_2Cl_3 materials suggests that the chain persists into the melt to some extent. Even stronger evidence for retained covalent behavior in these melts is seen by examination of the local order of CsCu_2Cl_3 using PDF analysis. As previously discussed, the nearest neighbor Cu-Cl and Cu-Cu contacts in crystalline CsCu_2Cl_3 are inequivalent due to the covalent interactions within the double chain structure. If random packing of spheres were the only structural influence on molten CsCu_2Cl_3 , the inequivalent bonding contacts would be lost and the atom-atom distances in its melt should be essentially equivalent to those found in molten CuCl and CsCl. Comparison of the PDF analysis for the three melts in Figure 12a clearly shows a local order in CsCu_2Cl_3 that is more complex than the simple combination of CuCl and CsCl. An overlay of the crystalline bond distances with the PDF of CsCu_2Cl_3 (Figure 3.15) shows that the pair correlations in molten CsCu_2Cl_3 instead closely resemble the atom-atom contacts present in crystalline phase. Two distinct Cu-Cl contacts are still observed in molten CsCu_2Cl_3 with a peak centered at 2.26 \AA and the smaller shoulder around 2.45 \AA , which closely compare to the room temperature distances of 2.27 and 2.49 \AA for the $\text{Cu-Cl}_{\mu 2}$ and $\text{Cu-Cl}_{\mu 4}$ bonds respectively. This observation of two different Cu-Cl contacts is further

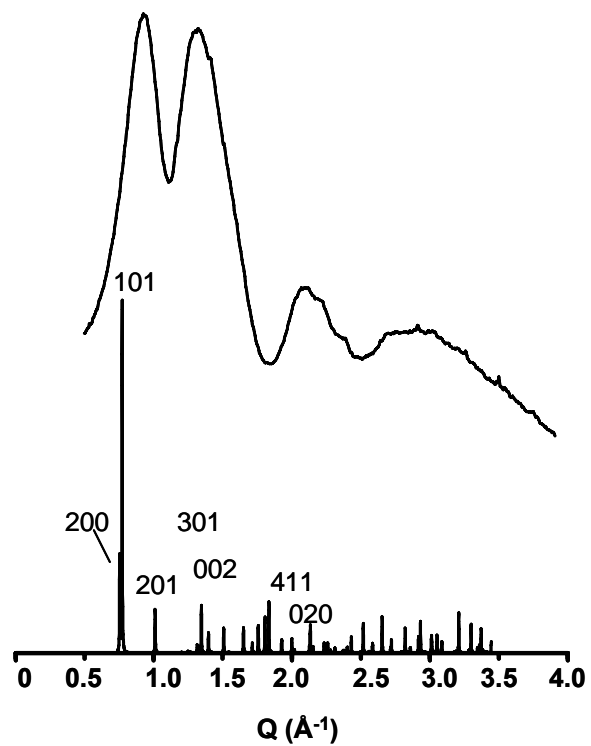


Figure 3.13: Crystalline and melt diffraction patterns of $(\text{NMe}_4)\text{Cu}_2\text{Cl}_3$ collected with X-ray diffraction.

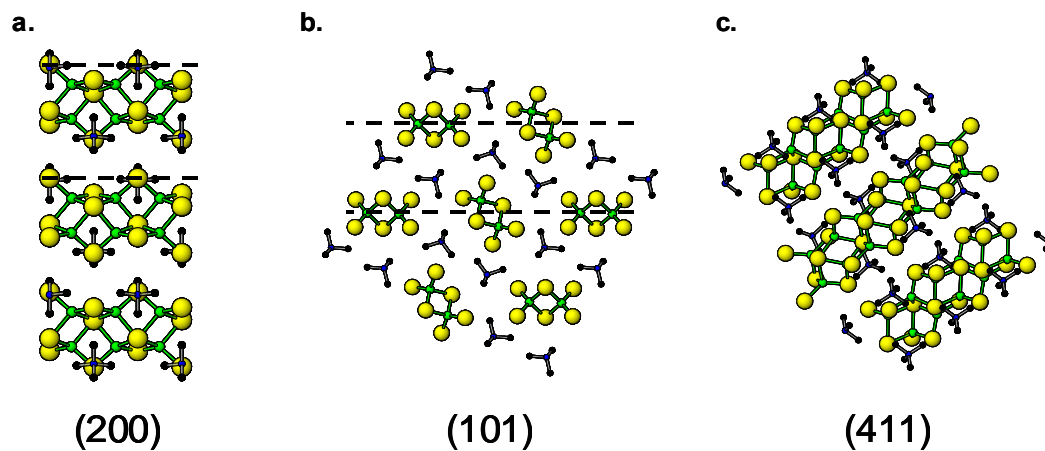


Figure 3.14: The spacings between the crystalline lattice planes correlated to the amorphous diffraction of molten $[\text{NMe}_4]\text{Cu}_2\text{Cl}_3$. The 200 and 101 planes relate to spacings between the $[\text{Cu}_2\text{Cl}_3]^-$ chains.

consistent with published Raman spectroscopy of molten CsCu_2Cl_3 that shows an asymmetric band corresponding to two Cu-Cl stretching frequencies.³⁶ The Cs-Cl and Cl-Cl contacts arising from the pseudo close packing are observed over a range between 3.5-4.5 Å, similar to that of the crystal. Two additional close correlations below 5 Å are present at 2.9 Å and the shoulder around 3.3 Å which we assign to the distinct Cu-Cu contacts perpendicular and parallel to the double chain respectively.

The observation of distinct Cu-Cu pair correlations in molten CsCu_2Cl_3 is in clear contrast to the previously reported lack of Cu-Cu correlations in the PDF of liquid CuCl. This apparent lack of Cu-Cu pair correlations for CuCl has been attributed to disordering of the mobile copper species.¹³ Given that the observation of IRO in amorphous materials has often been attributed to metal-metal correlations,² it can be argued that cation mobility in CuCl is responsible for the lack of a low Q peak ($<2 \text{ \AA}^{-1}$) in the diffraction of its melt. While no conductivity data is available for molten CsCu_2Cl_3 , we note that similar values ($\sim 5 \times 10^{-4} \text{ \Omega}^{-1} \text{ cm}^{-1}$) have been reported for both solid CuCl³⁷ and CsCu_2Cl_3 ²¹ at 500 K, suggesting the possibility of similar $[\text{Cu}]^+$ mobility in the two melts. Yet, we have shown here that molten CsCu_2Cl_3 does exhibit a low Q diffraction peak at 0.97 \AA^{-1} , which argues against the intermediate range order being linked to cation mobility. Further if the $[\text{Cu}]^+$ mobility is similar for both materials, the observation of preservation of the covalently bonded chains in CsCu_2Cl_3 suggests the covalent CuCl network might persist in the melt as well. This work also demonstrates that spacing between structural units, in this case the $[\text{Cu}_2\text{Cl}_3]^-$ chain, might be responsible for diffraction peaks below $Q = 2 \text{ \AA}^{-1}$. Similar structural units may be present in molten CuCl, however, any resulting low Q diffraction peaks are likely systematically absent due to the high symmetry of the CuCl network.

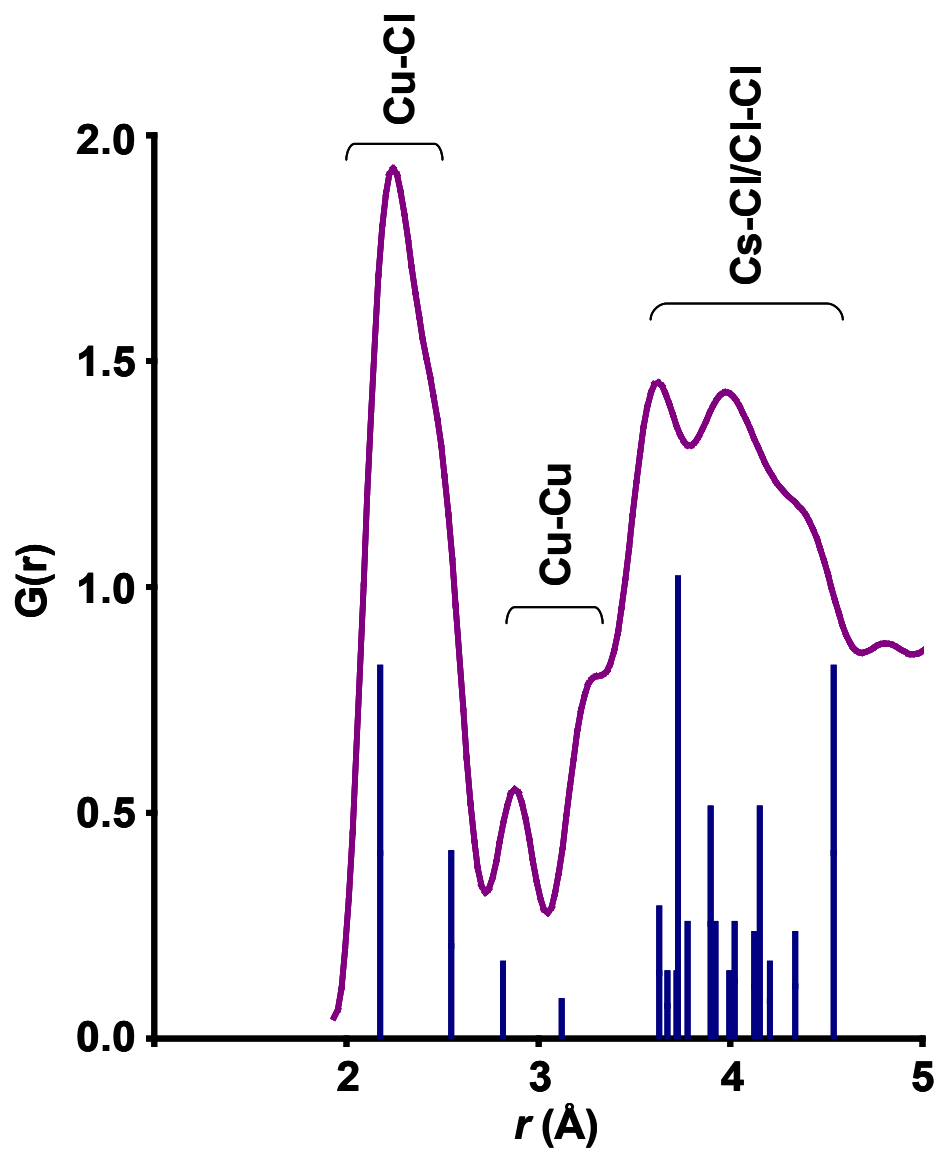


Figure 3.15: Overlay of the pair distribution function $G(r)$ plot of molten CsCu_2Cl_3 and the calculated atom-atom contact distances for the room temperature crystal.

Template Effects on Structure

The crystal packing, and by extension the molten structure, of the $[M_2X_3]^-$ chains in these materials is sensitive to both the size and shape of the templating cation. In most known cases, the site for the $[A]^+$ cation is defined by a rectangular anti-prism formed by 8 chlorides on three neighboring chains; a pair of μ^2 -chlorides from each of two chains which defines one rectangular face and with the second rectangular face defined by two μ^2 -chlorides and two μ^4 -chlorides from the third chain. While the general description of the cation position is common to nearly all of these structures, changing the cation size and shape leads to different packing arrangements of the $[M_2X_3]^-$ and therefore provides a means of manipulating both the crystalline and melt structures of these materials. Note however, that several of the known structures discussed here likely experience decomposition of their organic template prior to melting, particularly when $X = \text{Br}$ or I . Thus to access some geometries it may be necessary to utilize interactions such as hydrogen bonding to decrease melting points.

It is difficult to predict the specific symmetry induced by a given template, but a survey of the known AM_2X_3 compounds offers some understanding of the order imparted by different template types. For instance, several the smallest templates $[\text{Rb}]^+$, $[\text{Cs}]^+$ and $[\text{H}_2\text{NMe}_2]^+$, yield symmetry variants based on close packing of the $[A]^+$ and $[X]^-$ ions. However as shown by the crystal symmetries listed in Table 3.3, variations also exist even in the pseudo close-packed arrangement. While the original structure solutions of the alkali metal templated AM_2X_3 compounds suggested they all adopted the same $Cmcm$ crystal symmetry,³⁸ Hull and Berastegui later demonstrated³⁸ that where the relative size of the cation to the chain is smallest, slight orientational distortions of $0.6\text{-}1.25^\circ$ (see Figure 3.2b) of the

chains relative to the a lattice vector distinguish RbCu_2I_3 and CsAg_2I_3 and lower the crystal symmetry to $Pnma$.²¹ Use of the non-spherical template $[\text{H}_2\text{NMe}_2]^+$ reduces the symmetry in **1** further to the monoclinic space group $P2_1/c$. Orientational distortions also occur when the cation size becomes larger as in the structures where $A =$ tetramethylammonium, trimethylsulfonium or N-methylpyridinium (Figures 3.2c-d). When $A = [\text{NMe}_4]^+$ the chains are rotated dramatically (38° - 47°), while in $(\text{SMe}_3)\text{Cu}_2\text{I}_3$ neighboring chains are no longer symmetrically equivalent. The large changes in orientation seem to occur when the template is large enough to disrupt the close packing arrangement of the cation and halides, but is still smaller than the width of the metal halide chain. In fact, when $(\text{NMe}_4)\text{Cu}_2\text{Cl}_3$ is viewed on the 101 plane as in Figure 3.2c, two templates appear to take up nearly the same area as one $[\text{Cu}_2\text{Cl}_3]^-$ chain, suggesting the structural units responsible for the packing arrangement are the metal halide chain and pairs of $[\text{NMe}_4]^+$ cations. As the template size increases, its shape determines the chain arrangement. Structures with a reasonably symmetrical cation, such as $[\text{NEt}_4]^+$ (Figure 3.2e) have only a slightly lower crystal symmetry than CsCu_2Cl_3 , $Pnma$ rather than $Cmcm$, with the pseudo hexagonal arrangement of cations around each chain. In contrast, hydrogen bonded pairs of 1,1,5,5-tetramethylformazanium cations, shaped like a branched alkyl chain, act as co-packing units with a $[\text{Cu}_2\text{Br}_3]^-$ to give $(\text{Me}_2\text{N}_2\text{CHN}_2\text{Me}_2)\text{Cu}_2\text{Br}_3$ a much lower triclinic symmetry in which the inorganic chains are significantly isolated from the positive charge of the templates as shown in Figure 3.2f.

The spacing between $[\text{A}_2\text{X}_3]^-$ chains is determined by the size of the templating cation and by the identity of the halide. For cations small enough to be contained within the prism defined by the halides of neighboring chains, there exists a relationship between the sum of

the radii of the cation (r_+) and the halide (r_-) and the diagonal distance across the rectangular face of the prism (d) defined by the μ^2 -halides:

$$2(r_+ + r_-) / d \approx 1$$

As shown in Table 3.5, this ratio is nearly 1.0 in every structure where the template can be easily approximated as a sphere. This ratio rule is not directly applicable to compound **1** due to the shape of the dimethylammonium cation and strong hydrogen bonding of the dimethylammonium cation. However, the long dimension of the quadrilateral face of the prism in **1** and the radius of the $[\text{NMe}_4]^+$ cation,³⁹ shows that **1** still roughly follows the rule with an estimated value of 0.90.

A geometric justification of this radius ratio in AM_2X_3 is not readily apparent, rather it seems a somewhat coincidental consequence of the structure. Nevertheless, the radius ratio is helpful in evaluating whether a particular template will yield the AM_2X_3 structure type. For instance, the phase RbCu_2Cl_3 has been reported on some phase diagrams,^{19,40} however it has subsequently been shown to be nonexistent.⁴¹ Instead, the correct RbCl-CuCl phase diagram has two phases near the composition 66% CuCl phase, $\text{Rb}_{18}\text{Cu}_{31}\text{Cl}_{49}$ (63% CuCl) and $\text{Rb}_4\text{Cu}_9\text{Cl}_{13}$ (69% CuCl), suggesting $[\text{Rb}]^+$ is close to being able to form the RbCu_2Cl_3

Table 3.5. Sum of Cation Radius (r_+) and Halide Radius (r_-) Over Diagonal of Prism Face (d) in AM_2X_3

AM_2X_3	$2 (r_+ + r_-) / d$
CsCu ₂ Cl ₃	0.998
CsCu ₂ Br ₃	1.008
CsCu ₂ I ₃	1.018
RbCu ₂ Br ₃	0.992
RbCu ₂ I ₃	1.004
CsAg ₂ I ₃	1.002
(NMe ₄)Cu ₂ Cl ₃	0.994
(NMe ₄)Ag ₂ Br ₃	0.986
(NMe ₄)Ag ₂ I ₃	1.000
(H ₂ NMe ₂)Cu ₂ Cl ₃	0.906

phase.⁴¹ The nonexistence of RbCu_2Cl_3 is predicted by the template/halide radius ratio. Using CsCu_2Cl_3 as a model for the $[\text{Cu}_2\text{Cl}_3]^-$ chain dimensions, a $[\text{Rb}]^+ / [\text{Cl}]^-$ radius ratio of 1.0 would require a $\text{Cl}_{\mu 2} - \text{Cl}_{\mu 2}$ distance of 3.4 Å, which is less than the van der Waals radii of two chloride ions (3.6 Å), preventing formation of the RbCu_2Cl_3 phase. Similarly no ACu_2X_3 phases are known for $\text{A} = [\text{Li}]^+$, $[\text{Na}]^+$ or $[\text{K}]^+$, nor do they form phases near 66% CuX .⁴²

Furthermore, this radius ratio can be used to explain distortions in within the $[\text{M}_2\text{X}_3]^-$ chain occurring when A is a relatively large cation such as $[\text{NMe}_4]^+$, $[\text{NEt}_4]^+$ or $[\text{SMe}_3]^+$. In these compounds, the Cu-Cu distances are longer along the direction of chain propagation than those perpendicular to the chain, which is opposite what is observed for compounds with smaller cations. This is highlighted in Table 3.6 which lists the ‘across-chain’ and ‘down-chain’ Cu-Cu distances for several AM_2X_3 compounds, where the across/down distance ratio is larger than 1 for smaller cations but is less than 1 in $(\text{NMe}_4)\text{Cu}_2\text{Cl}_3$. The diagonal distance of the face of the rectangular anti-prism defined by the four μ^2 halides is determined by the distance between the μ^2 halides within a chain and the separation between the two chains as illustrated in Figure 3.16. The separation between the μ^2 -halides within a chain is approximately equal to twice the Cu-Cu down chain distance. To maintain a template/halide radius ratio of 1.0 in $(\text{NMe}_4)\text{Cu}_2\text{Cl}_3$, with a down chain Cu-Cu distance similar to that in CsCu_2Cl_3 , the spacing between chlorides on neighboring chains would need to be about 10.4 Å. In the actual structure, the $\text{Cl}_{\mu 2} - \text{Cl}_{\mu 2}$ distance within the chain is increased by switching the orientation of the Cu-Cu distances within the chain, such that the long distance is down the chain instead of across it. This allows for a smaller chain-to-chain

distance of 8.6 Å in the true structure and more efficient crystal packing. Similar distortions are also observed in $(\text{SMe}_3)\text{Cu}_2\text{I}_3$, $(\text{MeNC}_5\text{H}_5)\text{Cu}_2\text{I}_3$ and $(\text{NEt}_4)\text{Ag}_2\text{X}_3$ ($\text{X} = \text{Cl}, \text{Br}$).

Finally, $(\text{NMe}_4)\text{Cu}_2\text{I}_3$ provides an examples of a compound of ACu_2X_3 stoichiometry that exists but does not adopt the double chain structure of CsCu_2Cl_3 . Instead $(\text{NMe}_4)\text{Cu}_2\text{I}_3$ consists of a single chains of distorted copper centered tetrahedra with μ^2 and μ^3 iodide positions.⁴³ While the distortion of the Cu-Cu distances in $(\text{NMe}_4)\text{Cu}_2\text{Cl}_3$ allows it to keep a template/halide ratio of 1, a similar distortion in $[\text{Cu}_2\text{I}_3]^-$ a double chain, does not provide enough expansion of the rectangular anti-prism to accommodate tetramethylammonium. The Cu-Cu bond distances in $(\text{NMe}_4)\text{Cu}_2\text{Cl}_3$ of 2.87 and 3.12 Å, are quite similar to the distances in a copper iodide double chain such as in the isosymmetric $(\text{MeNC}_5\text{H}_5)\text{Cu}_2\text{I}_3$ which has Cu-Cu distances of 2.95 and 3.14 Å. Using the same Cu-Cu distances for the $[\text{Cu}_2\text{I}_3]^-$ double chain, to maintain a template/halide ratio of 1 in $(\text{NMe}_4)\text{Cu}_2\text{I}_3$ a $\text{I}_{\mu 2}-\text{I}_{\mu 2}$ distance between neighboring chains of 7.01 Å would be required, as opposed to the distance of 4.79 Å in $(\text{MeNC}_5\text{H}_5)\text{Cu}_2\text{I}_3$, giving a total unit cell volume of $\sim 1700 \text{ \AA}^3$ ($Z = 4$), corresponding to 425 \AA^3 per formula unit. The true structure provides more efficient crystal packing with a volume of 1871 \AA^3 ($Z = 6$), or 312 \AA^3 per formula unit.

Table 3.6. Calculated M-M Distances in AM₂X₃ Structures

Composition	Across Chain Distance (Å)	Down Chain Distance (Å)	Across Chain / Down Chain Ratio
CsCu ₂ Cl ₃	3.119(3)	2.7972(4)	1.115
CsCu ₂ Br ₃	3.079(3)	2.9066(4)	1.059
CsCu ₂ I ₃	3.143(1)	3.0486(2)	1.031
RbCu ₂ Br ₃	3.243(3)	2.776(4)	1.168
RbCu ₂ I ₃	3.414(2)	2.8928(3)	1.180
1 (low temp)	3.0549(6)	2.9090- 2.9100(6)	1.050
(NMe ₄)Cu ₂ Cl ₃	2.869(2)	3.116(2)	0.921
CsAg ₂ I ₃	3.622(2)	3.211(5)	1.128
(NMe ₄)Ag ₂ Br ₃	3.079(2)	3.526(2)	0.873
(NMe ₄)Ag ₂ I ₃ *	3.698-3.739	3.037	1.217

*The errors in atomic positions were not published with the crystal structure solution.

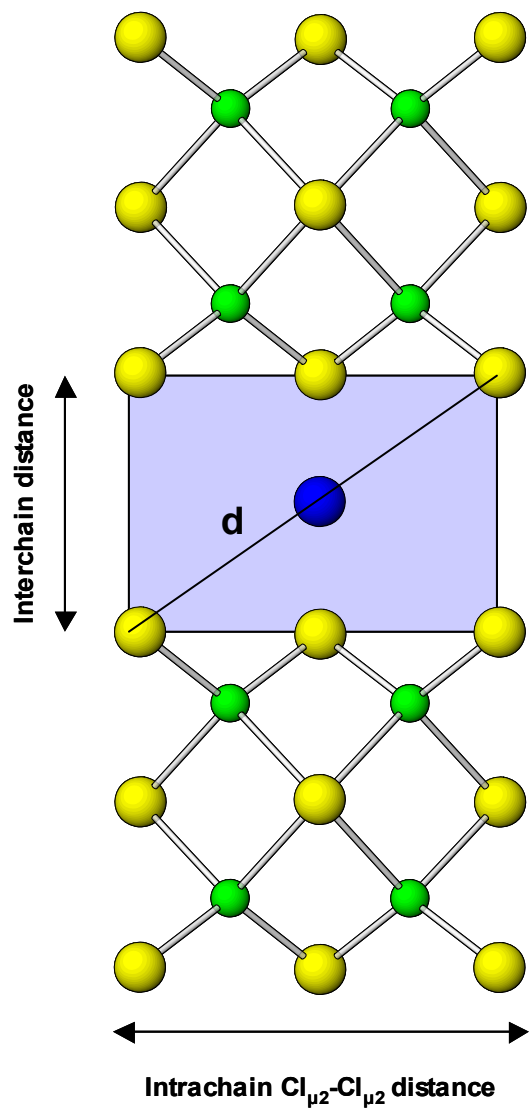


Figure 3.16: The face of the rectangular antiprism, shaded, is defined by the μ_2 -chlorides of two neighboring chains. The diagonal distance across this plane, d , is determined by the distances between the chains and the μ_2 -chlorides of a given chain.

3.3 Conclusions

The symmetry of CuCl can be lowered by chemical modification with an ACl templating salt to give the ACu_2Cl_3 structure, which in the molten state exhibits a first sharp diffraction peak characteristic of intermediate range order. Diffraction and pair distribution function analysis demonstrate that the covalent double chains in crystalline ACu_2Cl_3 remain intact in the molten state. That a lowering the symmetry of copper halide melts gives rise to a low Q diffraction peak is consistent with the idea that molten CuCl itself lacks such a peak due to a systematic absence. Further the preservation of Cu-Cl covalent bonding in a copper chloride melt challenges the original model proposed for molten CuCl suggesting disordering of the $[Cu]^+$ cation due to its high mobility.

The low Q diffraction peaks exhibited by these templated copper halide melts arises from intermediate range order related to the distance between the $[Cu_2X_3]^-$ chains. The anion chains therefore serve as structural units that can be used to design intermediate range order into copper halide melts. By varying the templating cation A, the molten structure can be further manipulated. The AM_2X_3 structure offers a number of known symmetry variants, which increases the possibilities of for intermediate range order design in these melts.

The low melting points of templated copper (I) and silver (I) halides make them excellent candidates for designing melt structure with covalently bonded inorganic structural units. The key to applying this strategy to other systems is to find materials with melting points low enough to avoid dissociation of covalently bonded units. The hydrogen bonding induced ion pairing in $(H_2NMe_2)Cu_2Cl_3$ has been shown to dramatically reduce the melting point of ACu_2Cl_3 giving it the lowest known melting point of this structure type. Even lower melting ACu_2X_3 variants may be discovered through both careful choice of chemical

composition and by intentional design of hydrogen bonding induced ion pairing effects. Designing similar ion pairing effects in other solids may serve as a useful tool to for developing low melting inorganics.

3.4 Experimental

General Procedures.

All manipulations were performed under inert atmosphere in a glove box filled with N₂ gas. Reactions were heated in flame sealed quartz tubes using vacuum and Schlenk line techniques. Copper (I) chloride was prepared from Cu metal and CuCl₂•2H₂O (Aldrich, 97%) according to literature methods.⁴⁴ Copper (I) bromide was purchased from Aldrich and purified by sublimation. Dimethyl amine hydrochloride (Aldrich 99%) was sublimed under vacuum at 140°C. Tetramethyl amine hydrochloride (Aldrich 97%) was purified by dissolution at 60°C in a 50/50 mixture of ethanol and ethyl ether. The hot solution was vacuum filtered and the solid was recrystallized at 0°C and filtered from the remaining solution. The recrystallized tetramethyl amine hydrochloride was then dried under vacuum at 140°C for 24 hours. Ethanol was distilled over CaH₂ and stored over 4Å molecular sieves.

Synthesis

(a) $(H_2N(CH_3)_2)Br$. Dimethyl amine hydrobromide was prepared by combining 4.4 mL of aqueous HBr solution (Aldrich, 48%) and 5.0 mL of aqueous dimethylamine (Aldrich, 40%) . The resulting solution was heated under vacuum to dryness leaving behind an off-white solid. This solid was washed several times with diethyl ether to remove excess Br₂ formed during the reaction. Finally the solid was sublimed under vacuum at 140°C. X-ray

diffraction of the sublimed solid matched the calculated pattern for dimethyl ammonium bromide.⁴⁵

(b) $(N(CH_3)_4)Cu_2Cl_3$. Bulk amounts of $(N(CH_3)_4)Cu_2Cl_3$ were prepared by mixing 0.107 g (0.98 mmol) tetramethylamine hydrochloride and 0.193 g CuCl (1.9 mmol) in a thin-walled silica tube. The tubes were flame sealed under vacuum, heated to 230°C for 24 hours and either slow cooled or quenched to room temperature. Single crystals of $(N(CH_3)_4)Cu_2Cl_3$ were grown for DSC experiments by combining 0.107 g (0.98 mmol) of tetramethylamine hydrochloride and 0.193 g (1.9 mmol) of CuCl in a thick-walled fused silica tube. One milliliter of dry ethanol was added to the tube using Schlenk techniques. The entire mixture was frozen using liquid nitrogen and flame sealed under vacuum. The tube was then heated to 100°C for 150 hours and then slow cooled to room temperature at a rate of 0.1°C/min. This produced several transparent, needle-shaped crystals confirmed to be $(N(CH_3)_4)Cu_2Cl_3$ by X-ray powder diffraction.

(c) $(H_2N(CH_3)_2)Cu_2X_3$. Bulk amounts of the compound **1** were prepared by placing 0.088 g dimethyl amine hydrochloride (1.1 mmol) and 0.212 g CuCl (2.1 mmol) in a thin walled fused silica tube. Bulk amounts of compound **2** were prepared by combining 0.091 g (0.72 mmol) dimethyl amine hydrobromide and 0.209 g (1.5 mmol) CuBr in a fused silica tube. The tubes were flame sealed and heated to 200°C to melt to reactants, then slow cooled at a rate of 0.1°C/min.

(d) $(H_2N(CH_3)_2)Cu_2Cl_{3-y}Br_y$. Mixed halide materials of composition $(H_2N(CH_3)_2)Cu_2Cl_{3-y}Br_y$ were prepared by the method above for compounds **1** and **2** using stoichiometric amounts of CuCl, CuBr, $(H_2N(CH_3)_2)Cl$, and $(H_2N(CH_3)_2)Br$.

X-ray Structure Determination of (H₂N(CH₃)₂)Cu₂Cl₃

A mixture of 0.088 g dimethylammonium chloride, 0.212 g of CuCl was placed into a thick-walled fused-silica tube. One milliliter of ethanol was added to the mixture using Schlenk techniques. The entire mixture was frozen using liquid nitrogen and flame sealed under vacuum. This reaction tube was then heated to 100°C for one week and slow cooled to room temperature at a rate of 0.1°C/min. Several colorless needle-shaped crystals grew from this solution. X-ray powder diffraction of these crystals indicated a single phase material.

A single crystal of **1** was mounted using silicon grease and kept under a constant flow of nitrogen at -128°C. Data were collected using an Enraf-Nonius CAD4-MACH diffractometer with Mo K α radiation. The cell lattice constants were determined by a symmetry constrained fit of 24 well centered reflections from a 2 θ range of 16.50° to 18.00° and their Friedel pairs. Reflections were collected from the entire Ewald sphere with 5979 independent reflections measured by ω scans from 0° < 2 θ < 54°. The data were scaled to three intensity check reflections using a five point smoothing routine. An empirical absorption correction was applied using psi scan data. Systematic absences were consistent with the space group P2₁/c, which was confirmed in the subsequent refinement. All non-hydrogen atoms were found using direct methods with the SIR92 program and hydrogen atoms were located from the difference Fourier map. All non-hydrogen atoms were refined anisotropically. A full matrix least squares calculation on 1678 unique reflections [$I > 1.0\sigma(I)$] were used in the final refinement using the NRCVAX programs. The final R factors obtained were R=0.040 and R_w=0.049.

Neutron Diffraction and PDF analysis.

Total structure factor data were collected on the GLAD diffractometer at the IPNS at Argonne National Laboratory. Data were collected on samples in fused silica ampules at approximately 40°C above the melts of fully deuterated $[D_2NMe_2]Cu_2Cl_3$ and $CsCu_2Cl_3$ as well as temperatures below the melt. These data were corrected with respect to an empty fused silica tube, a vanadium standard and the instrument background. Structure factor and pair distribution functions were calculated using the suite of programs provided by the IPNS-GLAD facility.

Powder X-ray Diffraction.

Variable temperature powder x-ray diffraction experiments were performed at the X7B beamline of the National Synchrotron Light Source at Brookhaven National Laboratory with a wavelength of approximately 1 Å in a Debye-Scherrer collection geometry using a *MAR345* Image Plate Detector system. The wavelength, sample-to-detector distance, tilting angle of the IP, and zero shift position of the IP were calibrated to the LaB_6 standard using the ‘fit2d’ software package to analyze the full Debye-Scherrer rings of the *MAR* data.⁴⁶ The amorphous background due to sample absorption and scattering from the glass capillary was subtracted manually from each solid sample, and the same background subtraction was applied to the melt data.

Room temperature lattice constants were determined using powder x-ray diffraction data collected on an Inel XRG 3000 diffractometer using monochromated $Cu K\alpha_1$ radiation and a CPS 120 detector. The diffractometer was calibrated with 57 peaks in the range of 12-60° 2θ from a potassium alum standard.⁴⁷ Samples of $DmaCu_2X_3$ were loaded into 0.5 mm

borosilicate capillaries which were then flame sealed to protect the sample from moisture. Diffraction data was collected for six hours for each sample. Lattice constants for each sample were refined using the DICVOL91 indexing software.⁴⁸

Differential Scanning Calorimetry.

All melting points were measured using a TA Instruments Q100 differential scanning calorimeter. Borosilicate capillaries of diameter 0.7 mm were used as sample holders because the ACu_2Cl_3 compounds were too reactive towards stainless steel sample pans. Approximately 4 mg of each sample loaded into the borosilicate capillaries inside a glove box. The capillaries were then flame sealed and set on aluminum holders inside the DSC. The reference consisted of an identical aluminum sample holder with an empty sealed capillary.

Acknowledgements

Dr. Jonathan C. Hanson is acknowledged for his support at NSLS Beamline X7B, and Dr. Paul D. Boyle for his assistance in collecting the single crystal data. Dr. Joan Siewiene and Dr. Chris Benmore are also acknowledged for their support at IPNS with the GLAD instrument. This work was supported by the NSF via the contract DMR-0305086. The research carried out at beam line X7b at BNL-NSLS was supported by contract DE-AC02-98CH10086 with the US DOE office of basic energy sciences division of chemical sciences. The NSLS and IPNS are supported by the Divisions of Materials and Chemical Sciences of DOE.

3.5 References

- (1) (a) Apling, A. J.; Leadbetter, A. J.; Wright, A.C. *J. Non-Cryst. Solids* **1977**, *23*, 369-384.
(b) Busse, L. E.; Nagel, S. R. *Phys. Rev. Lett.* **1981**, *47*, 1848-1851. (c) Phillips, J. C. *J. Non-Cryst. Solids* **1981**, *43*, 37-77. (d) Price, D. L.; Moss, S. C.; Reijers, R.; Saboungi, M-L. *J. Phys.: Condens. Matter* **1989**, *1*, 1005-1008.
- (2) Wright, A. C. *Glass Phys. And Chem.* **1998**, *24*, 148-179.
- (3) (a) Elliot, S. R. *J. Phys.: Condens. Matter.* **1992**, *4*, 7761-7678. (b) Badyal, Y. S.; Howe, R. A. *J. Phys.: Condens. Matter*, **1996**, *8*, 3733-3754. (c) Wasse, J. C.; Salmon, P. S. *J. Phys.: Condens. Matter.* **1998**, *10*, 8139-8146.
- (4) Martin, J. D.; Goettler, S. J.; Fossé, N.; Iton, L. *Nature*, **2002**, *419*, 381-384.
- (5) Biggin, S.; Enderby, J. E. *J. Phys. C: Solid St. Phys.*, **1981**, *14*, 3129,3136.
- (6) Desa, J. A. E.; Wright, A. C.; Wong. J.; Sinclair, R. N. *J. Non-Cryst. Solids*, **1982**, *51*, 57-86.
- (7) Angell, C. A.; Wong, J. *J. Non-Cryst. Solids*, **1970**, *73*, 1-17.
- (8) Wilson, M.; Madden, P. A. *Phys. Rev. Lett.* **1998**, *80*, 532-535.
- (9) Polsky, C. H.; Martinez, L. M.; Leinenweber, K.; VerHelst, M. A.; Angell, C. A.; Wolf, G. H. *Phys. Rev.B*, **2000**, *61*, 5934-5938.
- (10) Wilson, M. *J. Chem. Phys.* **2003**, *118*, 9838-9853.
- (11) Wong, J.; Lytle, F. W. *J. Non-Cryst. Solids* **1980**, *37*, 273-284.
- (12) Salmon, P. S.; Martin, R. A.; Mason, P. E.; Gabriel, J. C. *Nature*, **2005**, *435*, 75-78.
- (13) (a) Page, D. I.; Mika. *J. Phys. C: Solid St. Phys.* **1971**, *4*, 3034-3044. (b) Eisenberg, S.; Jal. J.F.; Dupuy; Chieux, P.; Knoll, W. *Phil. Mag. A.* **1982**, *46*, 195-209.

- (14) (a) *Handbook of Chemistry and Physics* **1968** (Cleveland: Chemical Rubber Co.) (b) Boyce, J. B.; Mikkelsen, Jr. J. C. *J. Phys. C* **1977**, *10*, L41-L43.
- (15) Wyckoff, W. G. R.; Posnjak, E. *J. Am. Chem. Soc.* **1922**, *44*, 30-36.
- (16) Subramanian, L.; Hoffmann, R. *Inorg. Chem.* **1992**, *31*, 1021-1029.
- (17) Andersson, S.; Jagner, S. *Acta. Chem. Scand. A* **1985**, *40*, 177-181.
- (18) Brink, C.; Binnendijk, N. F.; van de Linde, J. *Acta Cryst.* **1954**, *7*, 176-180
- (19) Yamato, O., in *Fast Ion Transport In Solids*; B. Scosati *et. al.* Eds.; Kluwer Academic Pub.; Netherlands, 203-211 (1993).
- (20) Lescano, G. M.; de Rapp, M. E. F.; Schmidt, J. A.; de Reza, N. W. *Materials Lett.* **2000**, *45*, 269-272.
- (21) Hull, S.; Berastegui, P. *J. Solid State Chem.* **2004**, *177*, 3156-3173.
- (22) Wojakowska, A.; Krzyżak, E.; Wojakowski, A. *Thermochimica Acta* **2000**, *344*, 55-59.
- (23) Wojakowska, A.; Krzyżak, E.; Wojakowski, A. *J. Thermal Analysis and Calorimetry* **2001**, *65*, 491-495.
- (24) Boehm, J. R.; Balch, A. L.; Bizot, K. F.; Enemark, J. H. *J. Am. Chem. Soc.* **1975**, *97*, 501-508.
- (25) Wojakowska, A.; Górniak, A.; Kuznetsov, A. Y.; Wojakowski, A.; Josiak, J. *J. Chem. Eng. Data* **2003**, *48*, 468-71.
- (26) Asplund, M.; Jagner, S.; Nilsson, M. *Acta Chem. Scand., A* **1985**, *39*, 447-451.
- (27) Hartl, H.; Mahdjour-Hassan-Abadi, F. *Naturforsch. Teil B.* **1984**, *39*, 149-156.
- (28) Geller, S.; Gaines, J. M. *J. Solid State Chem.* **1985**, *59*, 116-122.
- (29) Helgesson, G.; Jagner, S. *Acta Cryst., C* **1988**, *44*, 2059-2062.
- (30) Jagner, S.; Olsen, S.; Stomberg, R. *Acta Chem. Scand., Ser. A.* **1986**, *40*, 230-2.

- (31) Pettigrosso, R. S.; Bazán, J. C.; de Rapp, M. E. F. *Materials Letters* **1996**, *29*, 81-85.
- (32) Meyer, H. J. *Acta Cryst.* **1963**, *16*, 788-792.
- (33) Geller, S.; Ray, A. K.; Nag K. *J. Solid State Chem.* **1983**, *48*, 176-188.
- (34) Frydrych, R.; Muschter, T.; Brüdgam, I.; Hartl, H. *Z. Naturfor. Teil B*, **1990**, *45*, 679-688.
- (35) Locke, J.; Messoloras, S.; Stewart, R. J.; McGreevy, R. L.; Mitchell, E. W. J. *Phil. Mag. B.* **1985**, *53*, 301-315.
- (36) Gilbert, B.; Fung, K. W.; Mamantov, G.; Begun, G. M. *J. Inorg. Nucl. Chem.* **1975**, *37*, 921-927.
- (37) Wagner, J. B.; Wagner C. *J. Chem. Phys.* **1957**, *26*, 1597-1601.
- (38) Bigalke, K. P.; Hans, A.; Hartl, H. *Z. Anorg. Allg. Chem.* **1988**, *563*, 96-104.
- (39) Masterton, W. L.; Bolocofsky, D.; Lee, T. P. *J. Phys. Chem.* **1971**, *75*, 2809-2815.
- (40) Kanno, R.; Takeda, Y.; Masuyama, Y.; Yamamoto, O. *Solid State Ion.* **1983**, *11*, 221-226.
- (41) (a) Geller, S.; Sishen, X. *J. Solid State Chem.* **1986**, *63*, 316-325. (b) Sishen, X., Geller, S. *J. Solid State Chem.* **1986**, *63*, 326-335.
- (42) Wojakowska, A. *J. Thermal Anal.* **1996**, *46*, 369-376.
- (43) Andersson, S.; Jagner, S. *Acta Chem. Scan. A* **1985**, *39*, 181-186.
- (44) Kauffman, G. B.; Fang, L. Y. *Inorg. Synth.* **1983**, *22*, 101.
- (45) Jones, P. G.; Fischer, A. K.; Vogt, H. *Z. Kristallog.* **1994**, *209*, 834.
- (46) (a) Hammersley, A. P. *FIT2D: An Introduction and Overview*; ESRF Internal Report, ESRF97HA02T; European Synchrotron Radiation Facility: Grenoble Cedex, France, 1997.

(b) Hammersley, A. P. *FIT2D V9.129 Reference Manual V3.1*; ESRF Internal Report, ESRF98HA01T; European Synchrotron Radiation Facility: Grenoble Cedex, France, 1998.

(47) Larson, A. C.; Cromer D. T. *Acta Cryst.* **1967**, *22*, 793.

(48) (a) Louer, D.; Louer, M. *J. Appl. Cryst.* **1972**, *5*, 271-275. (b) Boultif, A.; Louer, D. *J. Appl. Cryst.* **1991**, *24*, 987-993.

Chapter 4:
Kinetics of the Lattice Reconstructions in CuAlCl_4
Induced by Small Molecule Binding.

Abstract

The ethylene gas sorption reactions of α -CuAlCl₄ have been studied by TGA/DSC and optical microscopy at 35°C to probe the mechanisms of the lattice rearrangements which give rise to (Et)_xCuAlCl₄ adducts. On exposure to partial pressures of ethylene below 30 Torr, CuAlCl₄ is converted to a liquid one-equivalent phase, **et-1**. The effect of CuAlCl₄ on the reaction rate demonstrates that formation of **et-1** occurs via two competing kinetic processes, whereby initial rapid reaction at the particle surface is followed by a slower rate of gas sorption to penetrate deeper into the CuAlCl₄ particles. On exposure to higher ethylene pressures **et-1** goes on to form crystalline (C₂H₄)₂CuAlCl₄, **et-2**. The rate of crystallization of **et-2** is shown to be linearly dependent on pressure, suggesting an associative reaction mechanism. By applying a Sharp-Hancock analysis to the kinetic data, these reactions are shown to follow acceleratory phase boundary controlled reaction kinetics as described by the Avrami-Erofe'ev model. The kinetic data is discussed in terms of the previously described sorptive reconstruction mechanism proposed for the solid-state gas sorption reactions of CuAlCl₄.

4.1 Introduction

An increasing number of crystalline materials are being reported which reversibly bind small molecules through dynamic solid-solid phase transitions and lattice expansions, notably metal-organic framework materials (MOFs).¹ These types of reactions are hoped to provide the technology for next generation gas storage and sensing materials.² In spite of their importance, the molecular-scale interactions involved in these and other heterogeneous gas-solid reactions are frequently not well understood. Some mechanistic information is available for decomposition of condensed solids involving the desorption guest species, particularly dehydration reactions,³ however, descriptions for gas sorption by bulk crystalline compounds is largely limited to reactions with either porous sorbates or those limited to surface binding.⁴ While binary copper halides have been reported undergo solid-state reaction with ethylene at pressures of 60 atmospheres⁵ and with CO from 3-100 atmospheres depending on particle size,⁶ we have shown that CuCl network materials formed with a common ion Lewis acid (AlCl₃, GaCl₃ or ZrCl₄) undergo dramatic reconstructive solid-state reactions on exposure to an atmosphere or less of gas.^{7,8,9} The structures of the CO and ethylene adduct phases of CuMCl₄ (M = Al, Ga) suggest an inversion of configuration of the copper centered tetrahedra occur on gas sorption. Based on this observation, we have proposed a mechanistic model for this process, referred to as sorptive reconstruction, whereby S_n2-type attack on copper by CO or ethylene leads to uptake of up to 2 molar equivalents of gas to yield crystalline adduct phases.^{7,9} The structure of CuMCl₄ (M = Al, Ga) possess sets of van der Waals channels,¹⁰ which are too small to accommodate guest molecules, but seem to direct the lattice reconstruction through the material. In an attempt to test the validity of the proposed sorptive reconstruction mechanism and to increase our

overall understanding of the reactivity of CuAlCl_4 we have examined the kinetics of these reactions. Specifically these kinetic measurements probe the ethylene pressure and particle size dependence and the dimensionality of the gas/solid reaction between CuAlCl_4 and ethylene.

4.2 Background

Review of CuMCl_4 Sorptive Chemistry

Sorption isotherms have shown that CuAlCl_4 forms 1- and 2- equivalent ethylene adduct phases at ethylene pressures less than one atmosphere in the solid state. At initial exposure pressures below 50 Torr of ethylene $\alpha\text{-CuAlCl}_4$ forms either $\alpha\text{-(C}_2\text{H}_4\text{)CuAlCl}_4$, **$\alpha\text{-et-1}$** , or $\beta\text{-(C}_2\text{H}_4\text{)CuAlCl}_4$, **$\beta\text{-et-1}$** . Although the specific conditions giving rise to the α and β phases are not completely elucidated, it appears that trace amounts of moisture catalyzes the nucleation of **$\beta\text{-et-1}$** . Once formed, the one equivalent phases can bind a second equivalent of ethylene to form crystalline $(\text{C}_2\text{H}_4)_2\text{CuAlCl}_4$, **et-2** . This addition of a second equivalent of ethylene is completed at a pressure of approximately 1 atmosphere for **$\beta\text{-et-1}$** or 4 atmospheres for **$\alpha\text{-et-1}$** . Evidence was also seen for a third reaction pathway to directly form **et-2** from $\alpha\text{-CuAlCl}_4$ on initial exposure pressures of 200 Torr or greater of ethylene. Pressure resolved synchrotron diffraction experiments at 15°C indicate that the reacting material remains crystalline throughout the entire structural transformation. The adducts exhibit low melting points (approximately 40°C) and if the temperature is increased above 65°C desorption of the gas occurs to yield $\alpha\text{-CuAlCl}_4$. Desorption isotherms show that ethylene is not lost from **et-2** until pressures below 75 Torr of gas. Desorption from either one-equivalent adduct does not occur until pressures below 10 Torr are achieved. The major

hysteresis observed for sorption and desorption is indicative of a significant kinetic barrier to the lattice reconstruction consistent with a chemisorption reaction. Literature reports of CuCl gas sorption reactions with ethylene and CO show a similar hysteresis and kinetic barrier to reaction.^{6c,11} The CuAlCl₄-CO reaction system is more complex, with the possibility of three 1-equivalent reaction products: α -(CO)CuAlCl₄ (**α -CO-1**), β -(CO)CuAlCl₄ (**β -CO-1**) or (CO)CuCl formed by a moisture catalyzed decomposition. At room temperature and one atmosphere of CO the reaction giving **α -CO-1** proceeds with concurrent formation of a eutectic melt of adduct phases which goes on to yield (CO)₂CuAlCl₄, **CO-2**, at higher pressure. By contrast, **β -CO-1** forms in completion before going on to form the 2-equivalent CO adduct. On decreasing pressure CO pressure **CO-2** begins to lose gas below 700 Torr, while the one-equivalent CO adduct phases is stable until pressures below about 350 Torr are reached.

The crystal structures solved for **β -et-1**, **et-2** and **β -CO-1** as well model structures (based on powder diffraction) for the remaining adducts are built from metal chloride chains with either C₂H₄ or CO ligands bound to copper. The one-equivalent adducts consist of ladder chains with CuAlCl₄ rungs, linked by alternating copper and aluminum tetrahedra. The chains run parallel to each other in the β phases, while the model structure for **α -et-1** suggests sets of perpendicular chains. To account for the considerable gas sorption into α -CuAlCl₄, a non-porous solid, we previously proposed a mechanism whereby sorption of C₂H₄ or CO at the entry point of a van der Waals channel on the crystal surface induces a dramatic lattice reconstruction to yield each adduct phase. The driving force for this sorptive reconstruction mechanism is nucleophilic S_n2 attack by the reactive gas on copper at the surface of a particle. The initial nucleation event expands the crystalline lattice at the

surface, allowing additional nucleophilic attack deeper into the lattice. The reaction would then propagate in this fashion directed by different sets of van der Waals channels in the CuAlCl_4 lattice. This process excises chains from the $\alpha\text{-CuAlCl}_4$ network, resulting in the 1-D chain structures of each of the adduct phases. The α adduct phases can be formed by reaction directed down the perpendicular set of tetragonal channels in $\alpha\text{-CuAlCl}_4$, while the β adduct phases may form by reaction directed by the channels formed by the close packed layers of chlorides. The structure of **et-2** can be readily formed by a second nucleophilic attack on copper, ‘unzipping’ each double chain to give a pair of single chains with two C_2H_4 ligands bound to each copper. The sorption isotherms also show evidence of a pathway giving direct formation of **et-2** from $\alpha\text{-CuAlCl}_4$. This direct $\alpha\text{-CuAlCl}_4 \rightarrow \text{et-2}$ reaction, observed only at higher ethylene pressure, is distinct from the stepwise pathway going through the $\alpha\text{-1-et}$ or $\beta\text{-1-et}$ intermediates.

Kinetics of Solid Phase Transitions.

Examination of structure has provided much insight into the nature of these solid/gas reactions. However, detailed kinetic measurements are required to more rigorously decipher the reaction mechanism. The kinetics of solid-state reactions are limited either by the rate of diffusion of a reactant through the crystalline lattice or by the rate of the propagation of the phase boundary between the reactant and product phases.¹² Phase boundary controlled phase transitions are typically analyzed using the model proposed by Avrami¹³ and Erofe'ev¹⁴ with the rate law given in equation 1 below:

$$[\ln(1-\alpha)]^{1/n} = kt \quad (1)$$

In this expression α is the fraction of the reactant phase transformed ($\alpha = 0$ prior to reaction and 1 at its completion), n is the dimensionality of growth (1, 2 or 3), t is the time in seconds and k is the rate constant for the reaction. This model assumes the random formation of “germ nuclei” of the new phase in a single crystal or grain of the parent material, which creates a phase boundary between the materials. Growth of the product phase occurs as the phase boundary spreads outward from the nucleation site in 1, 2 or 3 dimensions consuming the reactant phase. As the reaction proceeds, growth regions may impinge upon one another or reach the edge of a grain boundary, which will result in termination of growth. Phase boundary controlled reactions are characterized by four regions of their α vs. t plot: (i) an induction period (typically in the range $0 < \alpha < 0.15$), (ii) the acceleratory region ($0.15 < \alpha < 0.5$), (iii) the deceleratory region ($0.5 < \alpha < 1$) and (iv) termination ($\alpha \approx 1$). The induction period tends to be dominated by nucleation and the deceleratory region often shows deviation from the Avrami-Erofe'ev model when applied to a powder due to termination effects. The acceleratory region tends to be dominated by growth of the phase boundary and therefore provides the best fit to eq 1.

Many other solid-state rate expressions are known, including rate laws corresponding to diffusion-controlled growth and phase boundary controlled reactions that are deceleratory throughout the reaction. Nucleation and termination effects are difficult to study and model, and therefore kinetic data often deviates from the solid-state rate expressions in the early and late stages of the reaction, making it difficult to fit data to a particular rate law. However, Sharp and Hancock demonstrated that a plot of $\ln [-\ln (1-\alpha)]$ vs. $\ln (t)$ is linear over the acceleratory portion of a reaction ($0.15 < \alpha < 0.5$) for diffusion controlled or phase boundary

controlled reactions. By plotting equation 2 for only the acceleratory period of a reaction, deviations from the solid-state rate laws arising from nucleation effects during the induction period and termination effects late in the reaction are avoided. The slope of linear portion the Sharp-Hancock plot in eq. 2 can then be used to determine the group of rate laws, phase boundary or diffusion controlled, is followed by the reaction.¹⁵

$$\ln [-\ln(1-\alpha)] = n \ln(t) + b \quad (2)$$

For acceleratory phase boundary controlled reactions, the slope of the Sharp-Hancock plot is equivalent to the value n in eq. 1 corresponding to the dimensionality of the reaction. If the Sharp-Hancock plot gives $n < 1$ then a diffusion controlled mechanism is operative, while deceleratory phase boundary controlled reactions have slopes nearly equal to 1. For acceleratory phase boundary controlled reactions, experimental values of n are generally not whole numbers as suggested by the Avrami-Erofe'ev model and instead may be expressed as:

$$n = \lambda + \beta \quad (3)$$

where λ is the dimensionality of growth (1, 2, or 3) and β represents a contribution to the reaction rate due to nucleation, and normally varies from 0 to 1 ($\beta = 0$ for fast nucleation occurring only during the induction period, $\beta = 1$ for a slow constant rate of nucleation occurring throughout the reaction).^{13b} Therefore, values of n between 1 and 2 are observed for one-dimensional growth, $2 < n < 3$ for two-dimensional growth, and $3 < n < 4$ for three

dimensional growth.¹² The y-intercept of the Sharp-Hancock plot for a phase boundary controlled reaction gives rate constant for the reaction according to equation 4:

$$b = n \ln(k) \quad (4)$$

Some reactions exhibit values of β greater than one, resulting in a Sharp-Hancock much larger than expected based on the dimensionality of the process. While this part of the exponent n is not well defined, autocatalysis, the process by which the generation of germ nuclei is catalyzed by product formation, can be one component which leads to values of β larger than 1. The physical origin of autocatalysis may be attributed to some process such as branching or particle cracking during the reaction, which exposes fresh reactant surface and provides new nucleation sites. Due to the possibility of autocatalysis and values of $\beta > 1$, n does not necessarily correspond directly to a reaction's growth dimensionality. Therefore, unless autocatalysis can be unequivocally ruled out of a reaction mechanism, n only represents the *maximum* growth dimensionality of a phase transformation. It should also be noted that experimental values of n (and to a lesser extent the extracted rate constants) are sensitive to the precise determination of the start of the reaction, t_0 . Therefore, care should be exercised in applying the Sharp-Hancock analysis to experiments where t_0 for a process is not well defined.

For this work the kinetics of the ethylene and CO gas sorption reactions of CuAlCl_4 have been studied and are discussed in relation to the Avrami-Erofe'ev and Prout-Thompkins models. The effects of varying pressure and CuAlCl_4 particle size on the reaction kinetics are examined for the sorption of ethylene. The mechanisms of the low and high pressure

ethylene sorption reactions are discussed in light of the pressure and particle size dependence. The kinetic data presented here support the previously proposed sorptive reconstruction mechanism for gas sorption into the CuAlCl_4 crystalline lattice.

4.3 Results

Measurement of CuAlCl_4 Gas Sorption Kinetics

A number of potential methods were considered for measuring the kinetics of the CuAlCl_4 gas sorption reactions. To properly study the reaction kinetics, isothermal and isobaric conditions are required. An ideal technique for studying the reaction kinetics would allow kinetics experiments under different sets of isothermal and isobaric reaction conditions. In the previous investigations, the progress of these reactions was monitored by UV/Vis-spectroscopy, powder X-ray diffraction and barometric sorption isotherms.^{7,8} In the UV/Vis spectroscopy and X-ray diffraction experiments the reactive gas diffuses through a sample of CuAlCl_4 such that the entire sample is not exposed to the same gas pressure simultaneously, making these techniques unsuitable for measuring kinetics. In the barometric sorption experiments, which are performed in a stainless steel gas line with a known volume, well dispersed CuAlCl_4 samples are exposed to a specific reactive gas pressure providing uniform exposure of the sample. Since the progress of the reaction is calculated from changes in the pressure after the sample is exposed to the reactive gas, this technique does not provide isobaric conditions. However, the sample container of the gas line can be heated or cooled externally to allow for kinetic measurements at different temperatures.

A thermal gravimetric analysis (TGA) instrument was eventually chosen to measure the kinetics in this study. The nitrogen carrier gas of the TGA can be combined with either

ethylene or CO to provide a reactive atmosphere for solid samples of CuAlCl_4 . Further, by measuring the individual flow rates of each gas the specific partial pressures of reactive gas in the mixture can be calculated and controlled. Pressures from 0 Torr (pure N_2) up to 760 Torr (pure ethylene or CO) can be obtained by this method, although it was not possible to accurately measure the partial pressure of gas below 30 Torr with the available flow meters. The particular instrument used for these studies offers the additional benefit of collecting gravimetric and calorimetry data simultaneously, providing a method for studying both kinetics and thermodynamics in a single experiment. However, the draw back to this TGA is its poor temperature control near room temperature and the lowest operating temperature is 35°C .

CuAlCl_4 + Et TGA/DSC Experiments.

The kinetics of ethylene sorption were measured using the microbalance of a TA instruments TGA/DSC at ambient isothermal temperature. In a nitrogen filled glove box, approximately 10 mg of agate mortar and pestle ground samples of $\alpha\text{-CuAlCl}_4$ were placed in a ceramic sample cup of the TGA/DSC. Using a reactive gas manifold a predetermined partial pressure of ethylene was introduced into the nitrogen carrier gas stream. The TGA and DSC data were collected simultaneously during the experiment. Desorption reactions were achieved by shutting off the reactive gas flow leaving a stream consisting of only N_2 . In order to achieve exclusive formation of **et-1** CuAlCl_4 samples were exposed to ethylene partial pressures below 30 Torr. Figure 4.1 shows data for a typical TGA/DSC experiment of $\alpha\text{-CuAlCl}_4$ exposed to an ethylene partial pressure of less than 30 Torr. The TGA shows a two-step weight gain starting with a rapid near linear molar uptake in the first 3 minutes of

the reaction during which up to 0.4 equivalents of ethylene are sorbed. This first step is followed by a more gradual increase that plateaus at a mass corresponding to 1 equivalent of ethylene sorbed. The time required to reach completion varied from 30-120 minutes with different samples, however most samples achieved 95% completion within the first 75 minutes after exposure to ethylene. The fluctuation in reaction time is likely attributable to variations in the reactive gas partial pressure since it could not be accurately controlled at low concentrations. The DSC data corresponding to the weight gain shows a rapid initial exothermic heat flow peak followed by a tail as the reaction slowly approached completion. The total integrated area of the peak and tail in the DSC averaged for 20 experiments was -77 ± 6 kJ/mol of Cu.

After equilibrium was reached at 30 Torr, the ethylene partial pressure in the purge gas was increased to above 50 Torr resulting in the transformation of **et-1** to **et-2**. The ethylene partial pressure was varied from 75 to 700 Torr for different experiments to determine the pressure dependence of this reaction. The data shown in Figure 4.1 shows a representative experiment for an ethylene partial pressure of 700 Torr. A second rapid weight gain is observed until a second plateau is reached corresponding to an additional 0.81 equivalents of ethylene sorbed. Note that this is consistent with the step-wise **et-1** to **et-2** sorption isotherms previously reported, where at one atmosphere of ethylene 1.75 equivalents of gas is sorbed by CuAlCl₄. A corresponding sharp exothermic peak in the DSC accompanies the weight gain with an integrated area averaged over 20 experiments of -173 ± 7 kJ/mol of Cu. After no further weight gain was observed in the TGA the purge gas was switched to pure N₂ (partial pressure of Et = 0). A weight loss ensued over the following fifteen minutes in which the majority of the ethylene was desorbed, leaving approximately

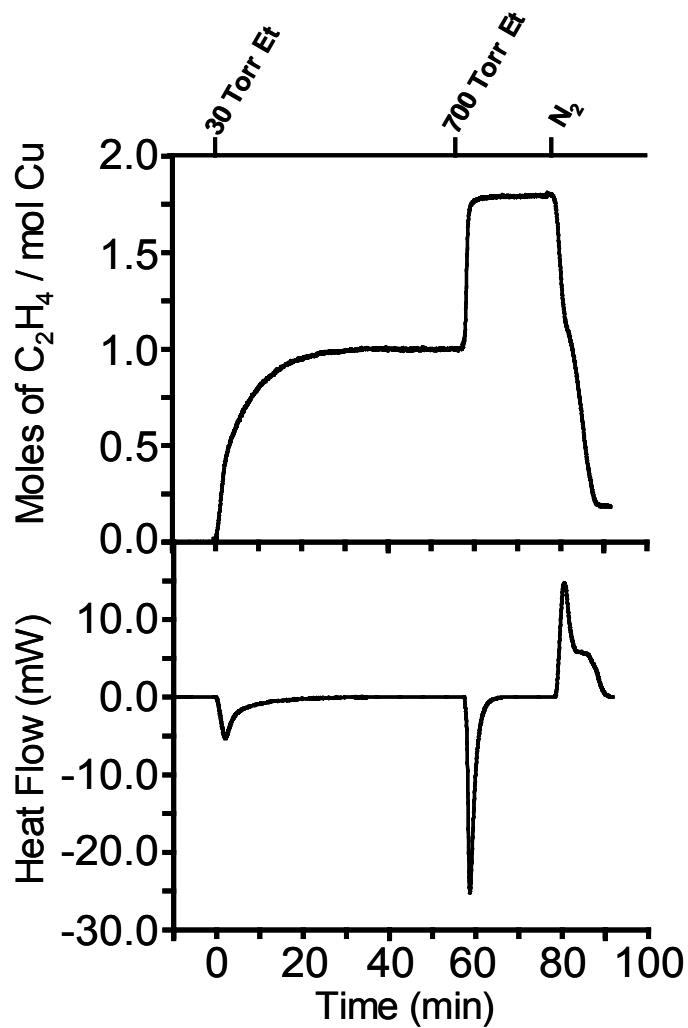


Figure 4.1. Representative TGA/DSC data for the stepwise reaction of CuAlCl_4 with ethylene. After exposure to an initial ethylene partial pressure of <30 Torr the sample rapidly binds ~0.4-0.5 equivalents of gas followed by additional slower absorption to reach the one equivalent phase **et-1**. Subsequent exposure to an ethylene pressure of 700 Torr, causes the sample to quickly bind an additional 0.8 equivalents of gas to yield **et-2**.

0.2 equivalents bound. An inflection in the weight-loss curve is observed at approximately halfway through the desorption, consistent with the microscopic reversibility of this step-wise reaction. Very gradual weight loss follows the rapid desorption. The experiments were terminated shortly after the majority of the desorption had completed. Heating the sample to above 90°C in one experiment resulted in desorption of all of the bound ethylene. The overlapping endothermic features in the DSC correspond to the two-step desorption process, with a total energy of -251 ± 8 kJ/mol of Cu averaged for all experiments.

To test the possibility of a reaction pathway resulting in direct conversion of α -CuAlCl₄ to **et-2**, samples were exposed to initial partial pressures of ethylene of 50 to 760 Torr. A representative experiment beginning with finely ground α -CuAlCl₄ and an ethylene partial pressure of 380 Torr is shown in Figure 4.2a. Over the first 90 seconds of reaction a rapid weight gain occurs, followed by an inflection after sorption of 0.4 equivalents of ethylene. Figure 4.3 highlights the early stages of this reaction for ethylene partial pressures from 100-760 Torr. In all cases for the inflection in the TGA curve at occurs at approximately 0.4 equivalents. With the exception of the 100 Torr experiment, the sorption of the first 0.4 equivalents of ethylene occurs in the same amount of time for each pressure, however the rate of sorption after the inflection increases with increasing ethylene partial pressure. The inflection is followed by a second rapid weight gain that slows as the reaction approaches completion near 1.9 equivalents of ethylene (Figure 4.2a). The majority of the weight gain occurs in the first 30 minutes after exposure to ethylene. The weight gain is accompanied by two overlapping exothermic DSC peaks, shown in Figure 4.2a, with a total energy averaged for all experiments of -281 ± 11 kJ/mol of Cu. Rapid weight loss occurs

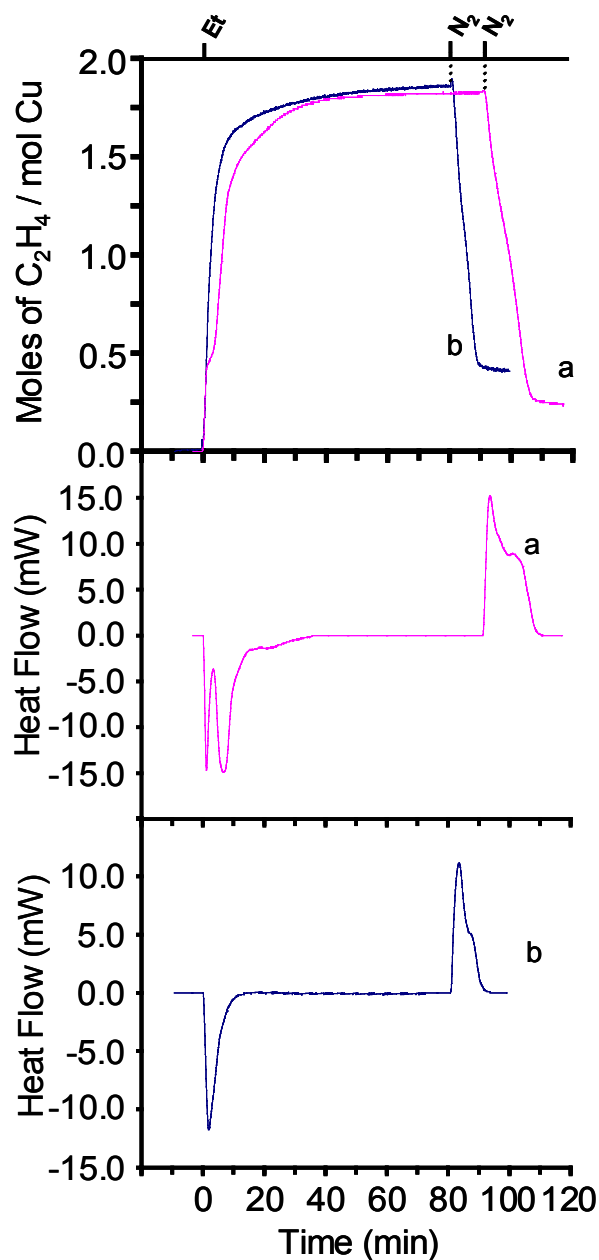


Figure 4.2. Representative TGA/DSC data for $CuAlCl_4$ exposed to an initial ethylene partial pressure greater than 50 Torr. (a) Reaction of agate mortar and pestle ground $CuAlCl_4$ on exposure to 380 Torr of ethylene. (b) Reaction of $CuAlCl_4$ particles sieved to a diameter of 0.2-0.3mm to an ethylene partial pressure of 80 Torr.

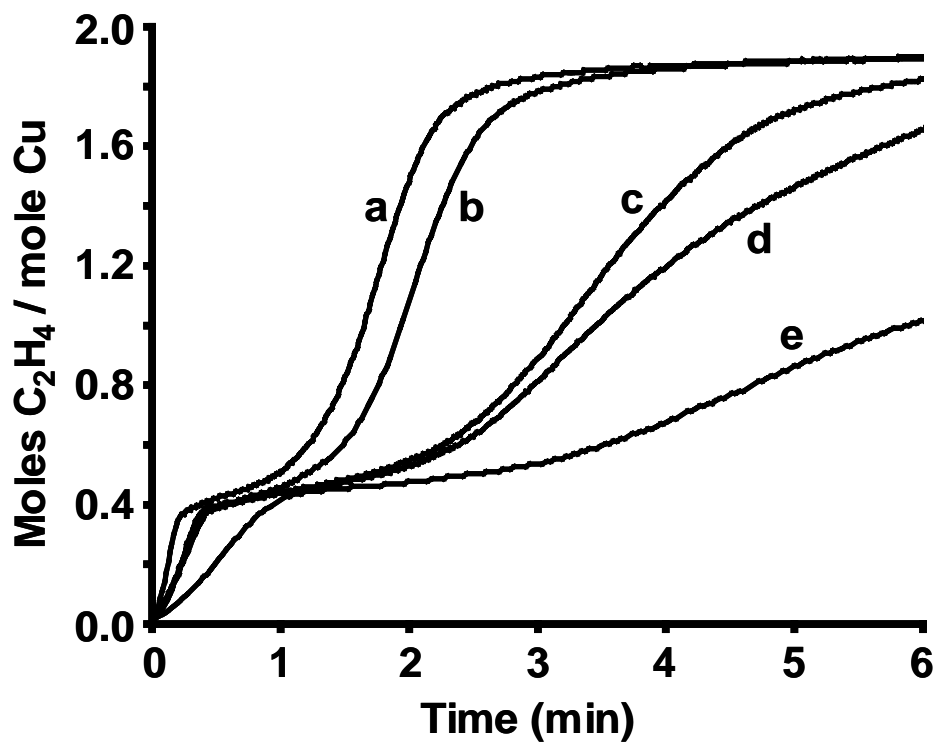


Figure 4.3. The early stages for the high pressure ethylene reaction with CuAlCl_4 at ethylene partial pressures of a) 760 Torr, b) 570 Torr, c) 380 Torr, d) 280 Torr, and e) 90 Torr. At every pressure studied an inflection in the TGA curve occurs at a weight gain corresponding to 0.4 equivalents of ethylene sorbed.

after switching the carrier gas to pure N₂ giving a desorption curve very similar to the one shown in Figure 1 for the step-wise experiment.

Particle Size Effect on Ethylene Gas Sorption

Experiments were also conducted to examine the particle size dependence of ethylene sorption by CuAlCl₄. The gravimetric data vary somewhat when larger particles of α -CuAlCl₄ are exposed to ethylene instead of a fine powder. An overlay of TGA data for reaction of α -CuAlCl₄ of different particle sizes with less than 30 Torr of ethylene is shown in Figure 4.4. The data shown are for samples of α -CuAlCl₄ consisting of an agate mortar and pestle ground fine powder, particles sieved to a diameter of either 0.2-0.3mm or 0.4-0.5mm, and a single solid chunk of α -CuAlCl₄ (7.5 mg). The sorption onset is sharpest for the fine α -CuAlCl₄ particles, and the total time required for each sample to completely bind one-equivalent of ethylene increases with increasing size of the particle. Exposing 0.2-0.3mm diameter sieved particles of α -CuAlCl₄ to greater than 50 Torr of ethylene gives approximately the same total molar sorption of gas as for a agate mortar and pestle ground sample, however no inflection is observed in the TGA data, (Figure 4.2b). Instead a steady weight gain occurs which only slows as the reaction approaches an equilibrium at a total weight corresponding to sorption of 1.8 molar equivalents of ethylene. The desorption curve observed after switching to a pure N₂ gas stream is similar for both the fine powder and sieved samples.

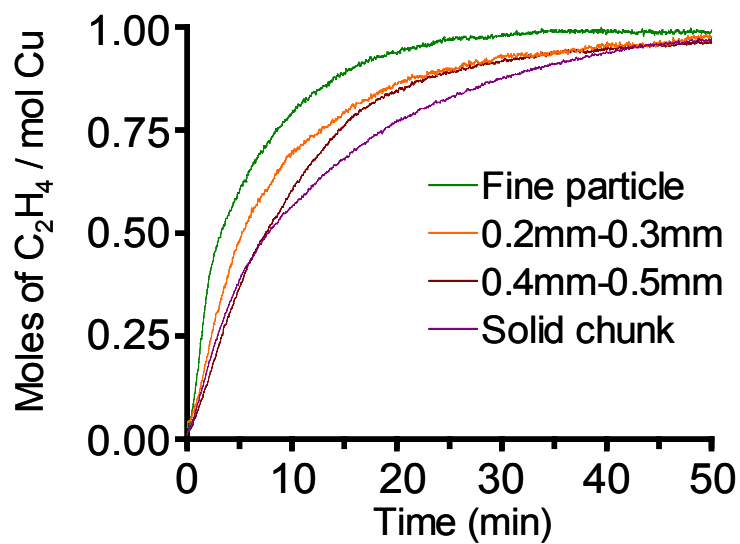


Figure 4.4. The particle size dependence of the reaction of CuAlCl_4 at ethylene partial pressures below 30 Torr. The reaction rate decreases somewhat with increasing particle size.

CuAlCl₄ + CO TGA/DSC data.

The sorption of CO by α -CuAlCl₄ was also monitored by TGA/DSC. Based on the CuAlCl₄/CO sorption isotherms reported previously, under the pressures accessible with this experiment only the 1-equivalent phases can form in completion. The TGA and DSC data collected for these experiments was not very repeatable, however a representative experiment representing the most commonly observed features is given in Figure 4. Typically less than one molar equivalent of CO was bound at a gas pressure of 650 Torr, with an initial linear weight gain similar to that observed in the ethylene reactions followed by a slower rate of sorption. Other experiments exhibited an initial period of rapid weight gain followed by a slower near linear weight gain and did not go as far to completion. Note that it is impossible to differentiate between the formation of **1-CO_{Al}** and (CO)CuCl by the TGA weight gain alone. However, in the majority of the experiments the DSC data indicate a nonreversible process, with a larger exothermic energy of sorption (average -100 ± 10 kJ/mol) than the endothermic energy of desorption (55 ± 12 kJ/mol). The enthalpy of desorption is very close to the enthalpy of -45.58 kJ/mol of Cu reported for the CuCl + CO gas sorption reaction.¹⁶ The desorption enthalpy and irreversibility of the reaction strongly suggests the moisture catalyzed disproportionation sorption pathway for CO sorption is followed in this experiment. Interestingly, the desorption curve in the TGA data is quite different from that observed in the ethylene experiments. Ethylene exhibits a two-step desorption with the majority of the bound gas desorbed over about ten minutes. However, with desorption of CO a rapid but small weight loss, corresponding to approximately 0.05 equivalents of gas, is observed when the purge gas is changed to N₂. Subsequently, the weight loss slows

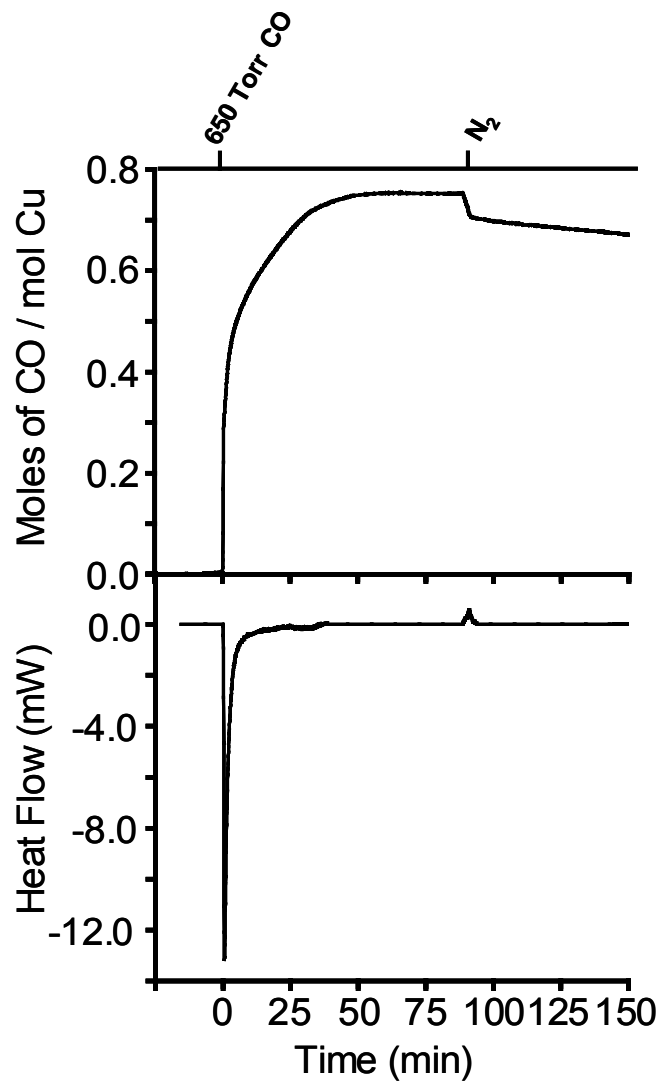


Figure 4.5. TGA/DSC data of the α -CuAlCl₄ reaction with CO. The DSC indicates the irreversibility of the reaction under these experimental conditions.

dramatically for the remainder of the CO desorption. One sample after being left under constant N₂ purge for 6 hours after CO sorption still retained 0.5 equivalents of gas.

Optical Microscopic Study of Reaction Progress

To help elucidate the effect of particle size on ethylene sorption, the progress of these reactions was monitored using a gas manifold attached to a 1 cm cuvette on a microscope stage. The microscope lamp heats the sample inside the cuvette to approximately 35°C. Figure 4.6 shows several subsequent images documenting the low pressure reaction of finely ground α -CuAlCl₄ at 400x magnification. As shown in Figure 4.6a, prior to reaction there is a clear distribution of particle sizes such that some particles are almost too small to observe, while other larger particles show crystallinity under polarized light (maximum diameter 70 μ m). One minute after exposure to 35 Torr of ethylene, Figure 4.6b, a small change in some of the smaller particles is observed. After 5 minutes, significant reaction has occurred with most of the small particles forming a liquid product, while several of the larger particles remain intact (Figure 4.6c). As the reaction continues, the larger particles continue to react from the outside in, becoming coated in a liquid product (Figures 4.6d and e), and eventually completely converting the liquid, Figure 4.6f. Exposure to higher pressures of ethylene greater than 50 Torr results in a recrystallization as the solid product 2-et. A similar process is observed when finely ground α -CuAlCl₄ is exposed to higher pressures of ethylene. The powder reacts to give a liquid melt of **et-1** phase in less than a minute, followed by crystallization as the solid **et-2** forms. On exposure to vacuum, the reaction proceeds in reverse, with the high pressure crystalline product first melting to give the liquid **et-1** phase

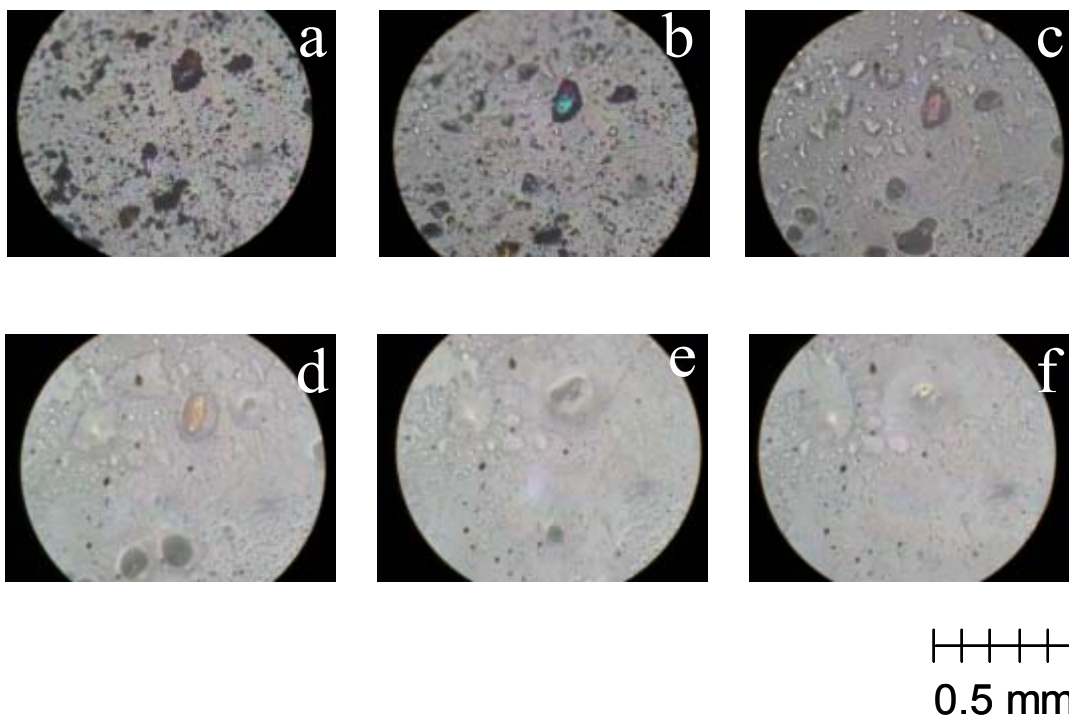


Figure 4.6. Optical microscopy showing finely ground α -CuAlCl₄ a) prior to reaction with ethylene, b) 1 minute after exposure in which the smallest particles have reacted, c) 5 minutes after initial exposure showing significant formation of the liquid **et-1**, d) 10 minutes after exposure with the majority of the sample liquid with a the reaction still penetrating the largest particle, e) 15 minutes after exposure in with further penetration into the largest particle, and f) nearly complete formation of the liquid **et-1** adduct.

and then recrystallizing as the parent CuAlCl_4 is reformed. The sorption/desorption cycle can be repeated with similar results.

No obvious signs of reaction are observed when sieved particles of diameter 0.2mm-0.3mm are exposed to <50 Torr of gas, however at higher pressures of ethylene clear evidence of reaction is observed. Figure 5.7 shows the progression of the reaction of sieved 0.2mm-0.3mm diameter $\alpha\text{-CuAlCl}_4$ particles exposed to an initial pressure of 400 Torr of ethylene. The resolution of the images from the microscope did not capture the reaction as it occurred, however comparison of the particles prior to and following exposure to 400 Torr of ethylene (Figure 5.7 a and b respectively) show that particles after reacting have expanded and perhaps fragmented somewhat. On exposure to vacuum, the product begins to melt as the liquid **et-1** is formed (Figure 5.7c) and eventually yields a crystalline CuAlCl_4 after the ethylene gas is completely desorbed (Figure 5.7d). As can be seen in Figure 5.7d the product formed on desorption consists of significantly fragmented particles as compared to the unreacted CuAlCl_4 particles in Figure 5.7a.

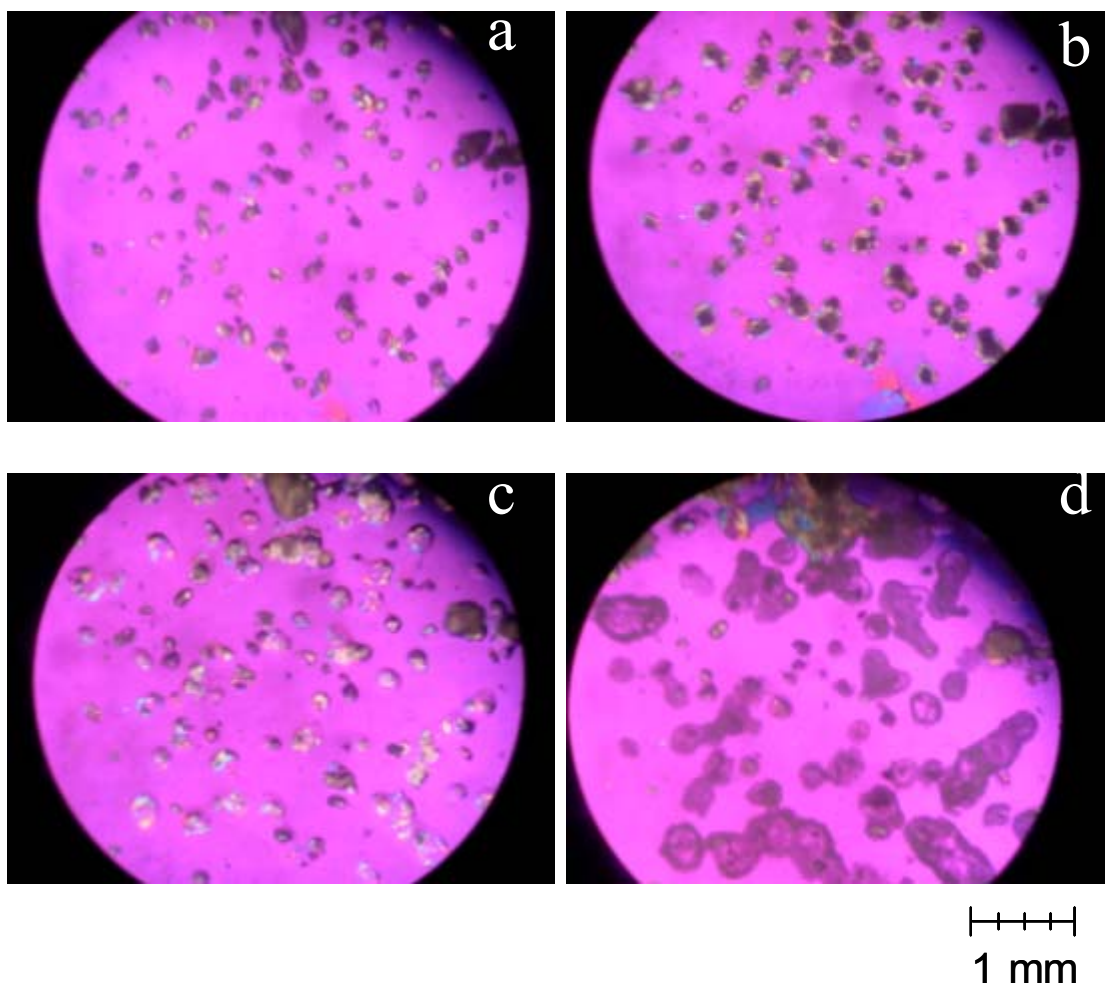


Figure 4.7. Particles of α -CuAlCl₄ sieved to 0.2-0.3mm diameter a) prior to reaction with ethylene, b) after exposure for 1 hour, c) during the initial stages of ethylene desorption from **et-2** yielding some liquid **et-1**, and d) after desorption is complete leaving highly fractured α -CuAlCl₄.

4.4 Discussion

In this study the kinetics of the ethylene/CuAlCl₄ gas sorption reactions have been measured by simultaneous TGA/DSC at 35°C. By controlling the partial pressure of ethylene in the TGA carrier gas, the separate reaction pathways reported previously for ethylene sorption were accessed. At ethylene partial pressures below 30 Torr the gravimetric experiments show that CuAlCl₄ binds one molar equivalent of gas to yield a one-equivalent ethylene adduct. On increasing the pressure of ethylene to above 50 Torr up to one atmosphere, the one-equivalent phase binds an additional 0.8-0.9 equivalents of gas, consistent with the previously reported stepwise sorption isotherm. In this same previous work, X-ray diffraction experiments cooled to 15°C showed that ethylene sorption by CuAlCl₄ occurred by a solid-solid phase transition to give crystalline **et-1** and **et-2**. However, microscopic observation of these reactions at 35°C show that **et-1** is a liquid while **et-2** is crystalline. Therefore at 35°C the higher melting temperatures of α -CuAlCl₄, **et-1** and **et-2** (236°C, ~30°C and 42°C respectively) lead to a solid-liquid-solid stepwise reaction.

The low melting temperature around 30°C of **et-1** slightly complicates the interpretation of this kinetic study. At the lowest operating of the TGA instrument, 35°C, **et-1** is molten thus precluding the study of the solid-solid phase transition occurring at lower temperature. Nevertheless, the liquids are still a condensed state of matter. As was shown in Chapter 3, a significant similarity exists between the structure of the covalent ladder chain in ACu₂Cl₃ solids and that of their low temperature melts. Although the melt structures of the Et/CO-CuAlCl₄ have not yet been studied, it is likely that the covalently bonded chains of their crystalline structures also persist over some length scale in the liquid state. Therefore to understand the formation of **et-1** from an atomistic perspective we work with the assumption

of similar crystalline and liquid state structure. Further, while the solid-state rate laws such as the Avrami-Erofe'ev model described in section 4.2 are typically used to describe the rate of product phase growth for a solid-solid phase transition or reaction, they should also be applicable to any condensed phase reaction. As such, it is still appropriate to discuss the solid-liquid phase transitions in terms of the Sharp-Hancock analysis.

Kinetics of Low Pressure Et-CuAlCl₄ gas sorption.

Samples of α -CuAlCl₄ exposed to pressures below 30 Torr of ethylene bind one-molar equivalent of gas, however, the rate of gas up-take appears to be somewhat particle size dependent. The TGA data indicates that gas sorption by a finely ground powder of CuAlCl₄ occurs via a stepwise process. Sharp-Hancock analysis is instructive to differentiate any change in the reaction mechanism during the course of the reaction. A plot of $\ln(-\ln(1-\alpha))$ versus $\ln t$ from a representative experiment is depicted in Figure 4.8. The Sharp-Hancock slope, n , over the range of $0.1 < \alpha < 0.4$ is 1.38 and the rate constant calculated from the y-intercept of the linear region is $4.9 \times 10^{-3} \text{ s}^{-1}$. In every experiment the slope of the Sharp-Hancock plot is between 1-2 over the range $0.1 < \alpha < 0.4$ with an average rate constant k of $5 \pm 1 \times 10^{-3} \text{ s}^{-1}$ for the 18 experiments. At $\alpha \approx 0.4$ in Figure 4.8 an abrupt change in slope occurs, followed by a second linear portion over the range $0.4 < \alpha < 0.7$. This second linear region has both a smaller slope, $n = 0.73$ and a smaller rate constant of $3.1 \times 10^{-3} \text{ s}^{-1}$. This change in slope at $\alpha \approx 0.4$ is present in the Sharp-Hancock slope of every low pressure experiment (slopes range from 0.5-1 and an average rate constant of $3 \pm 2 \times 10^{-3} \text{ s}^{-1}$) and is indicative of a significant change in mechanism. Interestingly this observation of dual mechanisms appears to be significantly particle size dependant. With larger CuAlCl₄

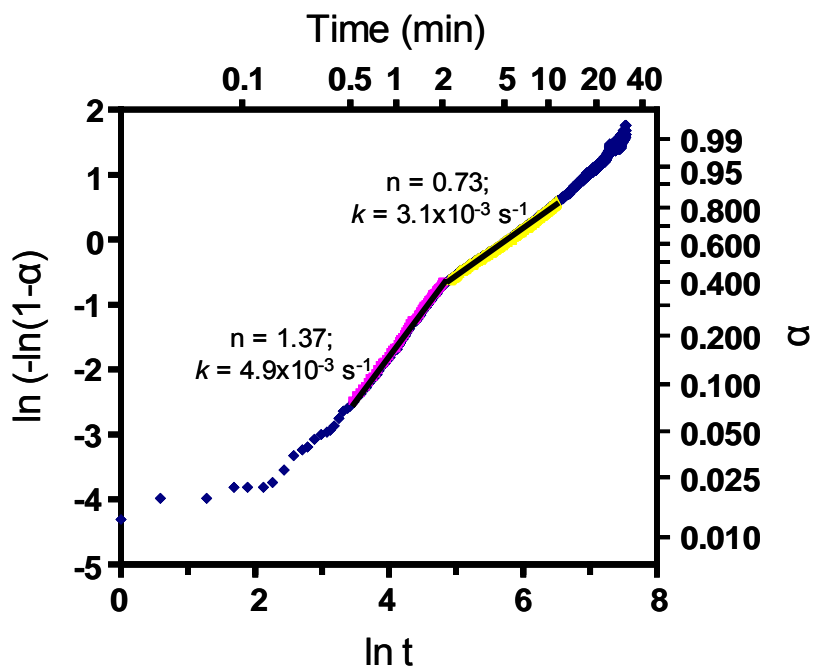


Figure 4.8. Sharp-Hancock plot for the low pressure reaction of finely ground CuAlCl_4 particles, which exhibits a change of slope near $\alpha = 0.40$ indicating a change in the reaction mechanism.

particles, there is little to no change in the Sharp-Hancock slope of $\sim 1-1.5$ over the range $0.1 < \alpha < 0.4$ (Figure 4.9). The observed rate constant for the large particle reaction, $1.7 \times 10^{-3} \text{ s}^{-1}$, is more similar to the rate of the latter portion ($\alpha > 0.4$) than the early part of the fine powder reaction.

The Sharp-Hancock slope over the range $0.1 < \alpha < 0.4$ is consistently between 1-2 for the fine powder CuAlCl_4 ethylene sorption reaction indicating a 1-D phase boundary controlled growth process. The value of n at $\alpha \geq 0.4$ in the fine particle experiments suggests a diffusion controlled mechanism by the guidelines given by Sharp and Hancock. However, Sharp and Hancock assumed a single reaction mechanism is operative over the entire reaction from $0 < \alpha < 1$, while the change in slope at $\alpha \approx 0.4$ indicates a dual mechanism. Further the slope of the Sharp-Hancock plot is very sensitive to the choice of t_0 . Since the second mechanism becomes operative well after t_0 , we cannot assign the kinetics of the low pressure reaction for $0.4 < \alpha < 0.7$ to a group of rate laws by the guidelines given by Sharp and Hancock. Rather than indicating a diffusion controlled mechanism, the decrease in the slope after $\alpha \approx 0.4$ is simply due to the slower rate constant of the second reaction mechanism.

The kink near $\alpha = 0.4$ in the TGA data for the low pressure reaction of fine particles of $\alpha\text{-CuAlCl}_4$ is similar to kinetic data reported for species diffusing into porous carbons.^{17,18} This kind of kinetic behavior has previously been attributed to sorption occurring by competitive rate processes.¹⁷ While the change in the slope of the Sharp-Hancock plot for the fine particle reaction at low ethylene pressure is indicative of dual mechanisms, no major change in slope in the Sharp-Hancock plot when the sample consisted of larger particles. Further the similarity in the rate constants between the reactions of the large particle and the

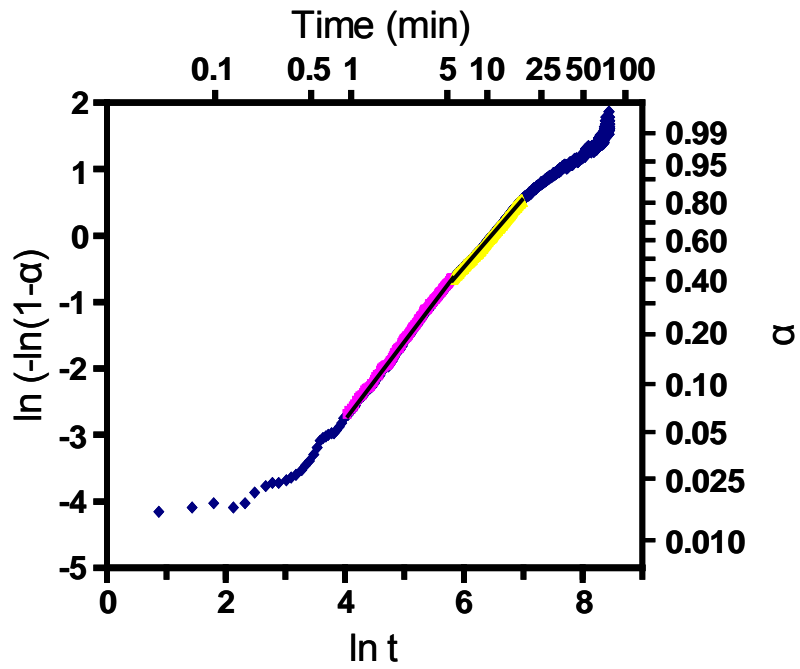


Figure 4.9. The Sharp-Hancock plot for the low pressure reaction of CuAlCl_4 particles sieved to a diameters from 0.2-0.3 mm, which has a single linear region over the approximate range $0.05 < \alpha < 0.75$.

$0.4 < \alpha < 0.7$ portion of the well ground samples suggest that the change in reaction mechanism at $\alpha \approx 0.4$ may be related to particle size. The microscopic observation of the ethylene sorption lends support to this hypothesis. Samples consisting of fine particulate α - CuAlCl_4 react with ethylene at low pressures to give a one-equivalent liquid. During the reaction, the smallest particles react quickly and completely form the liquid. The larger particles react rapidly to give the liquid only at their surface with more gradual reaction continuing deeper into the particle. Therefore, we propose that the step in the TGA data corresponds to two separate processes: rapid sorption near the particle surface, followed by slower gas sorption penetrating deeper into the lattice of sufficiently large particles. If the well ground α - CuAlCl_4 is considered to consist of perfect cubes with an average edge dimension of $10 \mu\text{m}$ (an extremely simplified model),¹⁹ fewer than 1% of the total reactive Cu^+ sites in the sample are present at the surface, which does not fully account for the initial rapid sorption of 0.4 equivalents. Therefore, this surface reaction must also include some penetration deeper into the crystallites. Based on the idealized model for the average particle size above, nucleation at the surface followed by penetration in to the lattice to a depth of $0.154 \mu\text{m}$ on all faces would constitute 40% reaction. By contrast reaction penetration to this depth would only account for 0.25% for a 0.2 mm diameter particle, which is consistent with no dramatic kink in the Sharp-Hancock plot of larger particle experiments. After the surface penetration stops, reaction into the bulk material must proceed by a second rate limiting process. While the two processes are distinct, Sharp-Hancock analysis indicates both the surface and bulk reaction occur via a 1-D growth mechanism. The second rate limiting process may correspond to either fracturing or expansion of the crystalline lattice, which is required to expose fresh reactive surface.

Two-equivalent Adduct formation from Liquid Et-1.

On exposure to pressures greater than 50 Torr of ethylene, the **et-1** liquid rapidly absorbs additional ethylene to bind a up to two equivalents of gas, as shown by the TGA experiments represented by Figure 4.2a. Following this reaction by optical microscopy the **et-1** liquid is observed to crystallize upon additional ethylene sorption to form the **et-2** product. Sharp-Hancock analysis of the TGA weight gain associated with this crystallization shows a significant dependence on the ethylene pressure. Sharp-Hancock plots for several pressures are shown in Figure 4.10 exhibiting slopes from 1 to greater than 4 at higher pressure, indicating an autocatalytic reaction process. At the lowest pressures, where the autocatalysis is least significant, the Sharp-Hancock slope is closer to 1, suggesting the reaction truly follows one-dimensional growth. Therefore by equation 2, $n-1$ gives the component of the slope due to the nucleation term, β . The nucleation component, plotted versus pressure in Figure 4.11, roughly follows a natural logarithmic function:

$$\beta = 1.0259 \cdot \ln[\text{Et}] - 3.96 \quad (5)$$

The data show significant scatter likely because β represents the *probability* of nucleation. Therefore eq. 5 can only be used as an approximate predictor of the effect of ethylene pressure on nucleation. Interestingly, the empirical relationship suggests no nucleation can occur at ethylene pressures below 48 Torr, (where eq. 5 = 0) which is equivalent to the equilibrium desorption pressure of the **et-2** phase observed in the previously reported desorption isotherm. The calculated reaction rate constants, k_{obs} , extracted from the Sharp-Hancock analysis show a clear linear dependence on ethylene pressure (Figure 4.12), with a

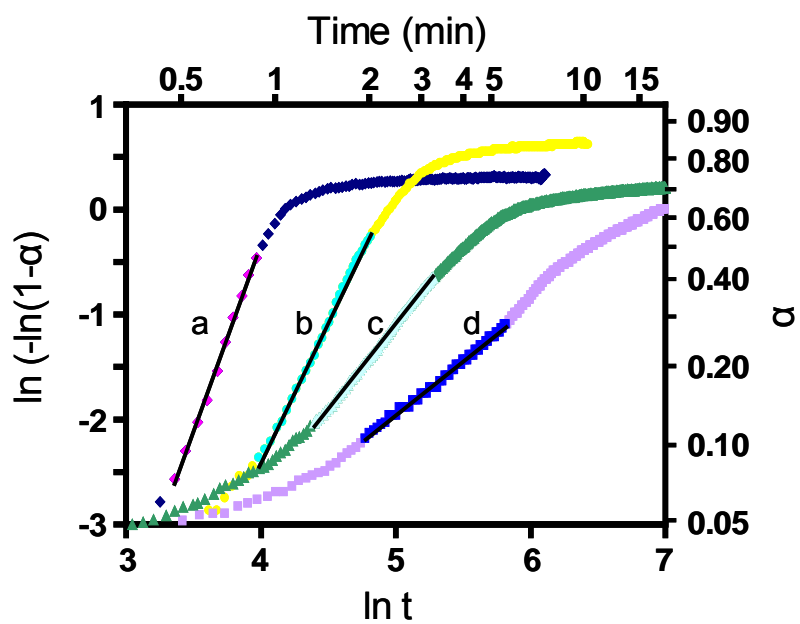


Figure 4.10. Sharp-Hancock plots for the $et-1 \rightarrow et-2$ reaction at a) 700 Torr, b) 620 Torr, c) 320 Torr and d) 70 Torr, with slopes between $0.15 < \alpha < 0.5$ of 3.56, 3.31, 2.70 and 1.05, respectively.

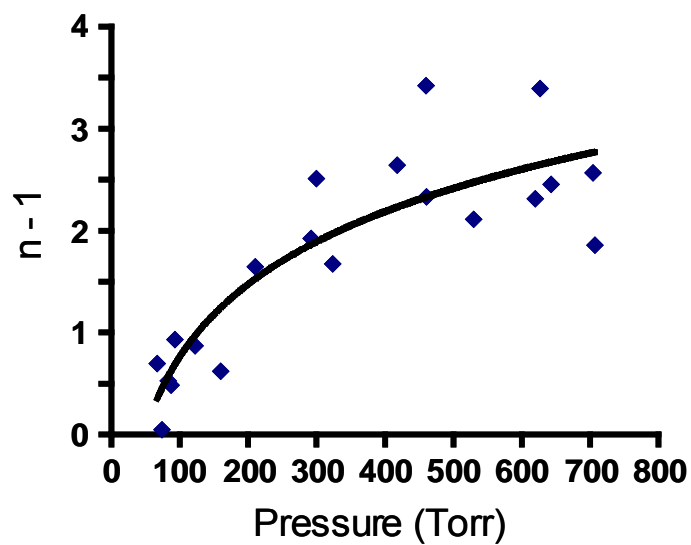


Figure 4.11. The ethylene partial pressure dependence of the probability of nucleation, β , for the 1-D phase boundary controlled crystallization of **et-2** from the **et-1** melt occurring on sorption of a second equivalent of gas.

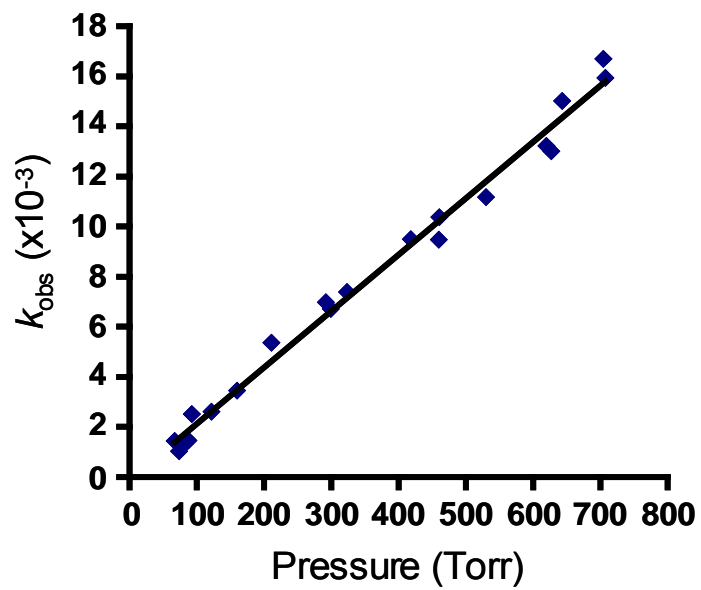


Figure 4.12. The pressure dependence at 35°C of the rate constant k_{obs} extracted from the Sharp-Hancock analysis of the TGA data for the et-1 to et-2 ethylene sorption reaction.

slope equal to the true rate constant of $2.25 \times 10^{-5} \text{ s}^{-1} \text{ Torr}^{-1}$. A similar linear dependence on reactant pressure has also been reported for the kinetics of some heterogeneous reactions yielding metal hydrides²⁰ and is consistent with the proposed S_n2 type mechanism. A general expression, can therefore be given to include the effect of pressure on ethylene gas sorption reaction from the one-equivalent liquid:

$$[\ln(1-\alpha)]^{1/n} = k_{obs} t = 2.25 \times 10^{-1} \text{ s}^{-1} \text{ Torr}^{-1} [\text{Et}]t$$

where $[\text{Et}]$ is measured in Torr and $n = 1 + \beta$, where β is described by eq. 5.

*Direct formation of **et-2** from CuAlCl_4 on at high ethylene pressure.*

Previous work conducted at 15-25°C suggested that at initial exposure to ethylene gas pressures greater than 100 Torr CuAlCl_4 may be converted directly to **e-2**. This reaction reaction pathway is distinct from the stepwise reaction giving the **et-1** intermediate. However, as shown in Figures 4.2a and 4.3, at 35°C reaction of finely ground $\alpha\text{-CuAlCl}_4$ with 100 Torr or greater ethylene partial pressures exhibits an inflection in the TGA data at $\alpha = 0.4$ and two overlapping exothermic peaks in the DSC, which both suggest a two-step reaction process. This is consistent with optical microscopy for this reaction, in which on exposure to greater than 100 Torr finely ground $\alpha\text{-CuAlCl}_4$ is always observed to yield the liquid **et-1** followed by a rapid crystallization to give **et-2**. Therefore, under the conditions of these experiments, the direct formation of **et-2** from $\alpha\text{-CuAlCl}_4$ does not occur. Instead formation of the **et-1** liquid phase is favored kinetically. The rapid TGA weight gain and second DSC peak correspond to the further adduct formation and rapid crystallization

observed microscopically. The step in the TGA data occurs at approximately the same molar amount of ethylene sorbed, 0.4 equivalents, as the inflection in the Sharp-Hancock plot observed for the lower pressure reaction. This supports the suggestion of an initial and rapid surface reaction yielding liquid **et-1**. By contrast the reaction of larger sieved CuAlCl_4 particles at high pressure does not show a step in the TGA curve and exhibits a single DSC peak (Figure 4.2b). In this case, due to the low surface area of the sieved particles, only a small amount of liquid **et-1** is formed from the surface reaction (less than 0.25% for a surface reaction penetration depth of $0.154 \mu\text{m}$), and the remainder of the reaction is rate limited by lattice expansion and fracture such that the TGA and DSC data seem to indicate a single reaction process. While a systematic study of ethylene pressure and particle size dependence of the kinetics for the large particle-high pressure sorption reaction has not been conducted, the reaction has been studied at pressures near 100 Torr and 650 Torr. Experiments near 100 Torr exhibited Sharp-Hancock slopes from 1.7-2.3, while ethylene pressures around 650 Torr gave slopes between 2.8-3.5. This increase in the Sharp-Hancock slope with pressure suggests that the lattice expansion/fracture mechanism is pressure dependent, while the low pressure experiments suggest a maximum growth dimensionality of 1 or 2.

Sorptive Reconstruction Mechanism

Previously a sorptive reconstruction mechanism was proposed for the stepwise gas sorption reactions of CuAlCl_4 . In this mechanism the one equivalent adducts can be formed by S_n2 attack on Cu by either ethylene or CO directed along sets of van der Waals channels in the $\alpha\text{-CuAlCl}_4$ lattice. Attack at the van der Waals channels, which can be seen looking on the close-packed chloride layers, Figure 4.13a, excises a CuAlCl_4 chain running along the

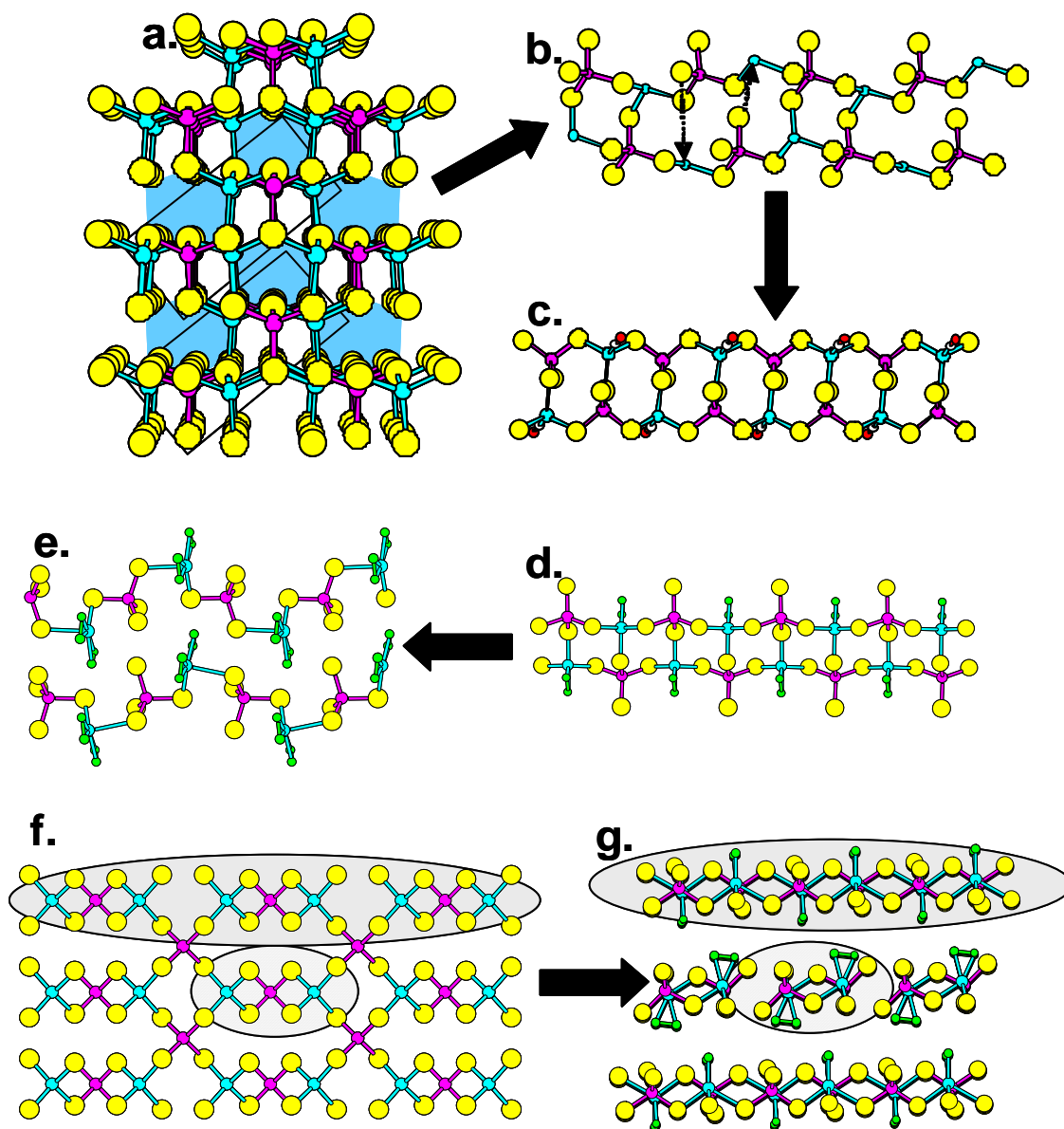


Figure 4.13. a) View of α - CuAlCl_4 down the 112 lattice vector with the entrance to the van der Waals channels shaded. b) Chains running along the 112 vector which are excised from the CuAlCl_4 lattice by the sorptive reconstruction mechanism to give the ladder chain structures c) β - COCuAlCl_4 or d) β - etCuAlCl_4 . f) Alternatively reaction may be directed along the perpendicular sets of tetragonal channels running along the 100 and 010 lattice vector to give the perpendicular sets of α - etCuAlCl_4 chains.

112 lattice vector. Rotation of the AlCl_4^- tetrahedra from the excised chain, as indicated by the arrows in Figure 4.13b, yield the ladder chain structure of the $\beta\text{-etCuAlCl}_4$ and $\beta\text{-COCuAlCl}_4$ adducts. Attack by an additional equivalent of gas at copper breaks the Cu-Cl bond which serves as the rung of the ladder chain in the β -adducts and ‘unzips’ the double-chain to give two single chains in the two equivalent adduct, as pictured for **et-2** in Figure 4.13c and d. A second low pressure reaction was also proposed where gas sorption directed along the tetragonal van der Waals channels of $\alpha\text{-CuAlCl}_4$ yields the $\alpha\text{-etCuAlCl}_4$ or $\alpha\text{-COCuAlCl}_4$ structures, which consist of sets of perpendicular ladder chains (Figures 4.13e and f).

Sharp-Hancock analysis of the kinetic data for the ethylene gas sorption reactions at 35°C indicate a phase boundary controlled process with a maximum growth dimensionality of 1 for low pressure formation of liquid **et-1** and the subsequent crystallization of **et-2**. The sorptive reconstruction mechanism for gas sorption into $\alpha\text{-CuAlCl}_4$ may not strictly apply at 35°C since a one-equivalent liquid ethylene adduct is involved in the reaction. Even though the product of the reaction is a liquid, van der Waals channels of the reactant likely direct the reaction through $\alpha\text{-CuAlCl}_4$. Therefore, the observed 1-D growth for the low pressure ethylene reaction is still consistent with the sorptive reconstruction reaction pathway in Figures 4.13a-c. The liquid-to-solid reaction to give crystalline **et-2** also follows 1-D growth kinetics. In this case 1-D growth kinetics is consistent with the crystallization of chain-based product phase. The linear dependence of the rate of crystallization and **et-2** formation on the pressure of ethylene provides supporting evidence for an associative mechanism, which is consistent with the proposed $\text{S}_\text{n}2$ attack on Cu(I)-centered tetrahedra.

While the data here gives supporting evidence for the sorptive reconstruction mechanism, more study of these reactions may help to further substantiate this model. For example, an experimental technique for studying the kinetics of these reactions below 35°C will provide a more direct assessment of the solid-solid reaction mechanism. Nevertheless, the current work suggests similarities between the solid-solid and solid-liquid reactivity of α -CuAlCl₄. A study of the liquid structure of the CuAlCl₄ adducts may help to further explain the observed similarities.

Thermodynamic Considerations.

The DSC data for the step-wise ethylene sorption reactions at 35°C showed enthalpies of -77 ± 6 kJ/mol Cu for the formation of liquid **et-1** and -173 ± 7 kJ/mol Cu for the crystallization of **et-2** at higher ethylene pressure, corresponding to a total reaction energy of -250 kJ/mol Cu for **et-2**. The ΔH for matrix isolated Cu⁺ binding ethylene to give the complex (Et)₂Cu⁺ was previously shown to be -175 kJ/mol Cu for each equivalent of ethylene.²¹ As discussed in Chapter 2, matrix isolated Cu⁺ should exhibit the non-classical limit of bonding to a π -coordinating ligand, and will result in the strongest possible Cu(I)-Et bond. Therefore, the -175 kJ/mol Et reported for matrix isolated (Et)₂Cu⁺ represents the maximum exothermic enthalpy for sorption of ethylene by a Cu(I) compound. In addition to the exothermic Cu-Et bond formation, reaction of α -CuAlCl₄ to yield the (Et)_xCuAlCl₄ adducts includes endothermic contributions including breaking a Cu-Cl bond and a net positive change in the enthalpy of lattice energy, resulting from the CuAlCl₄ network expansion on gas sorption. These endothermic factors are expected to result in a process less exothermic than -175 kJ/mol Cu for ethylene sorption by CuAlCl₄. By way of

comparison, the enthalpy for sorption of one equivalent of ethylene by solid CuCl has been measured to be -34.7 kJ/mol Cu.²² As expected this is less exothermic than the formation of $(\text{Et})_x\text{CuAlCl}_4$ adducts, since from by the solid state Et/CuCl gas sorption reaction gives a weaker Cu-Et bond and requires a greater lattice expansion. Given the possible range of enthalpies, between -34.7 kJ/mol Cu to -175 kJ/mol Cu, the value of -173 ± 7 kJ/mol measured for the sorption of the second equivalent of ethylene seems too close to the maximum for matrix isolated Cu^+ . However, taking into account the exothermic contribution of crystallization from the one equivalent liquid phase makes the value of -173 kJ/mol seem more reasonable. Similarly formation the melting of **et-1** at 35°C from solid $\alpha\text{-CuAlCl}_4$ solid should make an endothermic contribution to the phase change. Therefore the actual energy associated with the solid-solid CuAlCl₄ gas sorption of one equivalent of ethylene is likely intermediate between -77 and -173 kJ/mol Cu.

4.5 Conclusions

The kinetics of the gas sorption reactions of CuAlCl₄ with ethylene and CO have been studied by TGA, DSC and optical microscopy. The experiments show that at 35°C CuAlCl₄ forms one and two-equivalent ethylene adduct phases and a one-equivalent CO adduct at or below 1 atmosphere of reactive gas, consistent with the sorption isotherms reported at lower temperature. At the slightly elevated temperature of these experiments, the one-equivalent ethylene adduct is a liquid rather than a crystalline solid as observed for the lower temperature reactions. The sorption of in these experiments CO follow the disproportionation pathway to yield (CO)CuCl. The gas sorption reactions forming the

liquid one-equivalent ethylene phase and the two equivalent crystalline phase **et-2** proceed by 1-D growth processes in the acceleratory portion of the reaction. The rate of crystallization of **et-2** after the **et-1** liquid binds a second equivalent of ethylene is linearly dependent on pressure, consistent with an associative reaction mechanism. Sharp-Hancock analysis of this reaction at different pressures indicate a 1-D growth process with autocatalytic nucleation occurring at higher ethylene pressures. A natural logarithmic function helps to predict the pressure dependence of the autocatalytic nucleation. While the reactions at 35°C are not strictly in the solid state, the growth dimensionality and rate dependence on ethylene pressure provide support for the proposed sorptive reconstruction mechanism, whereby S_n2 attack by ethylene propagates along van der Waals channels in the α -CuAlCl₄ crystalline lattice. That the kinetics of the reaction which yield the liquid one-equivalent phase are consistent with the mechanism proposed for the solid-state reaction suggests that the covalently bonded metal halide chains in the crystalline Et/CO adducts of CuAlCl₄ persist into the molten state.

4.6 Experimental

General Methods and Materials.

All manipulations were performed under a nitrogen atmosphere in a Dry-Box. The α -CuAlCl₄ used in DSC/TGA and barometric sorption isotherms was prepared by literature methods. Nitrogen, ethylene and carbon monoxide gas were used as purchased from National Welders.

Thermal Analysis Experiments.

All thermal data was collected using a TA instruments SDT 2960 (simultaneous DSC/TGA) equipped with a gas switching accessory. Prior to the experiment α -CuAlCl₄ samples were either ground in to a fine powder with a mortar and pestle or sieved to a certain range of particle size (0.2-0.3 mm, 0.3-0.4mm or 0.4-0.5 mm diameter). In a typical experiment, 10 mg of α -CuAlCl₄ in an alumina sample cup was exposed to N₂ purge gas for three minutes to establish a baseline for the DSC and TGA. After three minutes, the gas switching accessory was used to change from N₂ to the reactive purge gas to start the gas sorption reaction. The sample was exposed to the reactive gas until no further weight gain was observed by TGA, after which the purge gas was changed back to pure N₂ to initiate the desorption reaction. The partial pressure of ethylene or carbon monoxide in the reactive gas was controlled by mixing the gas with N₂. The gases were combined at a Swagelok tee joint and subsequently traveled through 2 meters of ¼ polyethylene tubing at a rate of 40 L/min before entering the SDT 2960 to allow the gas to have a uniform composition at the sample. The total pressure of the purge gas was assumed to be 1 atmosphere. Specific partial pressures were achieved by controlling the flow rate of each gas prior to mixing at the T joint. For example, flow rates of 30 mL/min for both ethylene and 30 mL/min for N₂ provided a partial pressure of 0.5 atm (380 Torr).

In every experiment an instrumental effect occurs when the purge gas is changed using the gas switching accessory, causing a slight change (positive or negative) in the measured mass of the sample provides a convenient marker for time zero. A delay of approximately 0.05 min is observed from the time of this time zero marker and the first

observed weight gain due to gas sorption. The delay corresponds to the time required for the new purge gas to travel through the 2 meters of polyethylene tubing to reach the sample.

Optical Gas Sorption Experiments.

Powdered or sieved samples of α -CuAlCl₄ were loaded into a fused silica ampule under an N₂ atmosphere. The ampule was then affixed to a gas/vacuum manifold and subsequently evacuated to remove the N₂ gas. A predetermined pressure of ethylene gas was introduced to sample through the gas manifold. The ethylene pressure was measured using an MKS PDR-D-1 pressure transducer. Progress of the reaction was monitored visually under 400x magnification using a Nikon Labophot2-Pol polarizing microscope. Heat from the microscope warms the fused silica ampule and sample to approximately 33-35°C. Lower temperatures (25-27°C) were achieved for certain experiments by blowing N₂ gas cooled to 0°C over the sample.

4.7 References

- (1) (a) Fletcher, A. J.; Thomas, K. M.; Rosseinsky, M. J. *J. Solid St. Chem.* **2005**, *178*, 2491-2510. (b) Matsuda, R.; Kitaura, R.; Kitagawa, S.; Kubota, Y.; Belosludov, R. V.; Kobayashi, T. C.; Sakamoto, H.; Chiba, T.; Takata, M.; Kawazoe, Y.; Mita, Y. *Nature*, **2005**, *436*, 238-241. (c) Maji, T. K.; Mostafa, G.; Matsuda, R.; Kitagawa, S. *J. Am. Chem. Soc.* **2005**, *127*, 17152-17153. (d) Zhao, X.; Xiao, B.; Fletcher, A. J.; Thomas, K. M.; Bradshaw, D.; Rosseinsky, M. J. *Science* **2004**, *306*, 1012-1015.
- (2) (a) Rosi, N. L.; Eckert, J.; Eddaoudi, M.; Vodak, D. T.; Kim, J.; O'Keefe, M.; Yaghi, O. M. *Science*, **2003**, *300*, 1127-1129. (b)
- (3) *Reactions in the Solid State, Comprehensive Chemical Kinetics*; Bamford, C. H.; Tipper, C. F. H. Eds.; Elsevier: Amsterdam, 1980; Vol. 22.
- (4) (a) Cussen, E. J.; Claridge, J. B.; Rosseinsky, M. J.; Kepert, C. J. *J. Am. Chem. Soc.* **2002**, *124*, 9574-9581. (b) van Poppel, L. H.; Bott, S. G.; Barron, A. R. *J. Am. Chem. Soc.* **2003**, *125*, 11006-11017. (c) Albrecht, M.; Lutz, M.; Spek, A. L.; van Koten, G. *Nature*, **2000**, *406*, 970-974.
- (5) (a) Tropsch, H.; Mattox, W. J. *J. Am. Chem. Soc.* **1935**, *57*, 1102-1103. (b) Gilliland, E. R.; Seebold, J. E.; Fitzhugh, J. R.; Morgan, P. S. *J. Am. Chem. Soc.* **1939**, *61*, 1960-1962.
- (6) Peng, X. D.; Golden, T. C.; Pearlstein, R. M.; Pierantozzi, R. *Langmuir*, **1995**, *11*, 534-537.
- (7) Sullivan, R. M.; Liu, H.; Smith, S. D.; Hanson, J. C.; Osterhout, D.; Ciruolo, M.; Grey, C. P.; Martin, J. D. *J. Am. Chem. Soc.* **2003**, *125*, 11065-11079.
- (8) Capracotta, M. D.; Sullivan, R. M.; Martin, J. D. submitted to *J. Am. Chem. Soc.*
- (9) Dattelbaum, A. M.; Martin, J. D. *Polyhedron* **2006**, *25*, 349-359.

- (10) Martin, J. D.; Leafblad, B. R.; Sullivan, R. M.; Boyle, P. D. *Inorg. Chem.*, **1998**, *37*, 1341-1346.
- (11) Peng, X. D.; Golden, T. C.; Pearlstein, R. M.; Pierantozzi, R. *Langmuir*, **1995**, *11*, 534-537.
- (12) Brown, W. E.; Dollimore, D.; Galwey, A. K. *Reactions in the Solid State*; Bramford, C. H., Tipper, C. F. H., Eds.; Comprehensive Chemical Kinetics Series 22; Elsevier: New York, 1980; pp 42-115.
- (13) (a) Avrami, M. *J. Chem. Phys.* **1939**, *7*, 1103-1112. (b) Avrami, M. *J. Chem. Phys.* **1940**, *8*, 212-224. (c) Avrami, M. *J. Chem. Phys.* **1941**, *9*, 177-184.
- (14) Erofe'ev, B. V. *C. R. Dokl. Akad. Nauk SSSR* **1946**, *52*, 511-514.
- (15) Sharp, J. H.; Hancock, J. D. *J. Am. Ceram. Soc.* **1972**, *55*(2), 74-77.
- (16) Backén, W.; Vestin, R. *Acta Chem. Scan. A* **1979**, *33*, 85-91.
- (17) Ruthven, D. M.; Raghavan, N. S.; Hassan, M. M. *Chem. Eng. Sci.* **1986**, *41*, 1325-1332.
- (18) Fletcher, A. J.; Cussen, E. J.; Prior, T. J.; Rosseinsky, M. J.; Kepert, C. J.; Thomas, K. *M. J. Am. Chem. Soc.* **2001**, *123*, 10001-10011.
- (19) West, Anthony R. *Solid State Chemistry and Its Applications*. John Wiley & Sons. New York, 1984, p 8.
- (20) (a) Rudman, P. S. *J. Less-Common Met.*, **1983**, *89*, 93-110. (b) Hirata, T.; Matsumoto, T.; Amano, M.; Sasaki, Y. *J. Less-Common Met.* **1983**, *89*, 85-91. (c) Uchida, H. H.; Fromm, E. *Z. Phys. Chem. N. F.* **1989**, *164*, 1123-1128.
- (21) Sievers, M. R.; Jarvis, L. M.; Armentrout, P. B. *J. Am. Chem. Soc.* **1998**, *120*, 1891-1899.
- (22) Huang, H. Y.; Padin, J.; Yang, R. T. *Ind. Eng. Chem. Res.* **1999**, *38*, 2720, 2725.